IMPLANTABLE SUB-cm WIRELESS RESONATORS FOR MRI: FROM CIRCUIT THEORY TO MEDICAL IMAGING

A DISSERTATION SUBMITTED TO

THE GRADUATE SCHOOL OF ENGINEERING AND SCIENCE

OF BILKENT UNIVERSITY

IN PARTIAL FULFILLMENT OF THE REQUIREMENTS FOR

THE DEGREE OF

DOCTOR OF PHILOSOPHY

IN

ELECTRICAL AND ELECTRONICS ENGINEERING

By

Sayım Gökyar

December 2017

IMPLANTABLE SUB-cm WIRELESS RESONATORS FOR MRI: FROM CIRCUIT THEORY TO MEDICAL IMAGING

By Sayım Gökyar

December 2017

We certify that we have read this dissertation and that in our opinion it is fully adequate, in scope and in quality, as a dissertation for the degree of Doctor of Philosophy.

Hilmi Volkan Demir (Advisor)

Ergin Atalar

Oğuz Gülseren

Hatice Kader Karlı Oğuz

Cengizhan Öztürk

Approved for the Graduate School of Engineering and Science:

Ezhan Karasan
Director of the Graduate School

ABSTRACT

IMPLANTABLE SUB-cm WIRELESS RESONATORS FOR MRI: FROM CIRCUIT THEORY TO MEDICAL IMAGING

Sayım Gökyar
Ph.D. in Electrical and Electronics Engineering
Advisor: Hilmi Volkan Demir
December 2017

Making implantable wireless resonators having small footprints is fundamentally challenging when using conventional designs that are subject to the inherent tradeoff between their size and the achievable range of quality-factors (Q-factors). For clinical magnetic resonance imaging (MRI) frequencies (e.g., about 127 MHz for 3 T), conventional resonators either require a diameter of about 20 cm in chip size or off-the-chip lumped elements for successful operation, both of which practically prevent their use as implantable devices. At least two orders-of-magnitude reduction in footprint area is necessary to make on-chip resonators suitable for in-vivo applications. However, decreasing the size of such a conventional resonator chip comes at the expense of substantially decreased Q-factor. Thus, achieving high Q-factors with reduced footprints simultaneously entails a novel approach in implantable electronics. In this thesis work, to address this problem, we proposed, designed and demonstrated a new class of sub-wavelength, thin-film loaded helical metamaterial structures for in-vivo applications including field localization and signal-to-noise ratio (SNR) improvement in MRI. This implantable wireless architecture, implemented fully on chip with partially overlaid helicals on both sides of the chip interconnected by a through-chip-via, enables a wide range of resonant radio frequencies tunable on chip by design while achieving an extraordinarily small footprint area ($<< 1$ cm^2) and ultra-thin geometry (< 30 μm). The miniaturization of such microwave circuits to sub-cm range, together with their high Q-factors exceeding 30 in lossy soft tissues, allows for their use in vivo. The fabricated devices correspond to $1/1500^{th}$ of their operating wavelength in size, rendering them deep sub-wavelength.

For the proposed wireless resonant devices, equivalent circuit models were developed to understand their miniaturization property and the resulting high Q-factors are well explained by using these models. Additionally, full-wave numerical solutions of the proposed geometries were systematically carried out to verify the findings of the developed equivalent circuit models. All of these theoretical and numerical studies were found in excellent agreement with the experimental RF characterization of the microfabricated devices. Retrieval analyses of the proposed architectures showed that these geometries lead to both negative relative permittivity and permeability simultaneously at their operating frequencies, which do not naturally exist together in nature, making these structures true metamaterials. These fabricated wireless devices were further shown to be promising for the in-vivo application of subdural electrode marking, along with SNR improvement and field localization without causing excessive heating in MRI. MR images support that the proposed circuitry is also suitable for MRI marking of implants, high-resolution MR imaging and electric field confinement for lossy medium. Although our demonstrations were for the purpose of marking subdural electrodes, RF characterization results suggest that the proposed device is not limited to MRI applications. Utilizing the same class of structures enabling strong field localization, numerous wireless applications seem feasible, especially where miniaturization of the wireless devices is required and/or improving the performance of conventional structures is necessary. The findings of this thesis indicate that the proposed implantable sub-cm wireless resonators will open up new possibilities for the next-generation implants and wireless sensing systems.

Keywords: Metamaterials, wireless resonators, magnetic resonance imaging (MRI), MR-compatible implants.

ÖZET

MRG İÇİN İMPLANT EDİLEBİLİR KABLOSUZ cm-ALTI ÇINLAÇLAR: DEVRE TEORİSİNDEN TIBBİ GÖRÜNTÜLEMEYE

Sayım Gökyar
Elektrik Elektronik Mühendisliği, Doktora
Tez Danışmanı: Hilmi Volkan Demir
Aralık 2017

Küçük baskı alanına sahip implant edilebilir kablosuz rezonatörlerin (çınlaçların) yapılması, geleneksel tasarımların büyüklükleri ve ulaşılabilen kalite faktörleri aralığı (Q-faktörleri) arasındaki ilişkiye bağlı olarak oldukça zorlayıcıdır. Klinik manyetik rezonans görüntüleme (MRG) frekansları için (örneğin 3 T için yaklaşık 127 MHz), klasik çınlaçlar başarılı bir işlem için ya çip boyutunda yaklaşık 20 cm'lik bir çapa ya da çipten bağımsız harici elemanlara ihtiyaç duyar ki; bunların her ikisi de pratik olarak implant edilebilir cihazlar olarak kullanımı engeller. Vücut içi uygulamalarda kullanılabilmeleri için, yonga boyutunda en az iki basamak (100 kat) küçültme yapılması gereklidir. Bununla birlikte, böyle bir geleneksel rezonatör çipinin boyutunun bu denli azaltılması, önemli ölçüde azaltılmış Q-faktörüyle sonuçlanır. Bu nedenle, baskı alanı azaltılmasının ve yüksek Q-faktörlerinin aynı anda elde edilmesi, implant edilebilir elektronik için yeni bir yaklaşımı gerektirir. Bu tez çalışmasında, bu sorunu çözmek için, yeni bir sınıf olarak dalgaboyunun çok altında, ince film yüklü, sarmal meta-malzeme yapılar önerip, tasarladık ve bunların MRG′de alan lokalizasyonu ve sinyal-gürültü oranı (SNR) iyileştirmeyi de içeren vücut içi uygulamalarını gösterdik. Çipin her iki tarafında kısmen üst üste konmuş helezonlar ile tamamen çipte uygulanan bu implant edilebilir kablosuz mimari, olağanüstü küçük bir baskı alanı elde ederken (<<1 cm^2), çok ince geometriye (< 30 μm) ve tasarımı sayesinde ayarlanabilen geniş bir yelpazede rezonant radyo frekans aralığına olanak tanır. Bu mikrodalga devrelerinin cm-altı aralığına küçültülmesi, kayıplı yumuşak dokularda 30'u aşan yüksek Q-faktörleri ile birlikte vücut-içi kullanımına imkan sağlar. Üretilen cihazların boyutu çalışma dalgaboylarının 1 / 1500'ü büyüklüğüne karşılık gelir ve böylece dalgaboyu çok altına erişilmiş olur.

Önerilen kablosuz rezonant cihazların minyatürleştirme özelliklerini anlamak için eşlenik devre modelleri geliştirildi ve ortaya çıkan yüksek Q-faktörleri bu modelleri kullanarak tutarlı bir şekilde açıklandı. Buna ek olarak, önerilen geometrilerin sayısal çözümleri, geliştirilen eşdeğer devre modellerin bulgularını doğrulamak için sistematik bir şekilde gerçekleştirildi. Bütün bu teorik ve sayısal çalışmalar, mikro-üretilmiş cihazların deneysel RF analizi ile mükemmel bir uyum içinde bulundu. Önerilen mimarilerin çalışma frekanslarında yapılan analizleri, bu geometrilerin doğada doğal olarak bulunmayan ve bu yapıları gerçek metamalzeme haline getiren, hem negatif nispi elektriksel sabite hem de negatif nispi manyetik geçirgenliğe sahip olduğunu gösterdi. Bu imal edilen kablosuz cihazların, MRG'de aşırı derecede ısınmaya neden olmadan SNR iyileştirmesi ve alan lokalizasyonu ile birlikte dura-altı elektrot işaretlemesinin vücut içi uygulaması için umut verici olduğu gösterildi. MR görüntüleri, önerilen devrenin implantların MR görüntülemesi, yüksek çözünürlüklü MR görüntüleme ve kayıplı ortam için elektrik alan yoğunlaştırma için de uygun olduğunu desteklemektedir. Gösterimlerimiz bu çalışmada subdural elektrotları işaretlemek için yapılmış olsa da, RF analiz sonuçları önerilen cihazın sadece MRG uygulamaları ile sınırlı olmadığını göstermektedir. Güçlü alan lokalizasyonunu mümkün kılan aynı yapı sınıfını kullanarak, özellikle kablosuz cihazların minyatürleştirilmesi ve/veya geleneksel yapıların performansını arttırılması gereken yerler gibi sayısız kablosuz uygulama mümkün görünmektedir. Bu tezin bulguları, önerilen implant edilebilir cm-altı kablosuz çınlaçların, gelecek nesil implantlar ve kablosuz algılama sistemleri için yeni imknlar açılacağını göstermektedir.

Anahtar sözcükler: Metamalzemeler, kablosuz rezonatörler, manyetik rezonans görüntüleme (MRG), MR-uyumlu implantlar.

Acknowledgement

I would like to express my appreciation to my supervisor Prof. Hilmi Volkan Demir for his endless energy and motivating personality that propelled me to conduct this research. He technically and mentally guided me through this long, tough and blessed way to keep up the good work.

It is my pleasure to express sincere regards to Prof. Ergin Atalar for his invaluable contribution to this thesis work. He opened the doors of MRI to this research work and allowed us to use UMRAM (National MR Research Center) for our experiments. I would like to thank my committee members, Prof. Oğuz Gülseren, Prof. Hatice Kader Karlı Oğuz and Prof. Cengizhan Öztürk for their valuable comments and guidance.

I would like to express my special thanks to each and every member (past and present) of Devices and Sensors Research Group for their kind and eternal friendship. I also want to thank to Biomedical Engineering Group members and personnel of UMRAM, Department of Electrical and Electronics Engineering, people of UNAM and ARL, members of Outdoor Sports Society (Bilkent-DOST), Bilkent Orienteering Team (BOT) and METU Orienteering Team.

Particularly, I would like to express my thanks to Dr. Akbar Alipour, Emre Unal, Dr. Burçak Bilginer, Dr. Oktay Algın, Dr. Somayyah Fardindoost for their contributions throughout this thesis work. I also want to express my appreciation to Muhammet Göncü, Ozan Kanbertay, Murat Can Yıldız, Ceren Özveri, Elif Tosun and Mürüvet Parlakay for their support during my graduate lifetime.

This is the right time for me to declare my great appreciation to my wife and family. There is no word to define your sacrifice. You have sustained me, you have prayed for me and you have loved me. This work cannot be finished without your blessing support.

This work is partially supported by TUBITAK BIDEB.

Contents

List of Figures

List of Tables

Chapter 1

Introduction

Magnetic resonance imaging (MRI) studies of human being started early 1970s, with the seminal work of Paul Lauterbur [1]. Before MRI, nuclear magnetic resonance (NMR) had been already in use to characterize different materials. In 1946, two researchers, Felix Bloch from Stanford University [2] and Edward Mills Purcell from Harvard University [3], independently reported the first NMR identification of materials for liquids and solids, which was awarded a Nobel Prize in Physics [4]. This starting point turned into a medical imaging platform with the work of Lauterbur, which was also awarded a Nobel Prize in 2003 [5]. The relatively safe nature of MRI made it indispensable part of today′s medical imaging applications. Additionally, this opened a huge research field and today MRI practice has been still being developed.

1.1 Motivation of the Thesis

Obtaining high-resolution MRI with a high signal-to-noise-ratio (SNR) and short acquisition time is a challenging task for clinical applications. In addition to proper pulses, this requires novel coil designs with improved levels of radiofrequency (RF) performance such as a high quality-factor (Q-factor). The motivation of this thesis is to propose and develop a novel wireless resonator architecture to improve clinical MR imaging practice in terms of SNR improvement and marking of implantable devices for possible in-vivo applications.

Although the soft tissue contrast of MRI [1] is its ultimate property from its beginning, which makes MRI the strongest candidate among characteristic imaging modalities (including X-ray, CT, and PET), positioning of devices under MRI requires special treatments including the use of wired connections [6–11], introducing MRI marker materials [12–17] and using wireless passive devices with inductive coupling [18, 19].

Using wired connections to electrically reach devices under MRI is possible for interventional applications [9], but this comes at the cost of increased RF heating risk [20]. Using MRI visible marker materials, such as bearings and dyes [15–17], introduces other disadvantages such as size and non-adjustable relaxation parameters. These markers have sizes of several mm′s in three dimensions [21] that limit their in-vivo usage for most of the clinical applications, e.g., in subdural electrode marking. Additionally, once they are manufactured, longitudinal (T1) and transverse (T2) relaxation times of these markers are constant and their visibility will strictly depend on the MR imaging parameters such as repetition time (TR) and echo time (TE). This may limit the imaging methods; hence, additional scans with proper TR and TE values should be performed for marking of these devices. Simultaneous imaging of marking materials and anatomical features is critical to achieve better registration accuracy [22].

In addition to these methods, multimodal imaging is also used to mark the locations of these implantable devices [23–26]. However, combined registration of images that are acquired from different platforms results in reliability problems due to higher positioning errors from 1 to about 3 mm [27, 28]. In addition to reliability problems, moving patients from one platform to another would also decreases the patient comfort and increases the risk of inflammation. The ability of imaging implantable devices only under MRI would avoid the need for multimodal imaging platforms that would result in improved clinical practice.

The use of wireless resonant devices is a promising approach to mark implantable devices preventing the need for multimodal imaging. MRI performance of these wireless markers is loosely dependent on the imaging parameters (e.g., TR, TE and pixel volume). However, this class of devices calls for novel resonator designs for proper operation. Physical dimensions of these markers together with RF safety concerns should be considered for the surrounding tissues [20]. Decreasing RF power is a good practice to protect patients from the harmful effects of RF exposure but this lowers SNR on the acquired MR images and decreases the reliability of the images for diagnosing purposes especially for the regions with lower proton densities.

In this thesis work, we designed and demonstrated an innovative self-resonating structure that is intended to alleviate the aforementioned complications of the previous works in the literature. This proposed structure can be used as a wireless MRI marking device for potential in-vivo studies such as marking of subdural electrodes. Although it was demonstrated to mark the subdural electrodes as a proof of concept in this thesis work, characterization results show that it is not limited to MRI applications but also other wireless applications including miniaturization of wireless devices and improving the performance of conventional structures with field localization.

Here we address the scientific challenge of achieving low footprint area and high Q-factor at the same time for 123 MHz of self-resonance frequency. As a proof of concept demonstration we achieved an 8 mm $\times$ 8 mm footprint area with a free-space Q-factor of about 80 for the given operational frequency. We also report the simulation results of specific absorption rate (SAR) increase in brain. MR images support that the proposed architecture is a potential candidate for various applications including MRI marking of implants, high-resolution MR imaging and E-field confinement for lossy medium applications. These features may open up new possibilities for the next-generation implants as wells as for new sensing systems.

1.2 Organization of the Thesis

This thesis starts with a short introduction to MRI presenting its fundamental operating principles and imaging methods (Chapter 2). This brief introduction prepares readers to be familiar with the relationship between the material types and their MRIs. The thesis continues with explaining the electromagnetic fields of MRI and their coils for imaging. A relatively detailed analysis of RF fields emphasizes the importance of resonance for MRI.

In Chapter 3, methods of achieving deep-subwavelength resonance are analyzed and for the proposed thin-film loaded helical metamaterial architecture with comparison to conventional devices reported in the literature. Here, a equivalent circuit model is also provided to estimate the characteristics of the proposed structure in this chapter. Numerical studies are reported to verify the results of this equivalent circuit model. Superiority of the proposed architecture (in terms of Q-factor, tuning performance, electric and magnetic fields, and the loading performance) over conventional structures (such as ring resonators, split-ring resonators and stacked resonators) are also discussed in a comparative manner. The microfabrication of the proposed devices is explained with necessary recipes to highlight the suitability of the proposed architecture for mass-production. Experimental RF characterization of the microfabricated resonators and numerical simulations of the proposed structures are included in the end of this chapter.

Chapter 4 introduces the experimental MRI characterization of the proposed resonator for various imaging configuration. Intensity distribution maps are provided for qualitative analyses followed by more quantitative characterization methods including B1 mapping, SNR mapping, specific absorption rate and thermal analyses under MRI. This part also includes an experimental 1.5 T study for a proof of concept demonstration.

Next, Chapter 5 exploits some of the MRI problems frequently dealt with in clinical environment. These include MRI marking of implantable devices (subdural electrode marking for epilepsy treatment), SNR improvement for high-resolution MRI applications and SNR improvement for extremities. Multimodal imaging potential of the proposed architecture (such as imaging of this MRI compatible architecture with an x-ray platform) is explored to show a proof of concept demonstration. Finally, in Chapter 6 the thesis is completed with concluding remarks, future outlook and a summary of the contributions of the author to the literature.

Chapter 2

Basics of MRI

Early history of NMR, which has led scientists to invent MRI, starts with the definition of Larmor frequency. Joseph Larmor (1857), an Irish physician, found a formula to define the relationship between the external magnetic field and the rotational frequency of a spin as given in Equation (2.1).

$$w = \gamma B \tag{2.1}$$

Here, B is the magnetic field intensity (T), γ is the gyromagnetic ratio (Hz/T) and ω is the angular frequency (rad/s) of the nuclei. Sensitivity of an atom is defined as the ratio of MRI signal emitted from an atom to the excitation signal. It is depicted that the MRI sensitivity of ^1H is the highest compared to any other atom [29]. Abundance of ^1H atoms in tissues, together with its higher sensitivity, makes ^1H the strongest candidate to be used for clinical MRI applications. This dominant character of ^1H also has affected the MRI instrumentation with its specific resonance frequency characteristics. A clear understanding of NMR is necessary to figure out the basic principles of MRI, which is described as the behavior of a nucleus under a certain magnetic field. Although the details of NMR can be accurately explained by quantum mechanics, classical mechanics can also be used to illustrate this phenomenon. Here, we will use a hybrid approach to explain necessary details of NMR.

^1H atom will possesses a spinning frequency determined by external magnetic field as described in Equation (2.1). In a non-magnetized tissue, these spins are randomly oriented with a zero net magnetization. Rotation direction of these spins follows the left-hand rule as depicted in Figure 2.1.a. An external magnetic field would align some of these atoms rotation axes parallel to the external magnetic field, which would then push these spins into a lower energy state (Figure 2.1.b). Any subject (living tissues, phantoms etc.) would thus be magnetized due to the applied direct-current (DC) magnetic field (B_0) and this is schematically illustrated in Figure 2.1.c.

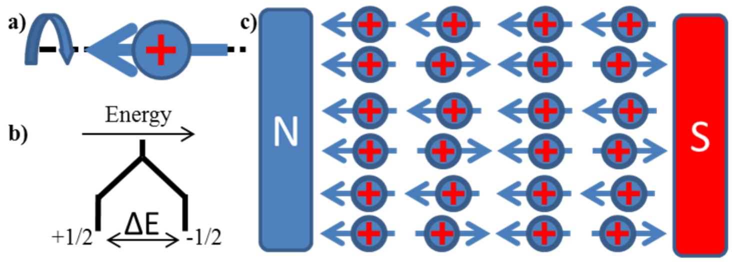

Figure 2.1: Illustration of a spin (a), its quantum mechanical representation to explain energy levels (b) and a schematic of a tissue under external DC magnetization (c).

Following this picture, any perturbation, (e.g., excitation by using RF fields) will allow spins to leave their state to move to upper energy state. Number of excited spins depends on the energy of excitation that finally determines the imaging signal strength. Energy difference of an excited spin can be formulated by Equation (2.2).

$$\Delta E = \frac{h}{2\pi} w \tag{2.2}$$

Here, h is the Planck's constant. Instead of defining this microscopic quantity, classical mechanics defines a macroscopic term called total magnetization (denoted by M_0) to quantify the material′s magnetic response as a whole.

Once a spin (or equivalently a macroscopic material) is excited to a higher energy state (e.g., by using an RF wave), it releases its energy to go back to its low energy state. Although the resonance frequency of all ^{1}H atoms are the same (while fat-shift type exceptions are always possible), energy release of a spin is strongly dependent on its interaction with the neighboring atoms, which results in different T1 and T2 durations. These characteristic parameters are mostly used to obtain the material classification in NMR. Similarly, MRI uses this property to obtain higher contrast between different tissues.

Although relaxation parameters are strong clues for material classification, they are not enough for imaging. This requires additional engineering of electromagnetic waves, called gradient fields. In addition to DC fields for magnetization of tissues and RF fields for perturbation of spins, gradient fields cause local magnetic field intensity variation to allow spins to rotate at slightly different frequencies. Thus, the frequency encoding of the acquired signals results in spatially decoded data, called magnetic resonance image.

2.1 Electromagnetic Fields and Hardware of MRI

As discussed earlier, ^{1}H atom, which is abundant in all organic tissues, plays the key role in determining the operating MR frequency with its specific gyromagnetic ratio (γ = 42.58 MHz/T). Commercially available MRI scanners with B_0 field strengths from 0.1 to 4 T with the corresponding hydrogen resonance frequencies from 4.26 to 170 MHz are used for todays clinical applications . In addition to clinical MRI scanners, NMR scanners with B_0 field strengths of up to 25 T are used for material identification.

Depending on typical B_0 values of scanners, the imaging frequency falls within the RF range where the tissue absorption of electromagnetic (EM) power is conveniently very low (e.g., compared to X-ray imaging). The photography of a 3 T Siemens Tim Trio scanner, which was located at National Magnetic Resonance Research Center (UMRAM [30]), is provided in Figure 2.2. Traditional MRI systems provide three different magnetic fields known as DC, gradient and RF fields that are created by three different coil systems.

2.1.1 Direct Current (DC) Field and Its Coil (or Magnet)

In opreation, rotation axes of the spins are oriented in the direction of DC magnetic field. Magnetization vector of nuclei under the DC magnetic field B_0 will point the given B_0 direction. This configuration, quantum mechanically, means to have a lower energy state for the spins, resulting in nonzero net macroscopic

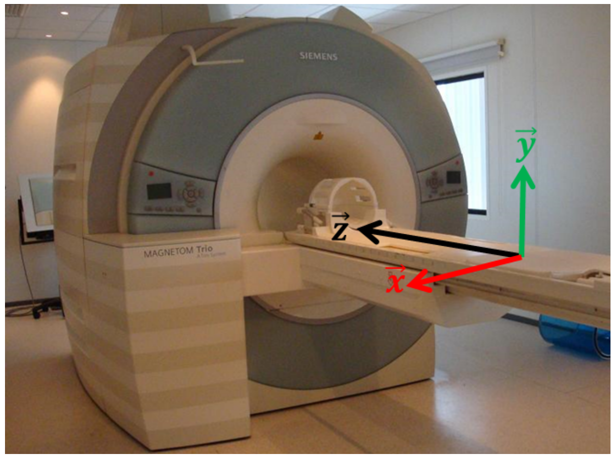

Figure 2.2: A 3 T Siemens Tim-Trio Imaging System located at UMRAM.

magnetic moment (M_0). For the sake of reference, direction of B_0 is commonly taken as the $\hat{z}$ direction; hence B_0 notation will be used to refer to $\mathbf{B_0}$. Here, it is worth pointing out that the given B_0 field does not cause any excitation to spins. At this point, any subject under DC field will only have magnetized spins rotating with a given Larmor frequency (see Figure 2.1.c).

DC magnetic field strength determines the resonance frequency of the given MRI system, which is considered as the identity of the system. Since permanent magnets cannot exhibit higher field strengths, they are mostly used for open coil scanners employed for the patients with claustrophobia. For higher field strengths (e.g., above 0.5 T), an electromagnet, which is most commonly in the form of a superconductor solenoid coil, is used for DC field creation [31]. As a last remark, these coils should be continuously working during the scanner lifetime. Hence, they are never turned off after regular operation.

2.1.2 Gradient Fields and Their Coils

After proper excitation of materials, which will be explained in the next section, classification of these materials can be achieved by using characteristic coefficients such as γ, T1 and T2. To obtain proper imaging signal, a relationship between space and signal should be achieved. Any spatial non-uniformity in the DC magnetic field will result in different resonance frequencies for the consecutive spins, resulting in non-zero bandwidth for the acquired signals. Corresponding resonance frequency differences will be used to map spins in frequency domain. The frequency spectrum of the acquired signals will be converted to space domain images by using Fourier transform.

This phenomenon was first proposed by Paul Christian Lauterbur and Peter Mansfield that introducing gradient fields into the imaged medium would make it possible to acquire the locations of emitted signals. It was the beginning of 70s when Lauterbur first obtained the first medical MRI image [1]. The detailed mathematical expressions related to the gradient fields and RF excitation can be found in [29].

To provide an arbitrary slice selection profile, gradient coils should be designed in such a way that the gradient fields can be applied in any direction with any amplitude. This is achieved by using different gradient coils for different directions. Arbitrary slice selection profile can be achieved by proper control of these coils; hence, these coils should be turned on and off very quickly. Dimensions of these coils are comparable with the DC coils, and thus they have very high inductance that can create high voltages in the case of instant current deviations. Sophisticated circuitry and various physical designs including shielding of coils are used to provide solutions to these problems [32].

2.1.3 Radio Frequency (RF) Fields and Their Coils

Time-varying electromagnetic fields, called RF fields, are used for the excitation of spins. Without RF fields, we only have the magnetized spins (due to DC magnetic field), with proper frequency encoding (due to space-dependent gradient fields). In addition to spinning of nuclei with Larmor frequency, an additional rotation movement of these spins is added to the system with the same frequency. Now the combination of these two movements, namely the rotation along with the B_0 direction and spinning along with the rotation direction, results in coherent signal emission from the magnetized material.

This is illustrated in Figure 2.3 that the overall magnetization of spin is now divided into two parts, namely longitudinal ($\vec{M}_z$) and transverse magnetization

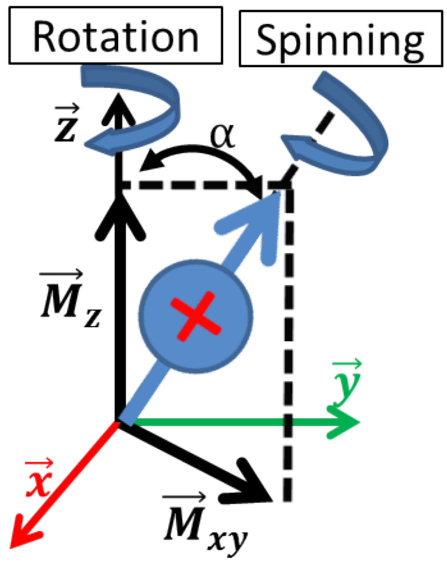

Figure 2.3: Illustration of an excited spin with non-zero transverse (xy) and longitudinal (z) magnetization vectors.

($\vec{M}_{xy}$) as expressed in Equation (2.3).

$$\vec{M}_0 = \vec{M}_z + \vec{M}_{xy} \tag{2.3}$$

where, $\vec{M}_{xy}$ can be decomposed into its components as given in Equation (2.4):

$$\vec{M}_{xy} = M_x\hat{i} + M_y\hat{j} \tag{2.4}$$

Here, $\vec{M}_z$ will determine the amount of signal that will be captured by the receiver antennas. The received signal, also named as the relaxation signal, will last for a certain amount of time. The energy stored in the excited material will be released by the relaxation of the nuclei for a finite period of time. The Bloch equation to define the overall magnetization in time domain is given by Equation (2.5):

$$\frac{d\vec{M}}{dt} = \vec{M} \times \gamma\vec{B} - \frac{M_x\hat{i} + M_y\hat{j}}{T2} - \frac{(M_z - M_0)\vec{k}}{T1} \tag{2.5}$$

where $\vec{M}$ is the overall magnetization, $\vec{B}$ is the effective magnetic field strength,γ is the gyromagnetic ratio of the nuclei, M_0 is the initial magnetization due to static magnetic field, T1 is the longitudinal relaxation time constant and the T2 is the transverse relaxation time constant for the materials. By assuming that the transverse and longitudinal magnetization vectors are decoupled from each other, Equation (2.5) can be solved by separating these two scalar differential parts as given in Equation (2.6) and Equation (2.8):

$$\frac{dM_z}{dt} = -\frac{M_z - M_0}{T1} \tag{2.6}$$

with a solution, after 90 ° excitation:

$$M_z(t) = M_0(1 - e^{-t/T1}) \tag{2.7}$$

and

$$\frac{dM_{xy}}{dt} = -\frac{M_{xy}}{T2} \tag{2.8}$$

with a solution, after 90 ° excitation:

$$M_{xy}(t) = M_0 e^{-t/T2} \tag{2.9}$$

Time-invariant magnetic field in the z-direction results in the recovery of initial magnetization after a certain amount of time. Similarly, transverse magnetization will die out after a certain amount of time due to the emission of magnetic resonance signal. Typical relaxation signals for some of the tissues are given in Table 2.1 for both 1.5 and 3 T magnetic field strengths [29].

Table 2.1: Typical relaxation parameters of different tissue types under different magnetic field strengths.

	1.5 T		3 T	
Tissue	T2 (ms)	T1 (ms)	T2 (ms)	T1 (ms)
Gray matter	100	900	100	1820
White matter	92	780	70	1084
Muscle	47	870	45	1480
Fat	85	260	83	490
Liver	43	500	42	812

Here, we can see that the T2 parameters of various types of tissues are more or less the same for different field strengths, which shows that the transverse relaxation is mainly dependent on material type and intermolecular interactions rather than the field strength. On the other hand, T1 relaxation is strictly dependent on the field strength that is reasonable due to the effect of main magnetic field on longitudinal direction. As an example, the longitudinal and transverse relaxation

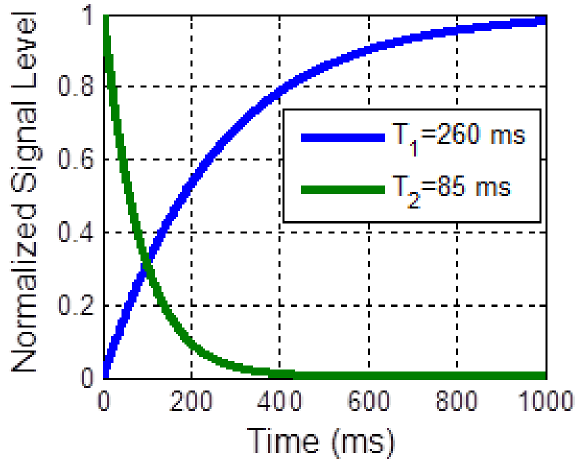

Figure 2.4: Longitudinal and transverse magnetization of a fat tissue for 1.5 T normalized to initial magnetization.

signal levels of a fat tissue for 1.5 T, normalized to initial magnetization, are presented in Figure 2.4 for visualization.

Excitation of spins and consequent collection of emitted signals from tissues are achieved by using RF coils. The former is achieved via transmitter (Tx) coils and latter is performed by using receiver (Rx) coils. Field distribution of these coils has significant importance on image quality; hence, they are positioned inside the other coils in order to be isolated as much as possible. Although every scanner has at least one body coil for RF signals, they are also capable of using additional RF coils for special purposes such as chest, neck, head, and knee coils. These special coils are designed to obtain the MRI of specific body parts with the highest possible SNR and lowest RF power excitation for the rest of the body parts.

A circularly polarized plane wave can be used to excite the spins uniformly in a certain volume to achieve an undistorted magnetic resonance image. Since a plane wave cannot be created by an antenna of finite size in a limited distance, the aforementioned special RF coil designs are required for generating uniform field distributions of finite volumes. These RF coils should have proper geometries to enable uniform magnetic field distribution for a region of interest (ROI), high Q-factors for SNR improvement and suitable mechanics to physically fit body parts.

Although several coil geometries for different body parts have been already designed for ex-vivo MRI, in-vivo coil designs are limited due to the difficulties of achieving low resonance frequencies for small sizes and providing high enough Q-factor in loaded scenarios.

To obtain the magnetic field distribution of a coil with a current distribution of $\vec{J}$, one has to solve the Equation (2.10) for every point in space ($\vec{R}$).

$$B(\vec{r}) = \frac{\mu_0}{4\pi} \int \frac{\vec{J} \times \vec{R}}{R^3} \tag{2.10}$$

For Tx coils, current distribution can be obtained relatively easily due to the known conductive geometry of the coils. But, the calculation of induced currents on receiver coils and tissues does not have closed form solutions for most of the geometries; thus, the use of numerical methods is unavoidable to derive magnetic field distribution of different coil geometries.

Chapter 3

Design and Demonstration of a Deep Sub-Wavelength Wireless Resonator

Designing wireless devices in the form of resonators is of significant importance for in-vivo applications. These devices can be used for different purposes including in-vivo strain sensing [33, 34, 38], stent lumen visualization [19], marking of implantable devices [18], miniaturization of antennas [39] and SNR improvement in their close vicinities [40]. Squeezing the electrical size of a resonator down to 1/1000 of its free space wavelength ($\lambda_0/1000$) is, however, a challenging task. One can consider different methods for this purpose including lumped element loading [41], introducing additional turns for spirals [39], stacking different layers [42] and creating thin-film capacitances [43]. Although these methods are acceptable for most of the conventional applications (e.g., printed circuit board devices, tuning of antennas, waveguides, wired systems and on-board radiative elements), in-vivo devices requirea a complex set of properties and functionalities including bio-compatibility, flexibility, elimination of lumped elements, field confinement for safer operation, stable operation under lossy medium loading and proper magnetic field manipulation for MRI among others [44].

We found that all of the above difficulties and complications can be addressed by conceiving and developing a new class of helical ring resonators, which are expected to be easy to fabricate. Potential applications including in-vivo MRI marking and SNR improvement can be achieved in certain MRI studies using this class of resonators [45–48]. A schematic of the proposed design is given in Figure 3.1.

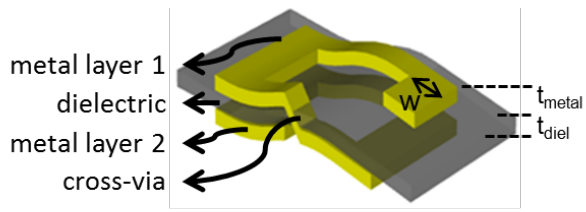

Figure 3.1: Schematic representation of the proposed helical ring resonator.

Following sections provide the detailed analyses of the proposed architecture, starting from miniaturization to experimental RF characterization along with detailed numerical studies for better understanding of electromagnetic operation.

3.1 Achieving Deep Sub-Wavelength Resonance

Full-wave solutions are useful for providing a physical explanation to the operating principles of resonators. This is also a cheap and convenient way to validate a model before its fabrication. Traditional split-ring resonators (SRR) are analyzed for their resonance frequencies (f_0) to compare the results with the proposed architecture. Schematics of the analyzed architectures are given in Figure 3.2.

To make a fair comparison among these different designs (e.g., circular and rectangular resonators, circular and rectangular SRRs, and proposed helical split-ring resonator architecture), we set the footprint area to 8 mm $\times$ 8 mm (side length, a, equal to 8 mm for rectangular ones and outer radius equals to 4 mm for circular ones), metallization thickness, t_{metal}, of 10 μm, a gap width, g, of 0.5 mm and a metallization width, w, of 1 mm. Here, a polyimide material from the numerical solver library is used as the dielectric layer with a variable thickness ($t_{dielectric}$) and gold (Au) is used as the metal layer with a variable metallization width (w).

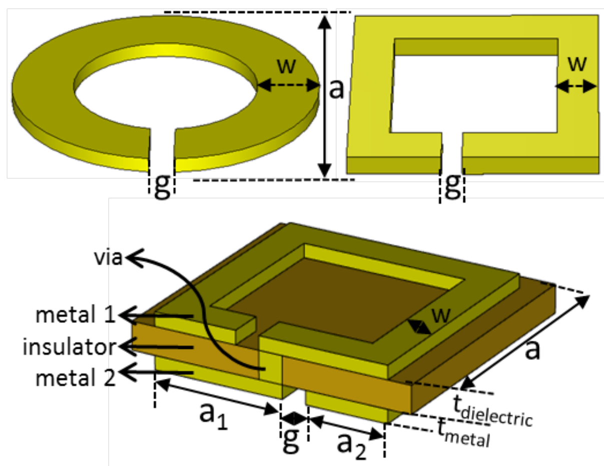

Figure 3.2: Schematics of the analyzed structures designed in the same footprint area (a×a) with a metallization width of w, a metallization thickness of t_{metal} and a gap width of g. In addition to these parameters, the proposed architecture (bottom) has a dielectric thickness of $t_{dielectric}$.

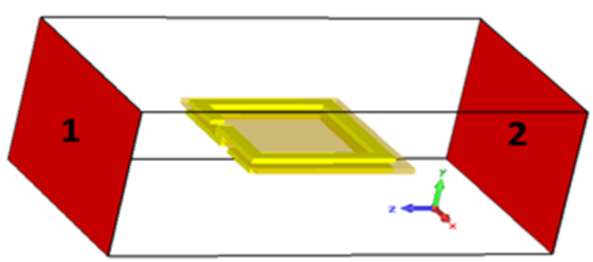

Figure 3.3: Simulation environment to obtain RF and EM characterization of the analyzed structures.

For numerical solutions, we used CST-Design Studio^{TM} (Darmstadt, Germany) to acquire scattering parameters and deduce resonance frequency from these scattering parameters. Figure 3.3 depicts the simulation environment for the proposed structure with two ports located in the z-direction and labeled as 1 and 2 consecutively. To obtain the resonance frequency of the wireless resonators, we used two wave-guide ports to acquire scattering parameters (S_{11} and S_{21}), with boundary conditions of perfect-electrical-conductor (PEC), perfect-magnetic-conductor (PMC) and perfectly matched layer (PML) in x, y and z directions, respectively. Simulation environment was extended with the side length of the resonator (e.g., 8 mm in this case) in all directions.

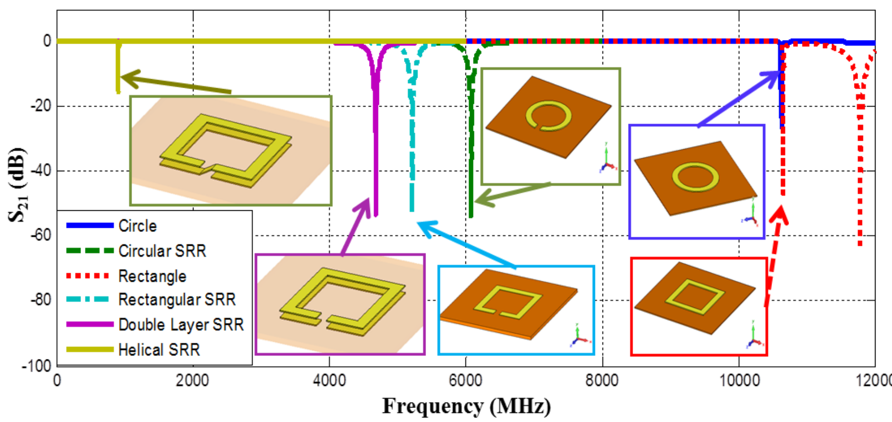

Figure 3.4: Resonance frequency comparison of different structures. Circle and rectangle resonators have the same f_0 of 10.6 GHz. On the other hand, circular and rectangular split-ring resonators (SRR) have the corresponding f_0 of 6.1 and 5.2 GHz, respectively. A double layer SRR structure, with a 0.5 mm polyimide dielectric thickness, has the f_0 of 4.7 GHz and adding a cross-via metallization drops this resonance frequency to 0.9 GHz. There is a clear one-order-of-magnitude shift compared to conventional resonators and 5-folds decrease compared to SRRs and double layer counterparts.

With this simulation environment, incident transverse-electromagnetic (TEM) waves (from Port 1) was coupled to the resonator that is strongly confined inside its dielectric region and re-emits this EM energy back to the environment resulting in intense field distribution in its vicinity. For the frequencies far from the resonance frequency of the resonator, TEM wave penetrates through the resonator and behaves as if there is almost no loss between the ports ($S_{21} \rightarrow 0$ dB). However, near the resonance frequency, a large amount of energy is stored on the resonator to be radiated back to the space, resulting in decrease in transmission parameter (S_{21} <0 dB). From the dip of S_{21}, we can clearly determine the resonance frequency of the resonator. Figure 3.4 depicts the results for comparison.

Here, conventional circular and rectangular resonators have the same resonance frequency of 10.6 GHz, which is due to the traveling wave mode of the E-field. On the other hand, creating a gap region results in different resonance frequencies for these resonators as reported earlier [49]. These are 6.1 and 5.2 GHz for the circular and rectangular SRRs, respectively. The mean electrical path for the induced wave is different for these two geometries, which leads to different resonance frequencies. For the stacked double-layer rectangular resonator configuration, thin-film capacitance between consecutive layers becomes dominant and decreases the resonance frequency of the overall structure. In addition to thin-film capacitance, mutual coupling of these consecutive layers can be increased by adding a cross via metallization to the system. Thus, resulting in much lower resonance frequency, that is about 5 times (4.7/0.9=5.2) lower compared to the stacked geometries [51]. These results are summarized in Table 3.1.

Table 3.1: Comparison of conventional resonators in terms of electrical size and resonance frequency for wireless operation.

Resonator Type (8 mm × 8 mm)	Resonance Frequency (GHz)	Free Space Wavelength (λ_0, mm)	Electrical Size
Circular	10.6	28.2	$\lambda_0/3.5$
Rectangular	10.6	28.2	$\lambda_0/3.5$
Circular SRR	6.1	49.3	$\lambda_0/6.2$
Rectangular SRR	5.2	57.7	$\lambda_0/7.2$
Stacked SRR	4.7	64.1	$\lambda_0/8.0$
Helical SRR	0.9	327	$\lambda_0/41.0$

The obvious miniaturization property of the proposed architecture makes it the strongest candidate among other structures for in-vivo applications. To apply equivalent circuit models, electrical size of a structure should be well below (e.g., 10 times) of its free space resonance frequency. The most suitable structure, to be modeled by using equivalent circuits, is the proposed helical SRR geometry. Although there are several articles in the literature to model SRRs with suitable equivalent circuits [49, 50], they are not suitable for the proposed architecture in here due to its dominant thin-film characteristics and increased mutual coupling.

Hence, the equivalent circuit model of the proposed helical SRR with distributed thin-film loading scheme is derived from the scratch.

The superiority of the presented architecture compared to conventional structures motivates us to continue our systematic study to investigate its characteristics in detail. To understand the effect of $t_{dielectric}$ and w on the resonance frequency, they were systematically swept over a range of values. Figure 3.5 shows the behavior of the proposed architecture for the same footprint area that was given previously and with a polyimide dielectric thin film with different thicknesses.

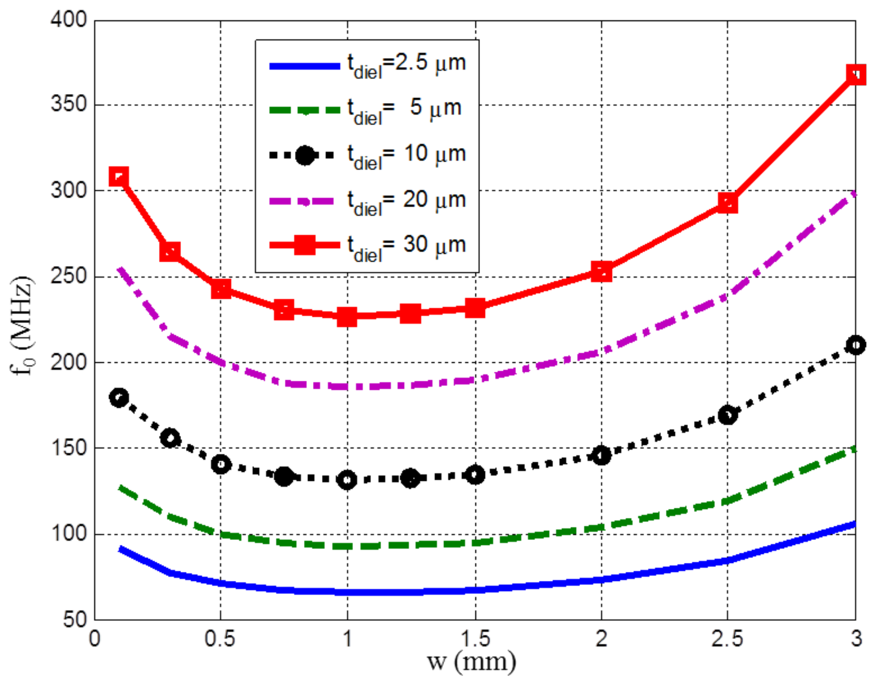

Figure 3.5: Frequency characterization of the proposed architecture with different dielectric thicknesses and metallization widths. Although dielectric thickness has a monotonous effect on the resonance frequency, metallization width has a non-linear effect on it.

Figure 3.5 shows that decreasing the dielectric thickness allows us to reach the lower range of resonance frequencies. When we compare these results with the previous results (500 μm dielectric thicknesses with 1 mm of w leading to 918 MHz), here, 5 μm dielectric thickness with the same metallization width results in 94 MHz resonance frequency. Results show that the resonance frequency of the structure is linearly proportional to the square root of the dielectric thickness ($f_0 \propto \sqrt{t_{diel}}$).

On the other hand, increasing the metallization width does not yield a monotonous contribution to the resonance frequency. For an infinitely thin metallization width, we do not expect any thin-film capacitance; hence, a higher resonance frequency can be acceptable. When we start increasing the metallization width, we introduce thin-film capacitance to the structure, which is the main reason of lower resonance frequency. On the other hand, according to the asymptotical equation of inductance ($L_{eff} \propto ln(\frac{l}{w+t_{metal}})$), logarithmic term becomes dominant and the effective inductance terms starts to decrease. According to Equation (3.1), combination of these two effects (increase in thin-film capacitance and decrease in effective inductance) generate a minimum f_0. For the Figure 3.5, we observed that the minimum resonance frequency can be achieved for the 1 mm of metallization width. It can be concluded that the w/a ratio of 0.125 is an optimal point for rectangular and circular helical resonators to achieve the lowest resonance frequency.

3.2 Circuit Theory Approach

For the electrical sizes of less than 1/10th of the operating wavelength (e.g., for a resonator with a side length $< \lambda_0/10$), circuit theory approach can be used to determine the initial characteristics of a resonator. Proper modeling of effective inductance (L_{eff}) and effective capacitance (C_{eff}) is enough to predict the resonance frequency of a resonator, whereas the modeling of effective resistance (R_{eff}) is necessary for Q-factor determination. Traditional split-ring-resonator (SRR) designs are modeled with an effective inductance of single turn (L_{eff}) and effective capacitance of the overall geometry (C_{eff}).

Although asymptotic formulations for the determination of L_{eff} is proposed for most of the geometries [52], pre-determination of effective capacitance is not that simple due to gap dimensions, fabrication imperfections, frequency dependent field localizations on resonators, and fringe field calculation deficiency between metallization layer and substrate. Since a larger capacitance is required to lower the operating frequency of a resonator, these problems become more dramatic, due to the dominant effect of capacitance.

Here, we modeled the proposed design as a series resonator with effective parameters of L_{eff}, C_{eff} and R_{eff}. Resonance frequency, f_0, of such a resonator is given by Equation (3.1):

$$f_0 = \frac{1}{2\sqrt{L_{eff} C_{eff}}} \tag{3.1}$$

and the Q-factor is given by Equation (3.2):

$$Q = \frac{2\pi f_0 L_{eff}}{R_{eff}} = \frac{1}{R_{eff}} \sqrt{\frac{L_{eff}}{C_{eff}}} = \frac{f_0}{f_{3dB}} \tag{3.2}$$

where f_{3dB} is the full-width-half-maximum (FWHM) bandwidth of the resonator. To design a resonator with higher Q-factors, it is necessary to increase effective inductance and decrease the effective resistance and capacitance. For a given frequency, f, effective RF resistance can be calculated using Equation (3.3):

$$R_{eff} = \frac{l}{W\sigma\delta(1 - e^{-t_{metal}/\delta})} \tag{3.3}$$

where l is the mean path length along with the resonator, W is the metallization width, t_{metal} is the thickness of the metallization, σ is the conductivity of the metal used for fabrication, and δ is the skin-depth of the metal for the given frequency, which is formulated as in Equation (3.4):

$$\delta = \sqrt{\frac{2}{2\pi f \mu \sigma}} \tag{3.4}$$

Effective inductance can be defined as the amount of magnetic energy stored in a volume for a given current distribution. Its analytical formulation is given by Equation (3.5):

$$L_{eff} = \frac{1}{I} \oint_S \mathbf{B} \cdot \mathbf{dS} \tag{3.5}$$

where I is the current on the conductor, $\mathbf{S}$ is the surface area covered by the resonator itself and $\mathbf{B}$ is the magnetic flux density passing through the surface $\mathbf{S}$. A proper inductance formulation for a rectangular loop is given by Equation (3.6) [52]:

$$L_{eff} = \mu_0 \mu_r \; l \; [ln(\frac{l}{W + t_{metal}}) + 1.193 + \frac{W + t_{metal}}{3l}] \tag{3.6}$$

where μ_0 is the permeability of the free space and μ_r is the relative permeability of the material used for resonator fabrication (which has to be unity for MRI operation), W is the metallization width and t_{metal} is the metallization thickness for the planar inductors. When the above equation is dimensionally analyzed, for the constant W and t_{metal}, the relationship between the inductance and side length of a resonator becomes as given in Equation (3.7):

$$L \propto l \; ln(l) \tag{3.7}$$

Equation (3.7) reveals the main point for higher inductance values. If the size of a resonator is longer, its inductance, thus the Q-factor, becomes higher. Therefore, having higher Q-factors using smaller resonator footprint area is a challenging task due to this limitation.

Effective capacitance of a resonator strictly depends on the metallization geometry and the ground plane location. For the resonators without clear ground plane, e.g., SRRs fabricated on insulators, effective capacitance comes from the summation of lumped elements (lumped capacitors if they exist) and thin-film capacitances (due to gap region and metallization surface). From circuit theory approach, increasing capacitance is not desired due to the effect of decreased Q-factor, but it is necessary to achieve lower resonance frequencies. Hence, proper engineering of capacitive regions have critical importance.

Capacitance of a structure can be defined as the total amount of stored electric charge (Q) for a given potential difference (V) and can be calculated by using Equation (3.8):

$$C_{eff} = \frac{Q}{V} = \epsilon_0 \epsilon_r \; \frac{A}{d} \tag{3.8}$$

where ϵ_0 is the permittivity of the free space and ϵ_r is the relative permittivity of the dielectric used for electric field localization, A is the parallel plate surface area, and d is the distance between the plates with the voltage difference. Effective capacitance can be reformulated, in terms of geometric parameters, for the microfabricated resonators as given in Equation (3.9):

$$C_{eff} = \epsilon_0 \epsilon_r \; \frac{W \; l}{d} \tag{3.9}$$

Here, the value of d is ambiguous for a single-layer resonator due to ground plane representation. Thin-film capacitance of a single layer resonator fabricated onto a dielectric is negligible due to missing ground plane. Hence, resonance frequency of such a resonator mostly depends on the capacitance due to gap region.

To overcome the size problems for low frequency operation, different methodologies can be used including creating spirals [39, 53], multi-turn SRRs, stacked resonators [42] and helical geometries [54]. Spirals have larger inductances due to mutual coupling of consecutive loops, but this coupling decreases as the inner loops become smaller. The effective capacitance of spirals is also not high due to their electric field distribution. Hence, Q-factor and resonance frequency of spirals are not suitable for in-vivo applications. Similarly, multi-turn SRRs have the same features with spirals with lower inductances [42]. Hence, their applicability to clinical MRI problems is not possible in the near future.

Stacked resonators have the advantage of increased thin-film capacitance and increased inductance due to their geometries. However, helical resonators beat the stacked geometries in all aspects due to their increased inductance (mutual inductance of a helical resonator is higher than that of stacked resonators) and increased distributed thin-film capacitance (thin-film capacitance of a helical ring is much higher than that of stacked resonators). Stacked resonators without any connection among consecutive layers cannot create necessary current distribution to increase mutual coupling between its different layers and cannot have the necessary voltage differences to confine electric field among its consecutive layers to create thin-film capacitances. Hence, helical ring geometries become the most promising candidate among all resonator configurations to achieve lower resonance frequencies and higher Q-factors simultaneously.

To analyze the proposed helical resonator architecture, we first sectioned the geometry with the effective unit-cell parameters of dR for resistance, dL for inductance, dC for capacitance and M mutual coupling between consecutive layers. Discretization of the proposed structure is schematized in Figure 3.6.

Discretization of the given resonator allows us to analyze its resonance frequency and Q-factor by considering all of its geometrical parameters, instead of just equivalent circuit value of the overall structure. Proposed method, namely unit-cell discretization, can also be used for different geometries such as circular helical rings. Figure 3.7 shows a discretized circular helical ring with a reversed

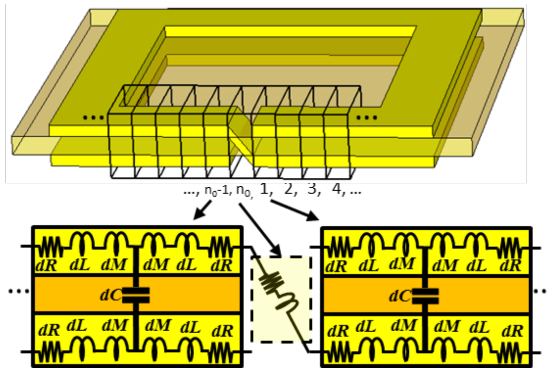

Figure 3.6: Schematic representation of a rectangular two-turn helical resonator and its equivalent circuit model for a given unit cell.

cross-sectional metallization using n_0 number of discretized elements.

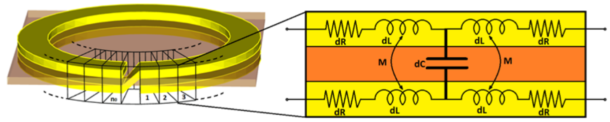

Figure 3.7: Schematic representation of a circular two-turn helical resonator and its equivalent circuit model n_0 unit cells.

Unlike traditional stacked SRRs, here the first and the last n_0^{th} elements are connected by using a via-metallization. This is the most critical element of the proposed architecture to increase its mutual inductance between consecutive layers and to increase the electric field confinement in the stacked dielectric region. By using this cross via-metallization, we obtain a positive mutual coupling, M, which increases the effective inductance drastically. Here, the value of M is the same as the value of dL due to strong coupling between consecutive layers.

Starting from the first unit cell, node voltage method can be applied to solve for the input impedance of overall structure. To do this, unit cells are labeled starting from 1 to n_0. Each unit cell is represented by using two different voltage nodes (for the i^{th} unit-cell, V_i and V_{i+n_0} represent the voltages of bottom and upper nodes, respectively). All of the unit cells are cascaded to consecutive ones except the first and last ones, which are connected to each other with a via-metallization. Circuit theory modeling of the proposed geometry results in the set of Equations (3.10-3.12):

$$V_1(-\frac{1}{2\ Z_L}+\frac{1}{Z_C})+V_2(\frac{-1}{4\ Z_L})+V_{n_0+1}(\frac{-1}{Z_C})=\frac{V_0}{2\ Z_L}, for\ i=1 \tag{3.10}$$

$$V_{i-1}(-\frac{1}{Z_L}) + V_i(\frac{1}{Z_L} + \frac{1}{Z_C}) + V_{i+1}(-\frac{1}{2\ Z_L}) + V_{i+n_0}(-\frac{1}{Z_C}) = 0, for\ 1 < i < n_0 \tag{3.11}$$

$$V_{n_0-1}(-\frac{1}{2\ Z_L}) + V_{n_0}(\frac{5}{6\ Z_L}) + V_{n_0+1}(-\frac{1}{3\ Z_L}) = 0, for\ i = n_0 \tag{3.12}$$

where V_0 is the applied input voltage to acquire input impedance of the structure, and Z_C and Z_L are the characteristic impedances of the unit-cell capacitance and inductances, respectively. To obtain the input impedance of the resonator, one has to solve Equation (3.13):

$$V[Y] = I \tag{3.13}$$

where V and I are the voltage and current vectors (with vector lengths of $2n_0$) and Y is a matrix, which is banded with the band size of n_0 due to mutual coupling elements, resulting in a matrix size of $2n_0$ by $2n_0$. For a resonator with an incomplete-turn ratio, $2n_0$ terms will be replaced by $n_0 + n$, where the n is the number of elements with double layer.

To verify the validity of the derived equations, we designed a two-layer circular resonator with a radius of 4 mm, a metallization width of 1 mm, a metallization thickness of 10 μm, a dielectric thickness of 7.5 μm, and a relative dielectric permittivity of 2.1. A MATLAB routine was coded to understand the effect of discretization number, n_0, on the simulation results. Figure 3.8 shows the effect of n_0 on the input impedance level and the resonance frequency estimation. For the given geometry, we have a 19.5 nH of inductance and 1.05 Ω resistance for the single turn and a thin-film capacitance of 70.1 pF. By using lumped element model of the first order, these values will result in a resonance frequency of 135.1 MHz and a Q-factor of about 16.8.

From Figure 3.8, we can see that the resonance frequency of the studied architecture is about 120 MHz and computational results depend on the discretization order (n_0). Table 3.2 summarizes the results obtained by using the proposed circuit-model for the given geometry (a radius of 4 mm, a metallization width of 1 mm, and a dielectric thickness of 7.5 μm).

Here, we found that the increasing the discretization number of the proposed architecture converges to the resonance frequency of 116.2 MHz and the Q-factor

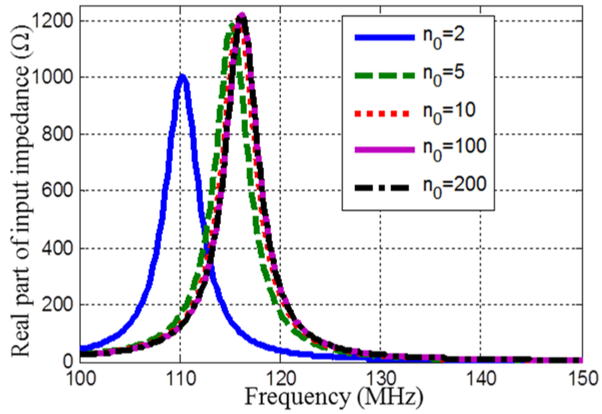

Figure 3.8: Real part of the input impedance for the double-layer helical resonator.

Table 3.2: Numerical results of the proposed equivalent circuit method for double-layer helical resonator using different discretization order (n_0).

n_0	Resonance Frequency (MHz)	f_{3dB} (MHz)	Q-factor	Computation Time (s)
2	110.2	2.6	42.4	0.019
5	115.4	2.4	48.1	0.069
10	116.0	2.5	46.4	0.128
100	116.2	2.6	44.7	4.8
200	116.2	2.6	44.7	25.6

of about 44.7. We also observed that using conventional equations of resonance frequency (Equation (3.1)) and Q-factor (Equation (3.2)), do not yield correct results due to the nature of the proposed architecture. Since we have a thin-film loaded geometry, it will neither behave like a simple series resonator, nor a parallel resonator. It is more like a cascaded RLC circuit with proper feedback (in the electrical model, which corresponds to a physical connection called via-metallization) to provide better resonance behavior in terms of the feasible sets of resonance frequency and Q-factor. Hence, instead of using a simple RLC equivalent circuit, the proposed circuit model characterizes the behavior of our structure more correctly.

In addition to convergent and correct solutions, computation duration of the proposed equivalent circuit method is very short compared to traditional full-wave solvers. When we check Table 3.2 carefully, we see that n_0=10 could also be accepted as a reasonable choice, which has a computational time of only about 128 ms.

To verify the correctness of the proposed circuit model for different layouts, we simulated the given structure with an in-complete upper turn. To do this, we changed the overlap region starting from full-turn to a single turn with 60° steps (where the double layer overlap corresponds to 360° loading and a single turn corresponds to 0° loading) as depicted in Figure 3.9 and quantified in Table 3.3.

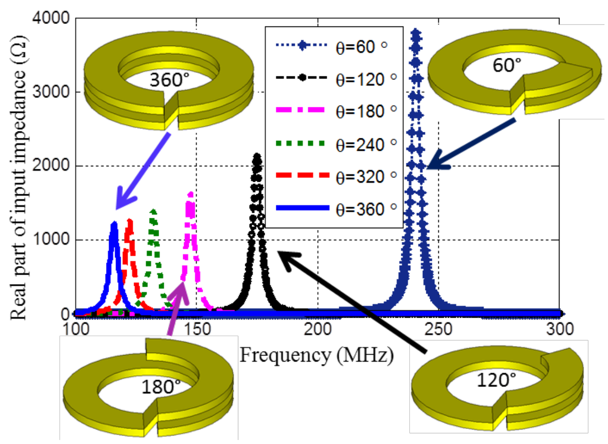

Figure 3.9: Resonance frequency characterization of the circular resonator using systematically varied overlap area.

Table 3.3: Resonance frequency characterization of the proposed architecture for different overlap areas quantified by the radial angle at the center that sees the overlap area $\theta(^\circ)$.

$\theta(^\circ)$	Resonance Frequency (MHz)
60	240.8
120	175.2
180	147.8
240	132.4
300	122.4
360	116.2

It is clearly demonstrated that the increasing the overlap region decreases the resonance frequency, which is naturally expected as a result of the circuit model discussed above. We also showed that the proposed equivalent circuit model can be used to determine the starting point for a thin-film loaded resonator. It is valid for a wide range of frequencies and it considers all of the geometrical parameters. In addition to circular elements, it can also be used for any closed geometrical shape (e.g., rectangular, square, diamond-like) due its geometry independent mathematical modeling embedded in the circuit model. In addition to circuit elements, loading of these resonators with lossy medium can also be modeled by simply changing the value of R_{eff} in the model.

3.3 Numerical Studies

The proposed resonator architecture exhibits unique properties such as extraordinary resonance frequency tuning capability, providing higher Q-factors, maintaining higher Q-factors under lossy tissue loading, and exhibiting better magnetic field amplification to electric field induction ratio (i.e., H/E ratio) for the surrounding tissue. All of these features are systematically studied in the following sections.

3.3.1 Tuning a Deep Sub-wavelength Resonator

In real life, we do not have the dielectric materials with continuous dielectric thicknesses and relative dielectric permittivity. Since we have limited dielectric thicknesses (e.g., 7.5 and 12.5 μm) and certain limited relative permittivity, we need another tuning mechanism to achieve different resonance frequencies. For traditional SRRs, although the gap width has an incremental effect, footprint area is the only remaining degree of freedom to tune the structure. Using lumped capacitors in the gap region is another method for tuning, but this comes at the cost of using extra volume and limits the potential applications especially for in-vivo applications.

For stacked and helical resonator architectures, the dielectric thickness is another parameter, which is limited by the manufacturers fabrication constraints. In addition to dielectric thickness, helical geometries have another critical parameter, which is the overlap region, to tune its resonance frequency perfectly to a predefined frequency. Modifying the intersection area of consecutive layers in a helical ring allows us to change the thin-film capacitance as well as the mutual inductance to tune a structure over a wide range of frequencies. This can be achieved after its manufacturing as well; hence, it is an attractive way of tuning because of its practicality.

To systematically analyze the effect of overlap area on the resonance frequency, we used the previously defined rectangular helical resonator with a side length of 8 mm, a gap size of 1 mm, a metallization width of 1 mm, and a metallization thickness of 10 μm. When a full-turn double-layer helical resonator is manufactured, it will have a parallel plate area of 27 mm^2. It is expected that this configuration has the lowest resonance frequency that can be achieved in the given physical dimensions. Partial removal of one of the layers will result in decreased thin-film capacitance, as well as decreased effective inductance; hence, a higher resonance frequency will be observed as shown in Figure 3.10.

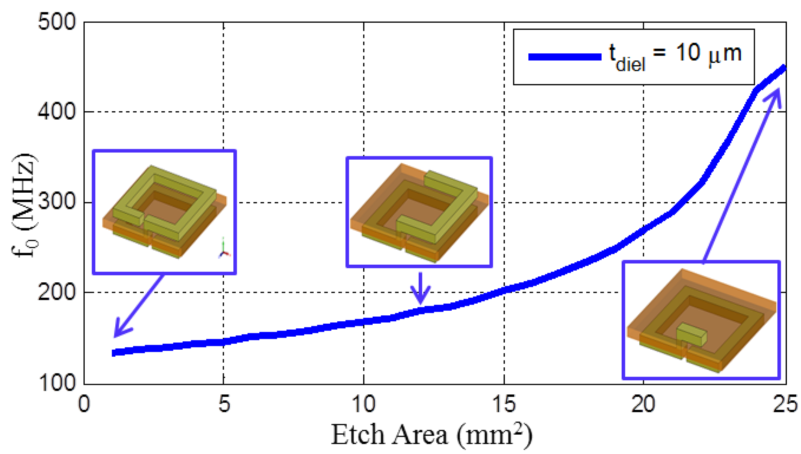

Figure 3.10: Frequency characteristics of the proposed resonator design for different overlapping thin-film regions. It is seen that resonance frequencies of about 120 to 450 MHz is achievable by partial removal of the overlay.

According to the obtained results, not only achieving a low resonance frequency but also tuning this resonance frequency precisely to a predefined value by simply etching the overlay region is possible. This opens up a wide range of applications including in-vivo ones.

To broaden our systematic study, we analyzed the resonance frequency of the provided structures for their different dielectric thicknesses . As mentioned earlier, provided design has the total thin-film capacitance area of 27 mm^2 among consecutive layers for a full turn. This time, we showed the resonance frequency as a function of percentage ratio of the etched area to the maximum thin-film area. Figure 3.11 presents the results of this systematic study.

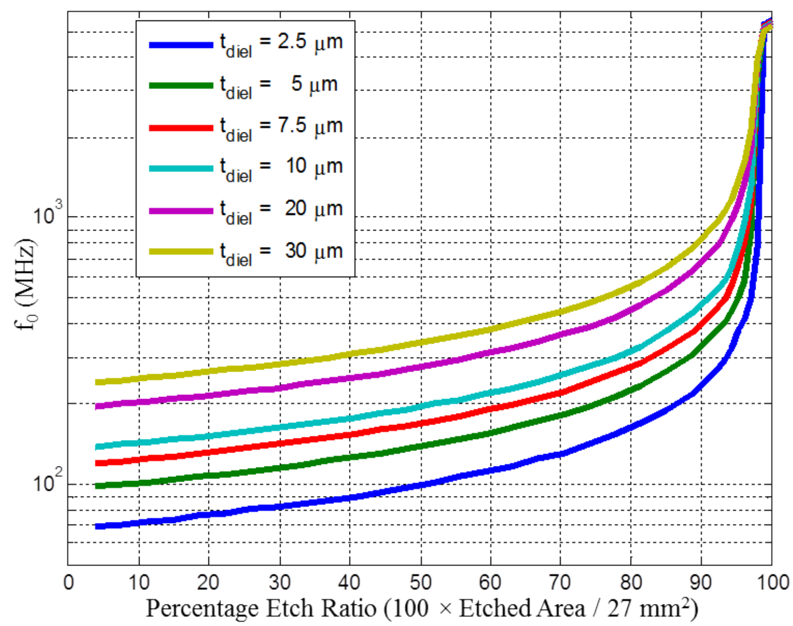

Figure 3.11: Frequency tuning property of the proposed resonator architecture for different dielectric thicknesses. It is observed that the resonance frequencies from 70 MHz to 5.5 GHz is possible using the given footprint area and varying dielectric thicknesses.

It is clearly seen that the upper limit for the resonance frequency is about 5.5 GHz, which is independent from the dielectric thickness. This is reasonable due to the diminishing effect of thin-film capacitance for a single-layer SRR (A %100 percent etch ratio corresponds to complete removal of one of the layers).

From the Figure 3.11, we can observe the effect of dielectric thickness on the resonance frequency. As the dielectric thickness becomes thinner (decreasing down to 2.5 μm in this study), thin-film capacitance becomes larger, resulting in lowered resonance frequencies for all cases. In contrast, increasing dielectric thickness (increasing to 30 μm in this study) increases the resonance frequency for all scenarios.

Additionally, there are several possible approaches to reach a predefined resonance frequency for the given results. For example, to obtain the resonance frequency of 300 MHz, one can choose a design with a 35% etch ratio and a dielectric thickness of 30 μm or a 95% etch ratio with a 2.5 μm dielectric thickness, or any solution in between these two. Practically, this property allows us to use different materials with different thicknesses to achieve the same resonance frequency. For example, if you need to have a very-thin resonator, it is better to choose the thinner dielectrics with higher percentage etch ratio. If the mechanical issues (bending, twisting or inducing strain on the resonator) force us to use the thicker dielectrics, then we can choose to use the 30 μm scenario with lower etch ratio.

3.3.2 Q-factor Analyses

Q-factor is one of the key performance indicators of a resonator. The higher the Q-factor is, the better it is to accomplish its purpose. As previously defined, Q-factor of a structure can be increased by increasing its energy storage capability and decreasing losses due to finite conductivity of metallization and non-zero resistivity of surrounding medium.

To systematically analyze the Q-factor of the proposed resonator design, we started with an arbitrary resonance frequency of 250 MHz, which can be achieved by using the dielectric thicknesses given in the previous section. We tuned the given resonator architecture to this resonance frequency for different dielectric thicknesses. Q-factor of the overall system is calculated by using Equation (3.14):

$$Quality\ Factor = 2\pi\ \frac{Energy\ Stored\ in\ the\ Simulation\ Domain}{Total\ Power\ Dissipiated\ in\ One\ Period} \tag{3.14}$$

Here the Power Density and Energy Density monitors with the Time Domain Solver of the CST Microwave Studio are used for necessary calculations. The geometrical parameters are reported in Table 3.4 to achieve the same frequency. Figure 3.12 depicts the parameters provided in Table 3.4.

These two graphs given in Figure 3.12 are exactly the same and acquired from Table 3.4. Here, we see that the Q-factor of the given resonator is increasing due to increased overlay region and also due to the thickness of the dielectric region.

Table 3.4: Q-factors of different designs for an arbitrary resonance frequency of 250 MHz.

Dielectric Thickness (μm)	Ovrelaid Area (mm^2)	Q-factor
2.5	2.4	107
5	4.3	155
7.5	6	180
10	7.8	191
20	15	209
30	22	217

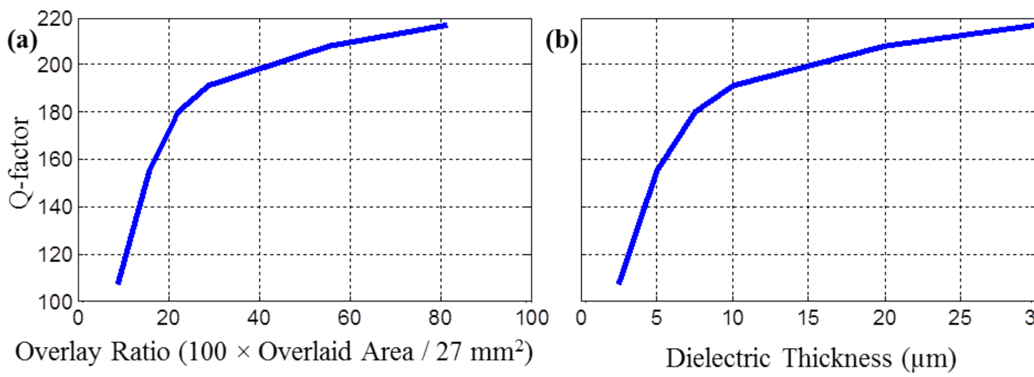

Figure 3.12: Q-factors of different designs for an arbitrary resonance frequency of 250 MHz. (a) Q-factor increases due to increased overlay region. (b) Q-factor increases due to increased dielectric thickness.

As previously explained, increasing overlay region, in other words the turn ratio, increases the effective inductance given the footprint area and results in the increased Q-factor [55]. Similarly, increasing dielectric thickness also decreases the capacitance value per unit length, which requires increased inductance to sustain the predetermined resonance frequency. Thus, the Q-factor of the resonator increases proportional to the overlay area. Additionally, we observed that the Q-factor seems to asymptotically converge to a value, which we should interpret using physical explanations.

This issue was previously reported for the conventional structures that their Q-factor does not increase linearly with their turn ratio due to decreased inductive coupling between different turns [39]. Although this limitation is not valid for our design, Figure 3.12 misleads us to draw the correct conclusion (whereas cascaded equivalent circuit model dictates linear relationship between the Q-factor and the number of turns). The main reason for these results is the improper choice of calculation domain. In literature, as well as in our method, simulation domain is filled with free space that is lossless. For thinner dielectric regions, total loss is small compared to thicker dielectrics. Hence, although it is not fair, the overall dissipated power increases due to increased dielectric thickness. This seems a limitation and causes saturation in the Q-factor calculations.

As an ultimate example, let us fill a large simulation domain using a lossy dielectric (with a loss-tangent of δ) that contains a small resonator and a plane wave excitation for the calculation. The plane wave solution in this medium (with negligible resonator effect) will have an effective Q-factor of about $1/tan(\delta)$. For our case, polyimide film used in the simulations has a loss tangent of 0.003, which results in the Q-factor of about 330.

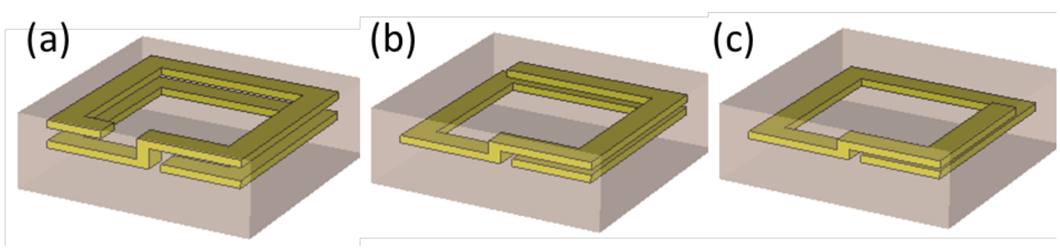

Figure 3.13: Schematics of the calculation domain at the resonance frequency of 250 MHz for different design parameters (not drawn to scale). (a) A thin-film region thickness of 30 μm with a 95% of overlay area, (b) a thin-film region thickness of 20 μm with a 63% of overlay area, and (c) a thin-film region thickness of 10 μm with a 33% of overlay area.

To make a fair comparison among different design parameters we determined a constant volume (a volume that contains the whole resonator) for energy storage and power dissipation calculations. To do this, we set a region with a thickness of 100 μm to include the whole design and limited our calculation medium to this volume (including the dielectric and resistive losses) to eliminate the contribution of enlarging dielectrics. The overall structures are sketched in Figure 3.13. By considering field distributions only in the given dielectric volume, we obtained the curves for Q-factors as reported in Figure 3.14.

Here we see that the overall Q-factor is decreased from about 200 to 20 for 10 μm thin-film layer thickness. This is absolutely in agreement with the expected

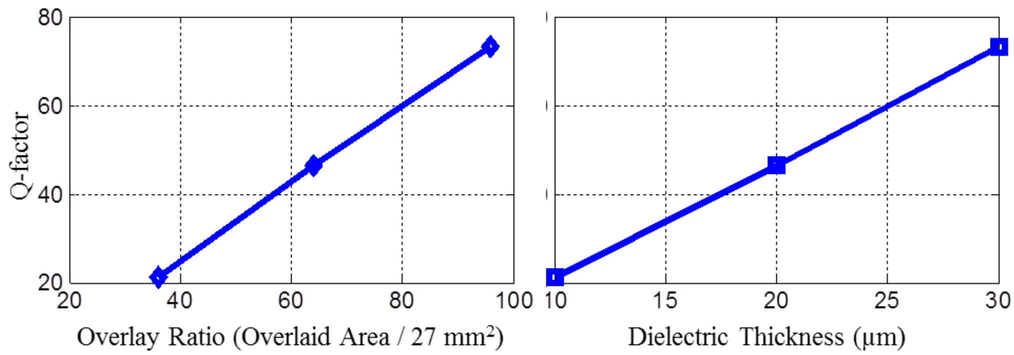

Figure 3.14: Q-factors of different designs for an arbitrary resonance frequency of 250 MHz. (a) Q-factor increases linearly due to the increased overlay area and (b) Q-factor increases linearly due to the increased thin-film region thickness. The overall dielectric region has a constant thickness of 100 μm.

results. Enlarging the lossy dielectric volume 10 times decreases the calculated Q-factor 10 times due to increased losses introduced into the medium. Although the resonators are the same (with the same geometric parameters immersed into the dielectric), Q-factors are completely different due to the dominant effects of the surrounding medium. Hence, the second model (the model with a constant dielectric volume) estimates the effect of each parameter on Q-factor more certainly.

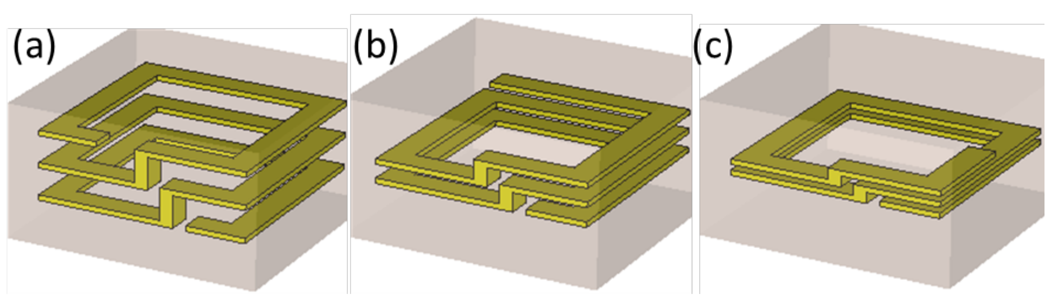

Figure 3.15: Schematic of the calculation domain for a 3-layer resonator at a resonance frequency of 250 MHz for different design parameters (not drawn to scale). (a) A thin-film region thickness of 70 μm with a 95% of overlay area, (b) a thin-film region thickness of 50 μm with a 65% of overlay area and, (c) a thin-film region thickness of 30 μm with a 19% of overlay area.

To further verify the numerical calculation methods with previously explained models (e.g., cascaded circuit equivalent model), we added a third layer to the overall structure as depicted in Figure 3.15. To ensure the immersion of resonator into the given dielectric, we changed its thickness from 100 to 250 μm. We again tuned the above structure to an arbitrary frequency of 250 MHz for all scenarios to eliminate the effect of resonance frequency on the Q-factor calculation. From Figure 3.16, it is observed that the Q-factor of the proposed resonator increases almost linearly for the given turn number with a similar slope for each turn. This allows us to draw a conclusion of increasing Q-factor with an increasing turn ratio (Q $\propto n$) due to the increase in mutual inductance among different layers.

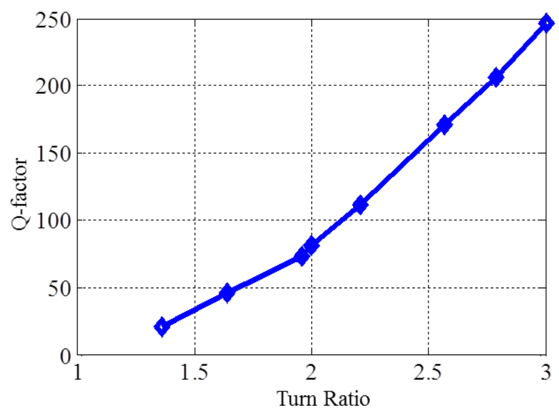

Figure 3.16: Q-factors of different designs for an arbitrary resonance frequency. Q-factor increases linearly due to increased turn ratio as expected from cascaded-equivalent-circuit models.

In conclusion, we successfully modeled the proposed resonator architecture using full-wave numerical solutions to estimate its Q-factor. The trends found in these numerical studies are in agreement with our previously reported cascaded-equivalent-circuit models.

3.3.3 Loading Effect

Designing a conventional resonator for a free-space application is straightforward and several methods can be used for it. However, using a resonator in living tissues requires special features including maintaining the Q-factor and low electric field deposition in the surrounding medium. All of these parameters are more or less related to each other and the physical interpretation to this can be given usgin the notion of electric field confinement. Although the free-space Q-factor of a resonator can be increased by using conventional methods, maintaining high Q-factors in a lossy environment requires novel designs. The most important factor affecting the Q-factor is the electrical losses caused by the resonators. For a given inductance, which determines the stored inductive energy, a design with a strong electric field confinement outside the resonator volume will be more vulnerable to loading [56].

Electric field distribution of conventional structures (including SRRs, spirals etc.) protrudes from their plane that makes them prone to loading. The proposed double-layer thin-film geometry has the advantage of electric field confinement in the low-loss dielectric region that allows for higher Q-factor and lower resonance frequency shifting. To analyze the superiority of the proposed architecture, we numerically evaluated its electric field confinement property. Figure 3.17 depicts the normalized electric field distribution at the resonance frequency of the architecture.

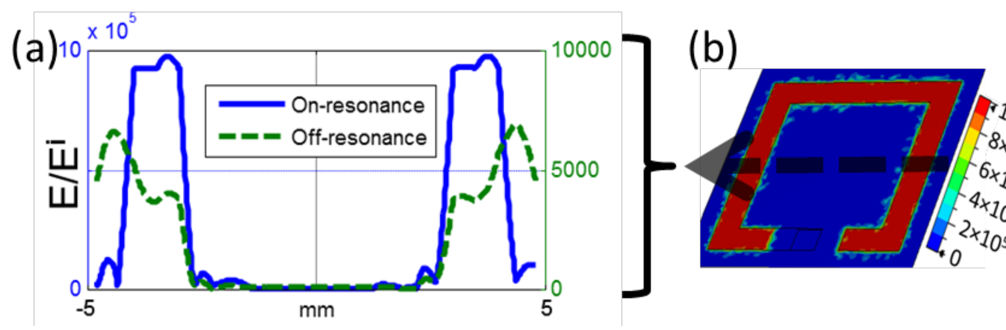

Figure 3.17: Electric field confinement property of the proposed resonator architecture. (a) Amplitude of the electric field normalized to incident field along with the dashed line marked in (b) shows that the electric field is 6 orders of magnitude higher in the localized region on resonance with respect to the incident field.

Figure 3.17(a) presents the normalized electric field profile along with the dashed line marked in Figure 3.17(b). Here, it is observed that the electric field is 6 orders of magnitude higher in the dielectric region compared to the incident field and about 3 orders of magnitude higher compared to off-resonance case. From Figure 3.17(b), it is clearly observed that the electric field distribution is strongly localized in the dielectric region between the top and bottom metallic layers, which is essential to achieving high Q-factor even when loaded with a lossy medium including biological tissues.

The proposed resonator structure exhibits unique properties for wireless operation that are critical to in-vivo studies. Conventional designs, e.g., single and stacked SRR without a cross-via metallization, have lowered electric field confinement and isolation in the insulator region. On the other hand, the proposed device properly confines the electric field inside its dielectric material between its metallic layers to increase the energy storage volume. Thus, this allows us to store more energy resulting in the increased Q-factor. Additionally, living tissues exhibit higher conductive losses, e.g., conductivity of 1 S/m, whereas the dielectric losses are radically lower, e.g., conductivity of 10^{-16} S/m for Kapton. Hence, confining electric field inside the dielectric substrate, instead of living tissues, drastically decreases the dissipated resistive power at the given frequency when this structure is placed in a lossy media. Thus, this helps to keep up the Q-factor of the proposed resonator significantly higher also when loaded in-vivo.

To make a comparison with a conventional SRR geometry, we numerically calculated the electric field distribution of the both structures along with the dielectric region used for metal deposition. Figure 3.18 depicts the comparison between the proposed structure (a) and the conventional SRR (b) for the same resonance frequency. The given SRR is loaded with a lumped capacitor of 30 pF from its gap region to achieve this resonance frequency, whereas the proposed architecture is self-resonant for the previously given layout parameters.

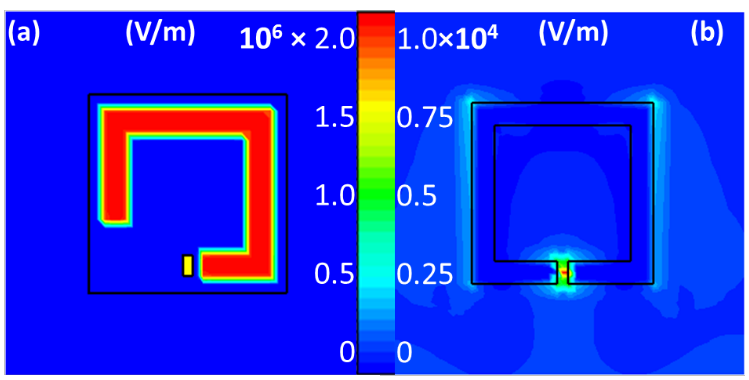

Figure 3.18: Electric field confinement comparison of the proposed architecture (a) and the conventional SRR (b). Conventional SRR is loaded with a capacitor of 30 pF to achieve the same resonance frequency. Electric field confinement of the proposed structure is more than two orders-of -magnitude ($2 \times 10^6/10^4$) higher than the conventional SRRs.

Here, it is seen that the electric field distribution of the proposed structure reaches about 2×10^6 V/m (with the exact value calculated as 2.13×10^6 V/m) where the conventional SRR has only the electric field value of about 10^4 V/m (with the exact value calculated as 10,970 V/m). Here, over two-orders-of-magnitude difference in electric field confinement is observed, which is a strong indicator of high Q-factor under lossy medium loading.

In addition to the electric field confinement property of the proposed structure outperforming the conventional SRRs, it is also not to spill its confined electric field over the surrounding medium. Figure 3.19 is provided to depict this property qualitatively. The proposed structure (Figure 3.19(a)) does not spill over its electric field into the medium, whereas the conventional SRR (Figure 3.19 (b)) has a wider electric field distribution across the outer plane. This is maximized in its gap region due to convection currents of the gap capacitor, which is expected to cause more interaction between the resonator and the surrounding medium.

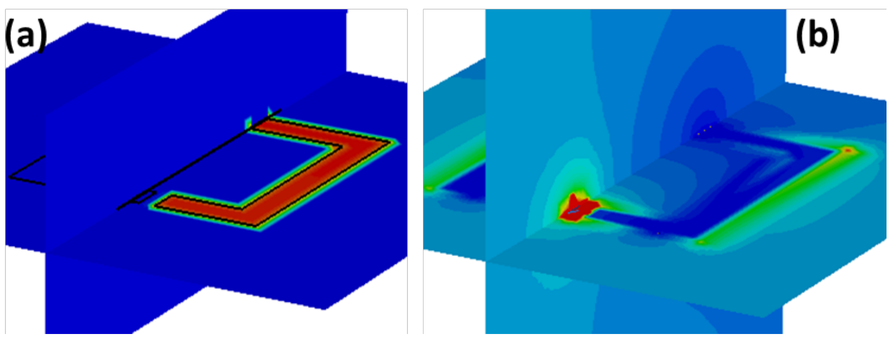

Figure 3.19: Electric field spill-over comparison between the proposed architecture (a) and the conventional SRR (b).

This is also quantified in Figure 3.20 that the proposed structure strongly confines its electric field in the dielectric region (almost two orders of magnitude better confinement in e-field distribution) without causing any magnetic field degradation (left). Magnetic field distribution of a conventional resonator along with a fictitious curve passing through its geometric center is depicted by a blue dashed curve and the magnetic field distribution of the proposed architecture along with a fictitious curve passing through its geometric center is depicted by a green dotted curve (both in plots and schematic (Figure 3.20-Left). It is seen that the magnetic field distributions are similar. Similarly, Electric field distribution of a conventional resonator along with a fictitious curve passing through its split region is depicted by a blue dashed curve and the electric field distribution of the proposed architecture along with fictitious curves passing through its metal traces

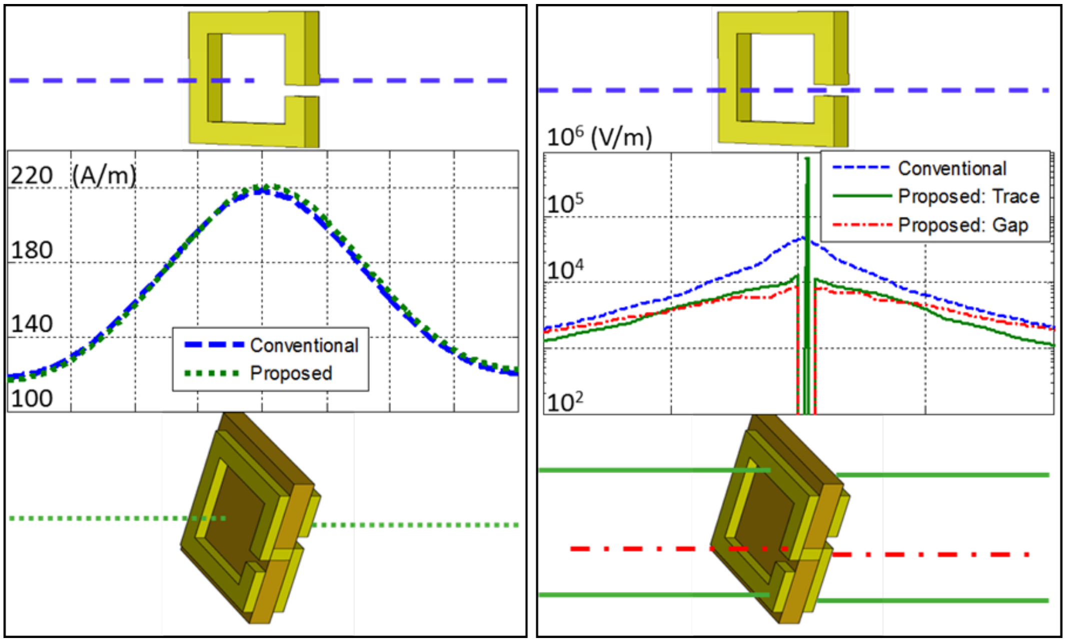

Figure 3.20: Magnetic field (left) and Electric Field (Right) distribution of the conventional (blue curves in plots) and proposed architecture (green and red curves) shows that the e-field of the proposed architecture is strongly confined in the dielectric region, without degrading magnetic field distribution.

and gap region is depicted by a green and red dashed-dotted curves respectively (both in plots and schematic (Figure 3.20-Right).

Here, we observed that the proposed structure has the better electric field confinement in its dielectric region, resulting in better isolation from the environment. Thus, better loading performance compared to conventional geometries is expected. We can see that the E-field distribution of the proposed structure never exceeds the level of 10^4 V/m, where a conventional resonator requires an isolation layer least 1.5 mm in thickness in both directions, which prevents its usage for in-vivo.

3.3.4 E- and H-Field Distributions

Electric field confinement of a resonator shows its energy storage capability and isolation of this region from the environment implies a better protected performance under loading in terms of resistive losses (hence, leading to higher Q-factors) for the given structure. Although E-field isolation can be achieved by using non-conducting coatings, magnetic field distribution of the resonator comes into the picture especially for MRI applications. Not only confining electric field, but also the amplification of magnetic field in the vicinity of a structure is critical to make it useful for MRI applications such as marking [46].

Figure 3.21 depicts the electric field and magnetic field distributions of the proposed resonator structure with the previously defined geometric parameters. Here, it is seen that the electric field distribution of the proposed structure maximizes at about 2×10^6 V/m (while the exact value is calculated as 2.13×10^6 V/m) and the magnetic field, at about 1.5×10^3 V/m (while the exact value is calculated as 1,497 A/m). The best point for these two field distributions is the location of their maxima. The maximum of the electric field is located in the dielectric thin film, which is important to isolate the structure from loading effect of the environment and also isolating the environment from the heating effect of the structure. Similarly, the maximum of the magnetic field is located outside this dielectric thin-film that is important for magnetic resonance imaging.

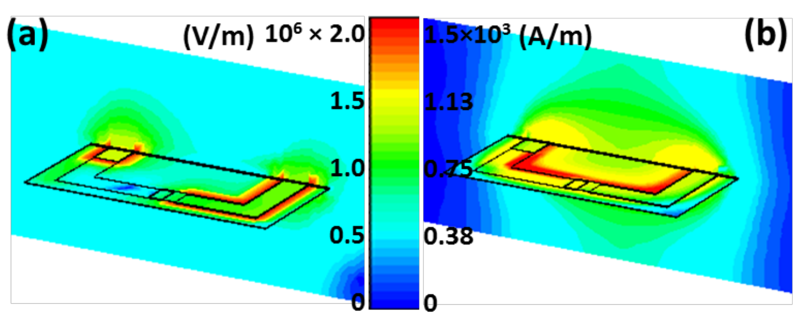

Figure 3.21: Field Distributions: Electric field (a), and magnetic field (b) distribution of the proposed architecture.

To visualize the superiority of the proposed resonator in terms of the electric fields for better understanding and quantify the relationship, we calculated the ratio of magnetic field to electric field values on the same plane as depicted in

Figure 3.21. The resulting numerical calculations are presented in Figure 3.22 for the resonant case (a) and non-resonant cases (b). Here we observed that the ratio of magnetic field to electric field is much higher in the resonant mode as expected and with higher values located in the vicinity of the resonator (not inside the dielectric region).

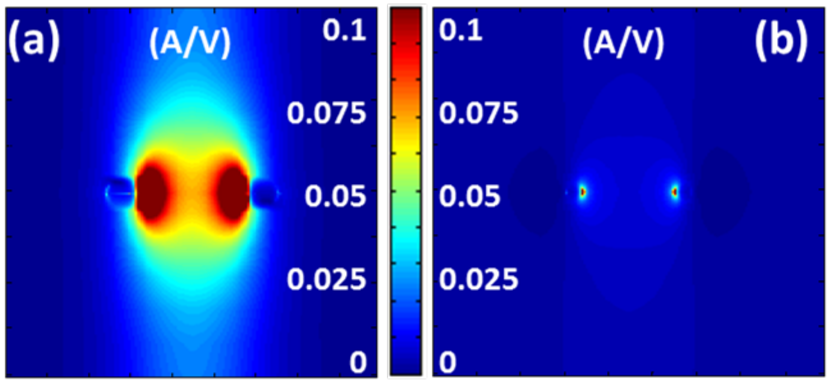

Figure 3.22: Magnetic field to electric field ratio (A/V) of the structure for: resonant (a), and non-resonant (b), modes.

To explain this phenomenon more clearly, we located a lossy tissue on the top and bottom of the resonator. This loading scheme is expected to degrade the performance of the resonator. We also repeated the same scenario with a conventional SRR tuned with a lumped capacitor. The results of this study are shown in Figure 3.23 for the proposed architecture (a) and the conventional SRR (b).

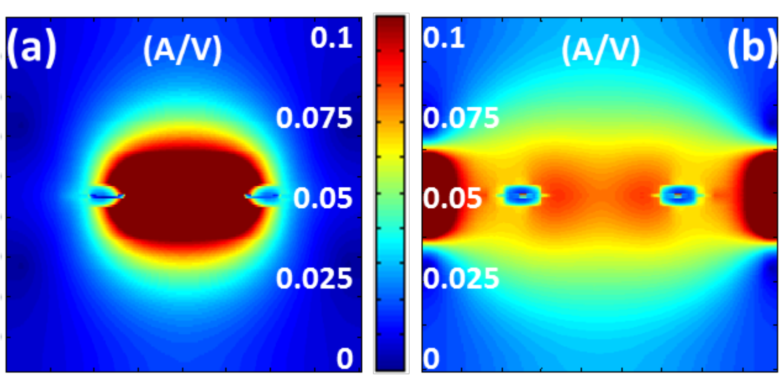

Figure 3.23: Magnetic field to electric field ratio (A/V) of the proposed structure (a) and the conventional SRR tuned with a lumped capacitor (b) in a lossy medium for the resonant mode of operation.

Here, it is seen that the loading of the proposed architecture does not degrade its performance unlike in the conventional SRR and its H/E distribution ratio is more suitable for MRI applications. From these results, different than conventional structures (including SRRs), we can foresee that the proposed architecture should be operating with little degradation of performance for the in-vivo applications. For example, its Q-factor performance is expected not to degrade significantly due to loading with a lossy tissue. Additionally, since the electric field is confined inside the dielectric region, in the case of using the proposed resonator, we expect comparably lower temperature increases and specific absorption rates (SAR) for the surrounding medium (compared to conventional resonators architectures).

3.4 Microfabrication

Although different microfabrication methods for micro-ring resonators have been proposed previously [57], the fabrication methodology of the proposed resonator architecture here is carefully designed for high yields for mass production and lower treatment with chemicals to preserve biocompatibility. A process flow for microfabrication methodology on a rigid silicon substrate is illustrated in Figure 3.24.

A positive photoresist (AZ 5214, AZ-Microchemicals) was spin coated onto a Si substrate, followed by ultraviolet (UV) lithography to create features for the bottom layer of the resonator. A thermal evaporation method was used to deposit the titanium/gold (Ti/Au) metals and lift-off was applied by using acetone with 1 minute of immersion. At the end of these processes, we obtained conventional SRR geometry fabricated on a Si substrate with the previously given footprint area.

To make the capacitive regions, we deposited the silicon-nitride (Si_3N_4) onto the whole substrate by using plasma-enhanced chemical vapor deposition (PECVD) method. The dielectric was then chemically etched to construct the cross-via metallization by using diluted hydrofluoric acid (HF) solution (about 1% of HF solution).

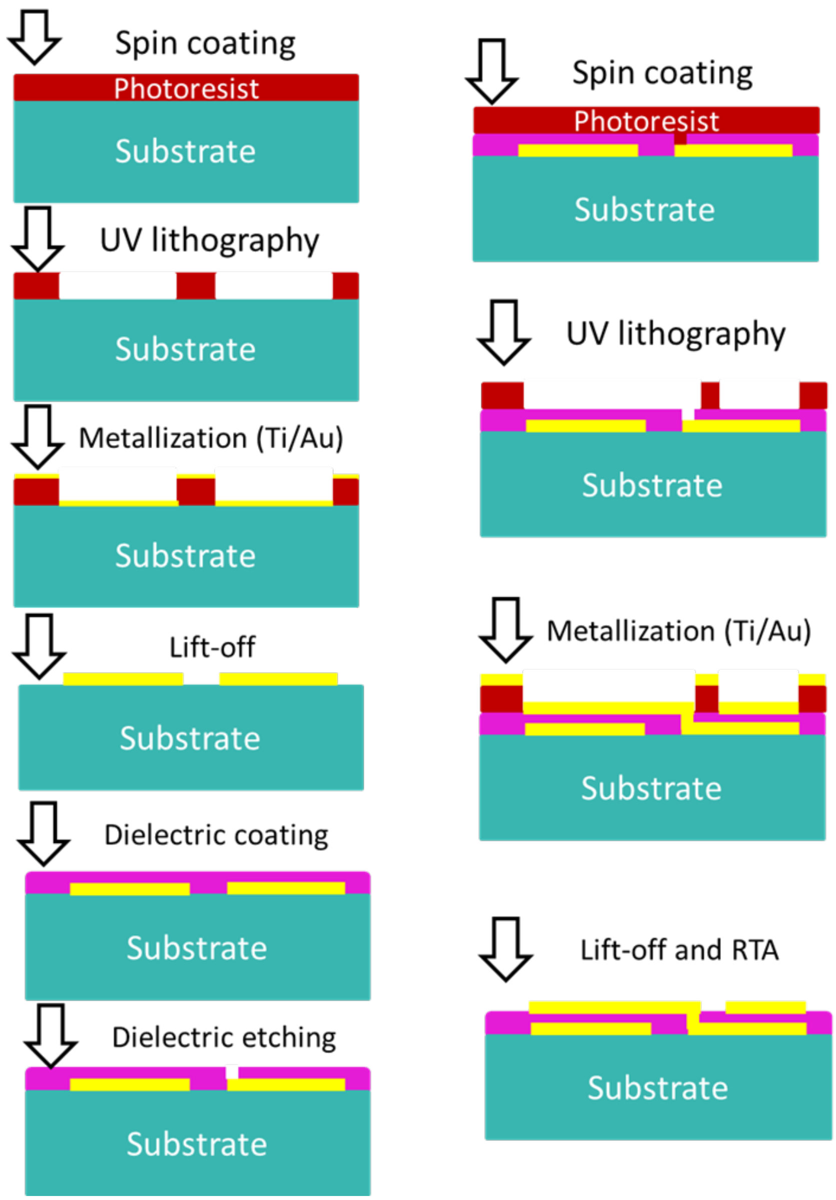

Figure 3.24: Schematic illustration for the microfabrication of the proposed resonator architecture onto a rigid silicon substrate by using conventional methods.

Subsequent fabrication of the second layer was almost the same as the first one, with proper alignment. Here, the alignment accuracy determines the precision of targeting a resonance frequency and potential mismatches between the numerical calculations and the experimental results will stem from this second layer deposition. After the fabrication of the second layer, Si wafer was rinsed and dried followed by a 5 min rapid thermal annealing at 250 °C.

Although the proposed microfabrication methodology may be suitable for mass production, it is not preferred due to potential biocompatibility issues. Using photoresist for in-vivo device fabrication might render dangerous as the remnants of the HF could be fatal for in-vivo applications.

Using UV photolithography allows us to create features as small as 1 μm with almost the same alignment accuracy. This level of accuracy is very critical to fabricate a device with predetermined parameters especially for the structures without a tuning capability. However, the proposed resonator design is capable of wide range of resonance frequency tuning. Thus, we can use relatively rough methods to fabricate the metallization layers and cross-via connection that would make the fabrication more cost effective and biocompatible.

Here, a new process flow to fabricate the proposed structure is designed by using hard masks (also known as shadow masks) with complementary SRR shapes. Using a hard mask prevents us to achieve a μm-level precision, which is not a limitation for our structure, but simplifies the fabrication steps significantly. The new microfabrication methodology to create the proposed architecture is illustrated in Figure 3.25.

A shadow mask with asymmetric comb sized SRR shapes was manually placed on top of a substrate to allow for Ti/Au vapor to penetrate through the open regions and create SRR shapes. By this method, the usage of UV illumination can be omitted at a cost of lowered fabrication accuracy. Dielectric coating and etching were than undertaken by using the same PECVD methodology as described earlier. The second layer and the cross-via metallization were coated by using the same hard mask with complementary side to allow for the creation of the helical geometry.

This simplified proces flow does not include any photoresist coating and UV

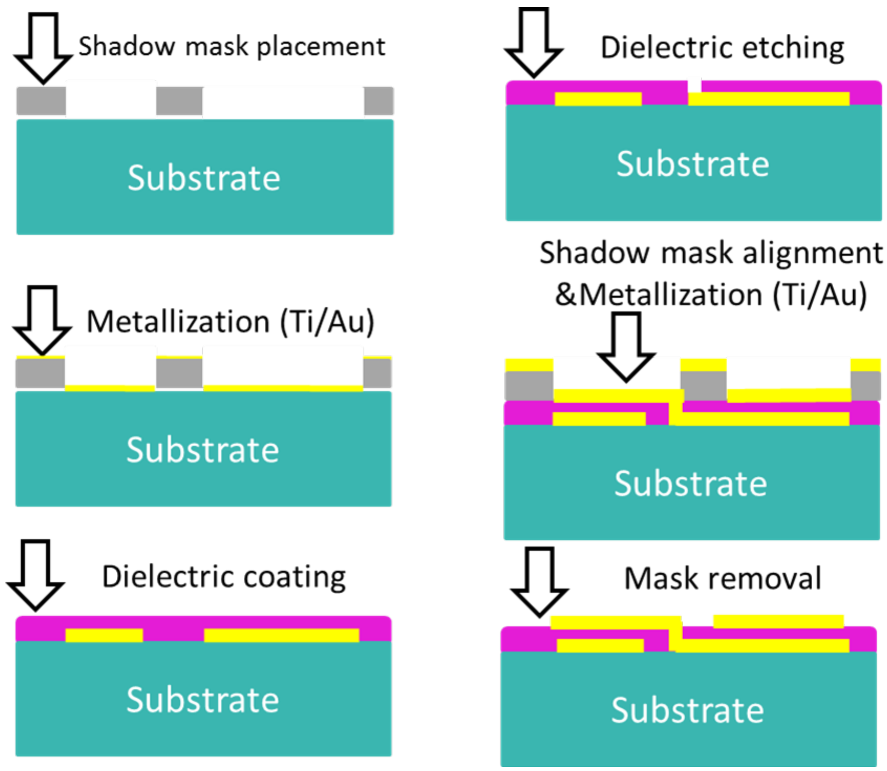

Figure 3.25: Schematic illustration for the microfabrication of the proposed resonator architecture onto a rigid silicon substrate by using simplified methods.

lithography methods, which makes it potentially safer compared to conventional techniques. Additionally, decreasing the number of steps allows us to increase the fabrication yield, which makes this process flow more promising for practical applications. Figure 3.26 shows the optical photography of the microfabricated samples with different footprint areas onto a rigid substrate by using the simplified approach.

Fabrication of the proposed helical architecture onto a flexible substrate can also be achieved by using the same process flow as described above. This time, one should be more careful to handle the overall sheet of flexible substrate and alignment of the hard mask will be more difficult. Hence, this alignment problem will lead to large discrepancies for the resonance frequency between the numerical solutions and the experimental results. Similarly, replacing a rigid substrate with a flexible one, one ends up having two layers of dielectric (one is for the substrate and the other one for the dielectric region) and in principle one of these could serve the purpose of the other. Hence, at this point our idea was to use a substrate

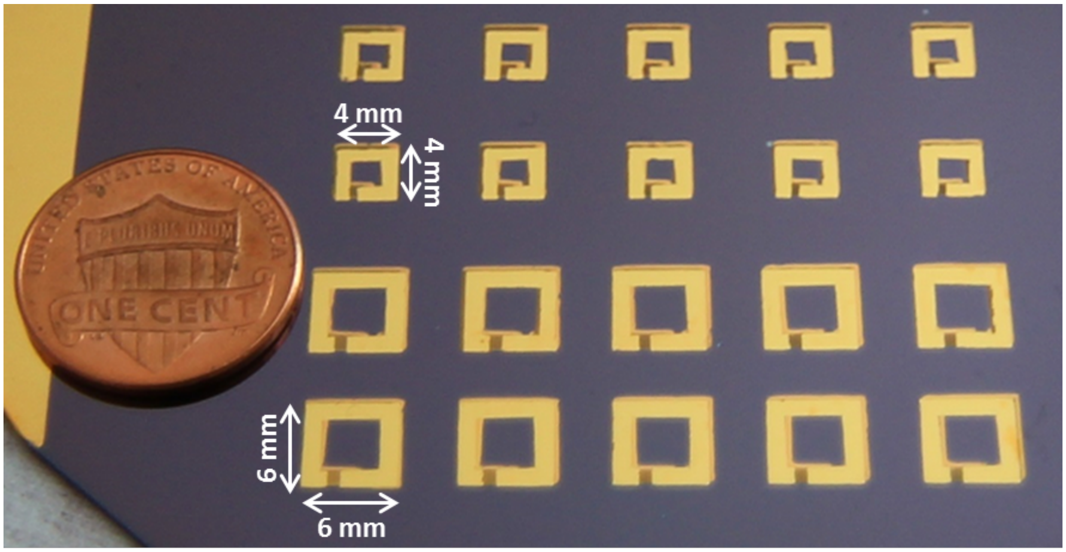

Figure 3.26: Optical photograph of the microfabricated samples on rigid substrate by using simplified methods. The ease of fabrication comes at the cost of misalignment that would result in increased resonance frequency discrepancies between the numerical and experimental results.

as a dielectric region and to make an ultra-thin helical structure.

Using a flexible substrate, which also serves as a dielectric region, eliminates the nitride deposition step and further simplifies the microfabrication methodology to increase yield and biocompatibility. The process flow to create helical structures using both sides of a polyimide film is illustrated in Figure 3.27.

Here, a shadow mask including complementary SRR shapes with asymmetric comb sizes was used to deposit a layer of patterns on one side of the polyimide tape. Then, the tape was turned upside down to coat the second layer and cross-via metallization. Unlike the conventional HF-based etching of silicon nitride, the polyimide was etched by using mechanical drilling. The second layer of metallization was deposited by using the same hard mask. In the end, the polyimide substrate was sandwiched between two metallization layers so that it was used as a capacitive region between the metal levels. This decreases the device thickness significantly, leading to ultra-thin and flexible self-resonant device [47]. The optical photographs of the fabricated samples are provided in Figure 3.28 for the side lengths of 14 mm (a) and 8 mm (b).

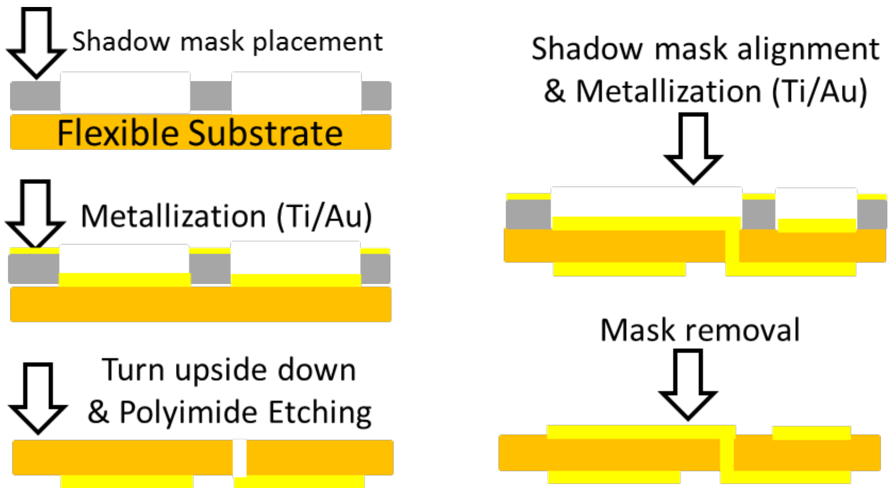

Figure 3.27: Schematic representation for the microfabrication of the proposed architecture onto a flexible substrate by using simplified methods.

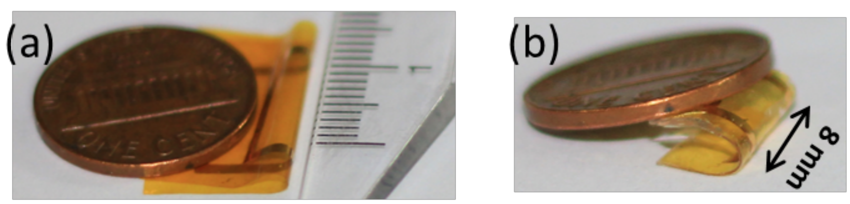

Figure 3.28: Optical photographs of the microfabricated samples on flexible polyimide thin-films by using simplified methods for (a) 14 mm and (b) 8 mm side lengths.

3.5 RF Characterization

Characterization of a wireless circuit component is different than its wired counterparts. Measuring scattering parameters (S_{11}, S_{21}, etc.) clearly defines the operation of wired circuit elements such as waveguides, transmission lines, inductors, and resonators. However, characterization of a wireless structure requires designing specific measurements and modeling techniques to determine its characteristic parameters.

As described in Section 3.2, our proposed thin-film loaded helical structure can be modeled by its cascaded equivalent circuit to determine its characteristic parameters including the resonance frequency and the Q-factor. For numerical environments, determining a measurement result without touching or changing it, is possible. However, in practice, measuring the conduction current of a wireless resonator is not possible without affecting its operation. Thus, the characterization of a wireless resonator needs a proper measurement method along with a model to determine the necessary parameters from the measured ones.

A quick and effective method to find the resonance frequency of a wireless loop coils was previously reported [58]. This approach relies on using a pick-up coil antenna to excite and measure the response of a wireless resonator. For low frequency operation, the pick-up coil antenna can be modeled by using an effective resistance (R_{ant}) and an effective inductance (L_{ant}). Here, R_{ant} includes the resistive losses that the antenna interacts and the radiation impedance of the coil for the operation frequencies. To excite and measure the response of a wireless resonator, it is required to have an inductive coupling between the pick-up antenna and the resonator. As explained in Section 3.2, the proposed structure itself can be modeled by its effective circuit parameters, L_{res}, C_{res} and R_{res}. The overall circuit model to explain the measurement system together looks like in Figure 3.29.

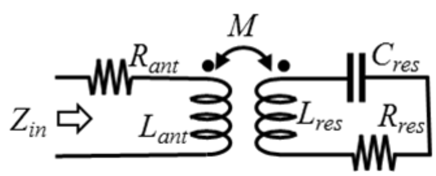

Figure 3.29: Equivalent circuit model to characterize a wireless resonator. The pick-up coil antenna is inductively (M) coupled to the wireless resonator and the input impedance, Z_{in} seen through the antenna is measured by using a network analyzer.

The main parameter that is measured by using the antenna is its input impedance. From the circuit theory, the measured input impedance can be easily found as given in Equation (3.15):

$$Z_{in} = R_{ant} + jwL_{ant} + \frac{M^2\ w^2}{R_{res} + jwL_{res} + \frac{1}{jwC_{res}}} \tag{3.15}$$

where w is the angular frequency and $j = \sqrt{-1}$. A free space input impedance measurement without a resonator was recorded to find the characteristic parameters of the antenna itself. This data was algebraically subtracted from the input impedance measurements that were acquired with a mutual coupling to the resonator to find the effective input impedance of the resonator (Z_{eff}). Z_{eff} can then be formulated as given in Equation (3.16):

$$Z_{eff} = \frac{M^2\ w^2}{R_{res} + jwL_{res} + \frac{1}{jwC_{res}}} \tag{3.16}$$

Having a higher Q-factor ensures the higher input impedance for the real part of Z_{eff} at the resonance frequency. Similarly, the imaginary part of Z_{eff} is expected to be zero at the resonance frequency. However, S_{11} might not have a dip at the resonance frequency. Hence, tracking the zero crossing for the imaginary part of Z_{eff} is the most reliable method to determine the resonance frequency.

Similarly, measuring the dip of S_{11} does not give a reliable result to estimate the value of Q-factor. Higher Q-factors may result in lowered dips or vice-versa. Hence, instead of using the curve of S_{11}, we chose to use the complex impedance values to fit the best curve using equivalent circuit model to estimate its Q-factor from the effective parameters of R_{eff}, L_{eff} and C_{eff} based on the formula (3.2).

Figure 3.30 shows the characteristic curves seen through the pick-up antenna for a resonator with a L_{eff} of 20 nH, a C_{eff} of 100 pF, a M of 20 nH and R_{eff} ranging from 1 to 10 Ω. These parameters result in a resonance frequency of about 112.54 MHz with a Q-factor ranging from 14 to 1.4. This figure proves the arguments above that the Q-factor of a wireless resonator cannot be deduced from the tracking of S_{11} measurement. This task requires proper modeling of mutual coupling and resonator.

Numerical studies reported in Section 3.3 indicate that a resonance frequency of about 100 MHz is achievable for the footprint area of 8 mm × 8 mm with a dielectric thickness of about 10 μm. To achieve the given resonance frequency with standard polyimide thin-films (e.g., Kapton HN30 has a thickness of 7.5 μm and Kapton HN50 has a thickness of 12.5 μm), we microfabricated the devices with 14 mm × 14 mm footprint area by using HN50 polyimide thin-film. Resulting Z_{eff} curves are given in Figure 3.31 for their real parts in (a) and imaginary parts in (b) separately.

It is clearly seen that the eight samples (out of nine) were microfabricated successfully to resonate below 100 MHz, while six of them (Samples 2, 3, 4, 7, 8, and 9) had almost the same characteristic parameters and two of them (Samples 1

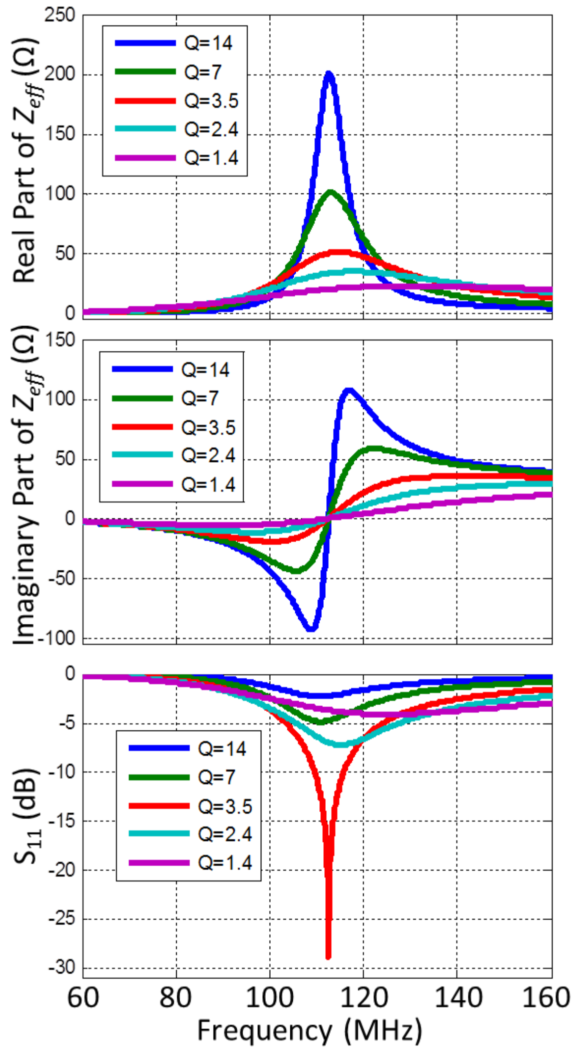

Figure 3.30: Wireless resonator characterization: (a) Real part and (b) imaginary part of the effective impedance and (c) the scattering parameters (S_{11}) seen through the pick-up coil. Note that having a higher Q-factor does not guarantee to have a sharper S_{11} dip, which is conventionally true for wired measurements.

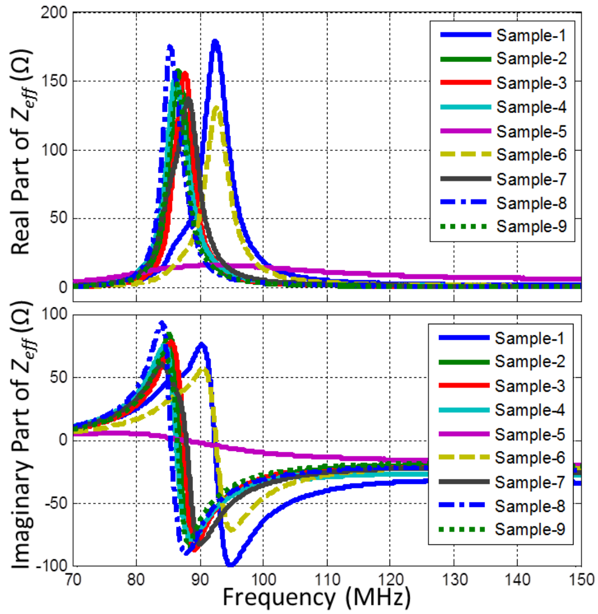

Figure 3.31: Experimental characterization of the fabricated samples over a 14 mm × 14 mm footprint area using a polyimide thin-film with a thickness of 12.5 μm. Eight samples (out of nine) are working and six of them almost have the same characteristics (Samples 2, 3, 4, 7, 8, and 9) and two of them (Samples 1 and 5) have slightly different characteristics due to fabrication imperfections.

and 5) have slightly different characteristics possibly due to the fabrication imperfections. Q-factors of all samples were calculated, first by finding their effective parameters and then using the Q-factor formulation provided in Equation (3.2). We calculated that the Q-factors are ranging between 75 and 68, which deviates mainly due to the metallization thickness variation among different samples.

To observe the first experimental tuning of the proposed resonator architectures, all of the working samples were tuned to about the imaging frequency of a 3 T MRI scanner by partially removing one of their metallization layers. The resulting characteristic curves are shown in Figure 3.32 for the real part (a) and the imaginary part (b) separately.

The second layer of these 14 mm × 14 mm samples were etched approximately by 15 mm^2, which corresponds to a 29% of etch ratio (as the overall surface area is about 51 mm^2). All of these tuned samples were also thermally annealed for better electrical conductivity. After successfully fabricating and tuning these devices with the footprint of 14 mm × 14 mm and using 12.5 μm polyimide tapes,

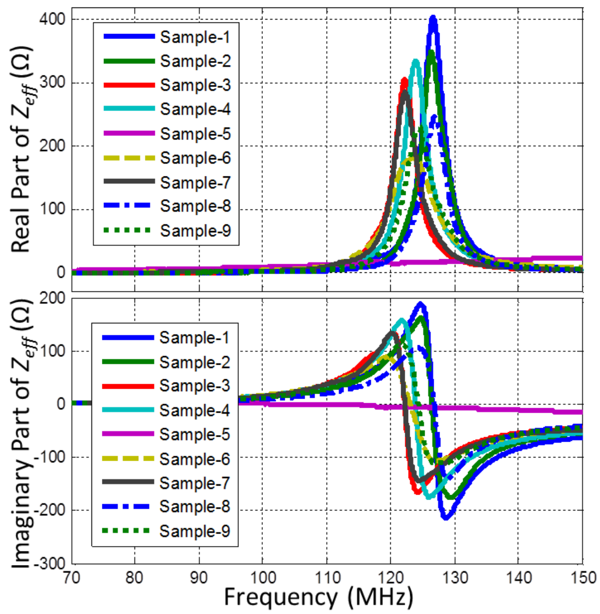

Figure 3.32: Experimental tuning results of the fabricated samples given in Figure 3.30. All of the working samples were successfully tuned to about the imaging frequency of a 3 T MRI scanner.

we further designed sub-cm resonators to be used for in-vivo applications.

As a starting point, we used the same tape material to see the resonance frequency and compare them with our numerical results in Section 3.3. Hence, here we used a polyimide film with a thickness of 12.5 μm and observed the resonance frequency characteristics presented in Figure 3.33.

In Figure 3.33, we experimentally showed that the proposed devices possess resonance frequencies of about 130 MHz. These results are in agreement with the ones given in Section 3.3, which is about 140 MHz. Similar to the 14 mm $\times$ 14 mm case, here all of the fabricated samples were working with reasonable resonance qualities. However, three of these samples had characteristics that are different from the rest of the samples. This is attributed to the geometrical misalignments, which occurred during microfabrication. For the smaller sizes, the alignment of the second layer on top of the first one becomes more important to obtain experimental results in agreement with the numerical ones.

Although the fabricated structures exhibited sufficient Q-factors (e.g., about 35 for free space), they do not have suitable resonance frequencies and need to

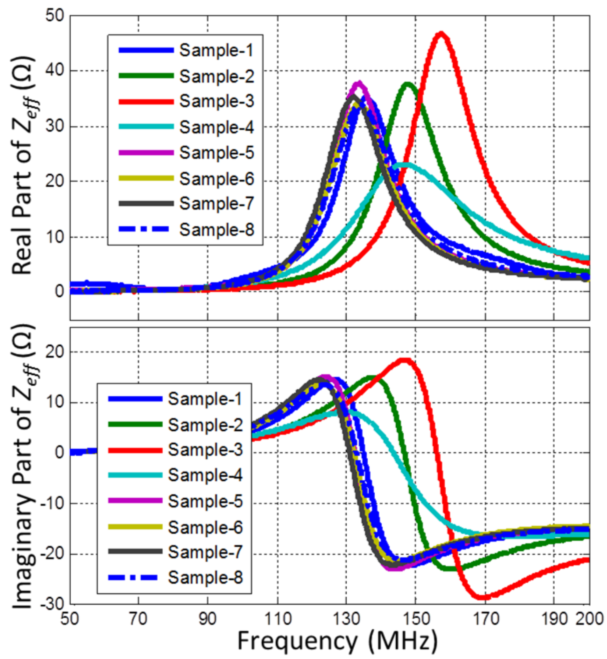

Figure 3.33: Experimental characterization of samples over 8 mm × 8 mm footprint area using a polyimide film with a thickness of 12.5 μm. Eight samples (out of nine) are working but three of them (Samples 2, 3, and 4) have different characteristics due to the fabrication imperfections.

be tuned a pre-defined MRI frequency (123 MHz for this case). Hence, the given size and dielectric combination (8 mm side length with a 12.5 μm polyimide film) is not suitable for 3 T MRI applications.

To achieve the lower resonance frequency with sub-cm footprint dimensions, we replaced our thin-film dielectric with a thinner one, having a thickness of 7.5 μm. The resonator with the footprint area of 8 mm × 8 mm we discussed previously was fabricated and its initial characterization curves areshown in Figure 3.34.

Here, three samples (out of four) were working with reasonable resonance qualities (i.e., Q-factors of about 35-40). Alignment of the second layer on top of the first one was achieved and these experimental results were in agreement with the numerical results reported in Section (3.3). It can be concluded that the proposed size and dielectric combination (i.e., 8 mm side length with a 7.5 μm polyimide thin-film) is suitable for 3 T MRI applications. Additionally, for the targeted MRI applications, with the resonance frequency of about 120 MHz, we tuned these structures by partially removing one of their metallization layers.

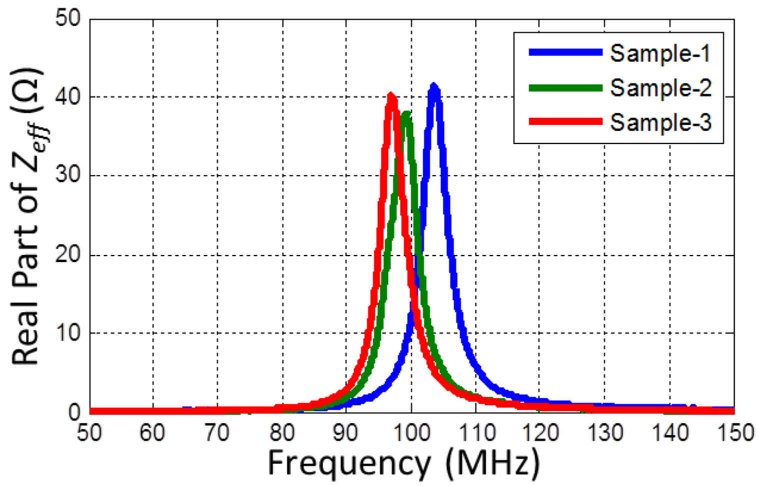

Figure 3.34: Experimental results of the fabricated samples with 8 mm $\times$ 8 mm footprint area using a polyimide film with a thickness of 7.5 μm. Three samples (out of four) are working with slightly different characteristics due to fabrication imperfections.

Results of the experimental tuning steps are shown in Figure 3.35.

Here, one of the fabricated structures (Sample-3 of the Figure 3.35) has been tuned to the targeted frequency of about 120 MHz by partially removing one of its layers. Removal of 20% of the top layer, with a corresponding area of about 5.2 mm^2 (as the overall top layer has a surface area of 26 mm^2 before removal) results in perfect tuning to 123 MHz in free space. These experimental results are in agreement with the numerical results reported in Section 3.3. Similarly the Q-factors of the proposed structures were increased to about 50 after tuning.

It is observed that the tuning of flexible structures from 100 to 120 MHz results in the increased Q-factor, which is in agreement with the proposed circuit model (Q-factor= $w\ L_{eff}/R_{eff}$). On the other hand, it is reported that the Q-factor of the conventional structures, (e.g., spirals, solenoids and SRRs) does not increase linearly due to the lowered inductance for the consecutive turns [39]. Hence, this geometry is very special in terms of its improved Q-factor due to the strong mutual coupling among consecutive layers and the lowered resonance frequency for the same footprint area.

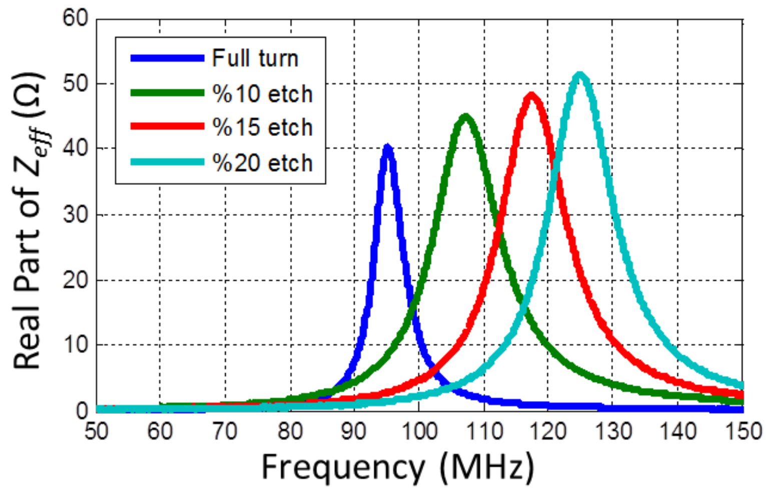

Figure 3.35: Sample-3, given in the previous figure is tuned to the targeted frequency of about 120 MHz by partially removing top layer with the given percentages. Experimental and numerical results are in agreement.

Tuned resonators were also immersed into a body-mimicking phantom to measure their Q-factors. We found that the Q-factors decreased to about 40 (from 50 in free space), which is reasonably lower compared to conventional structures reported in the literature [59]. Hence, we observed that the proposed resonator architecture also provides higher Q-factors even when loaded with lossy phantoms, which makes this resonator structure a very powerful candidate for in-vivo applications.

We aso microfabricated a resonator with a 6 mm side length onto a rigid silicon $< 111 >$ substrate to achieve the smallest electrical footprint area (without targeting a predefined operational frequency). By using a hard mask with complementary SRR patterns, we thermally evaporated two 10 μm thick SRR layers made of gold (chosen due to biocompatibility) that sandwiches a 1 μm thick plasma-enhanced chemical vapor deposited (PECVD) silicon nitride (Si_3N_4) between each other. The optical image of microfabricated devices are depicted in Figure 3.26.

In Figure 3.36, it is seen that three samples (out of four) were working with reasonable resonance qualities. Similar to our previous fabrication experience, alignment of the second layer on top of the first one was achieved with a lower success rate. These experimental results are in agreement with the numerical

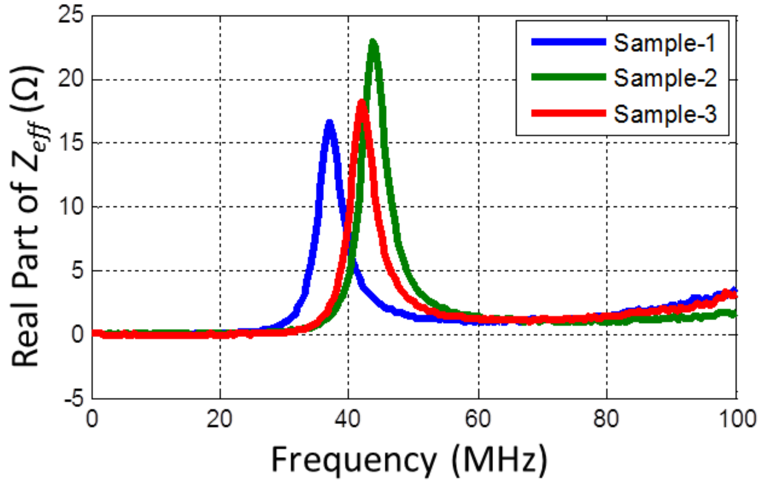

Figure 3.36: Experimental characterization of the fabricated samples over 6 mm × 6 mm footprint area using a rigid silicon wafer with a siliconnitride thickness of 1 μm. Three samples (out of four) are working with slightly different characteristics due to the fabrication imperfections.

models described in Section 3.2. Additionally, for most of the clinical MRI applications, with the resonance frequencies of above 60 MHz, these structures can be tuned by partially removing one of their metallization layers.

We also found that the resonance frequency of the rigid samples (6 mm × 6 mm resonator sandwiching a 1 μm thick siliconnitride) to be 33.4 MHz with a corresponding free-space wavelength (λ_0) of 8.98 m. By using FWHM, we calculated a Q-factor of about 13 for this resonance frequency (due to the losses sourced from the silicon substrate). We found that the side length of the rigid resonator (6 mm) is shorter than $\lambda_0/1500$, which is one of the smallest single-chip deep sub-wavelength resonators reported thus far in the literature [60]. Although a theoretical work with a side length of $\lambda_0/1733$ [61] and an experimental work with lumped capacitors having a side length of $\lambda_0/2000$ [62] were reported, there is no experimental demonstration for a self-resonant structure smaller than the presented architecture here, to the best of our knowledge.

3.6 Metamaterial Characterization

It was previously shown that the full-turn helical structures are a chiral metamaterials [54] and capacitor-loaded SRRs are also a metastructure [63], but there has been no study or evidence on the metamaterial characteristic properties of the partial-turn thin-film loaded resonator architectures. To prove this, we used CST Microwave Studio to acquire the complex reflection parameters (S_{11} and S_{21}). In this simulation environment, we constructed the resonator in the xy plane with a unitcell boundary conditions in the $\hat{x}$ and $\hat{y}$ directions. Simulation ports were located in the $\hat{z}$ direction with open boundary conditions and simulation domain was extended over 8 mm in both the positive and negative $\hat{z}$ directions. Complex S_{11} and S_{21} parameters were exported using the graphical user interface of the CST Microwave Studio to process with MATLAB. The acquired scattering parameters were used to retrieve the effective relative permittivity (ϵ_r) and permeability (μ_r) of the metastructure by applying the methods described elsewhere [64].

To obtain these constitutive parameters, we first calculated the complex reflection (Γ) and transmission (T) coefficients by using the parameter K, as given in Equations (3.17-3.19):

$$K = \frac{1 + S_{11}^2 - S_{21}^2}{2\ S_{11}} \tag{3.17}$$

$$\Gamma = K \pm \sqrt{K^2 - 1} = |\Gamma| e^{j\phi} \tag{3.18}$$

$$T = \frac{S_{11} + S_{21} - \Gamma}{1 - (S_{11} + S_{21})\Gamma} \tag{3.19}$$

To have a physical meaning, the sign of K was chosen such that the $|\Gamma| < 1$, resulting in the radiation coefficient (γ) given by Equation (3.20):

$$\gamma = \frac{ln(\frac{1}{T})}{d} + j\frac{2n\pi - \phi}{d} \ for \ \ n = 0, \pm 1, \pm 2, \pm 3, ... \tag{3.20}$$

where d is the distance between two waveguide ports. From these propagation numbers, relative complex permittivity and permeability were calculated as given in Equations (3.21 and 3.22):

$$\epsilon^* = \frac{\gamma}{\gamma_0}(\frac{1-\Gamma}{1+\Gamma}) \tag{3.21}$$

$$\mu^* = \frac{\gamma}{\gamma_0}(\frac{1+\Gamma}{1-\Gamma}) \tag{3.22}$$

where γ_0 is the complex radiation constant for free space.

Here, we observed that the real parts of the effective permittivity and the permeability of the proposed metamaterial both exhibit negative values near the resonance frequency, which does not naturally exist in classical materials.

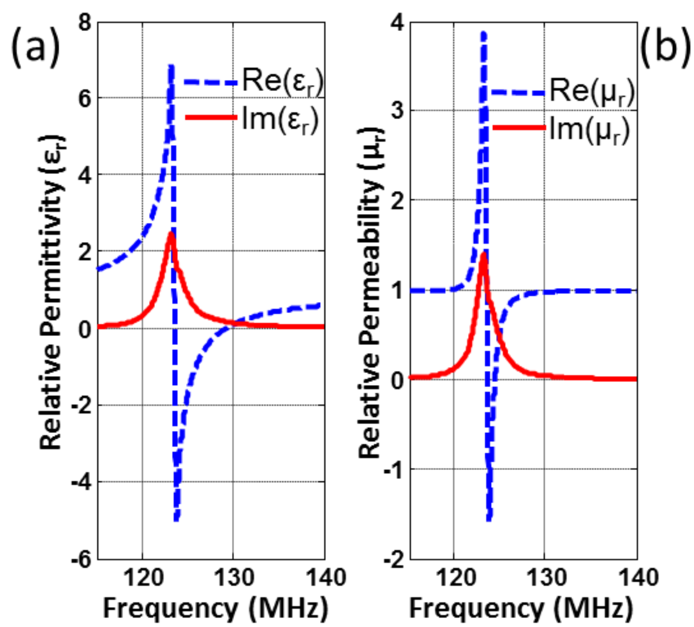

Figure 3.37: Retrieved material parameters of the tuned resonator for MR imaging: (a) the effective relative permittivity, ϵ_r, and (b) effective relative permeability, μ_r, of this metamaterial architecture have negative values around its resonance frequency.

We found that the proposed resonator structure with its tuned geometry still preserves its metamaterial property in terms of its negative constitutive parameters. This is accomplished by properly manipulating EM field within its geometry to have strong resonance characteristics with a high Q-factor. Hence, the proposed resonator architecture is shown to be a tunable metamaterial architecture with an extraordinary tuning bandwidth and a high Q-factor, suitable for various applications including in-vivo imaging practices.

Chapter 4

MRI with Wireless Resonators

MRI has been attracting increasing interest for the localization of implantable devices (e.g., subdural electrodes). Although the soft tissue contrast of MRI [1] makes it the strongest candidate among other imaging modalities (such as X-ray, CT, and PET), the positioning of devices under MRI requires special treatments including the use of wired connections [6–11], introducing MRI marker materials [12–17], and using wireless passive devices with inductive coupling [18, 19].

The use of wireless resonant devices is potentially highly promising to mark implantable devices without requiring multimodal imaging. MRI performance of these wireless markers is loosely dependent on the imaging parameters (TR, TE and resolution). However, this requires novel resonator designs for proper operation. Physical dimensions of these markers together with RF safety concerns should be considered for the surrounding tissues [20].

In this chapter, we characterized our proposed thin-film resonator architecture that alleviates the potential complications of the previous works in the literature. Intensity distribution maps, B1 field distribution, SNR and SAR distribution of this proposed resonator for various imaging configuration are provided. Experimental temperature studies showed that the proposed devices can be used for in-vivo applications. This may open up new possibilities for the next-generation implants that contain their own wireless e-markers integrated on them.

4.1 Intensity Distribution Maps

As discussed earlier, MRI signal strength is dependent on the magnetic field distribution in a tissue. Conventionally, it is mostly accepted that the higher the signal strength is, the better the signal-to-noise ratio is for a given MR image. The most primitive method to understand the relative signal quality of a given MRI image is to characterize its intensity distribution.

MRI measurements were taken using a 3 T Siemens Tim Trio System with a body-mimicking liquid phantom composed of 2 mM copper sulfide solution ($CuSO_4.5H_2O$, with %98 purity of Merck) and 50 mM of NaCl, which mimics most of the tissues [65], with a relative permittivity of around 60, conductivity of 0.5 S/m [66], T1 of 140 ms and T2 of 88 ms. T1 and T2 measurement results are shown in Figure 4.1.

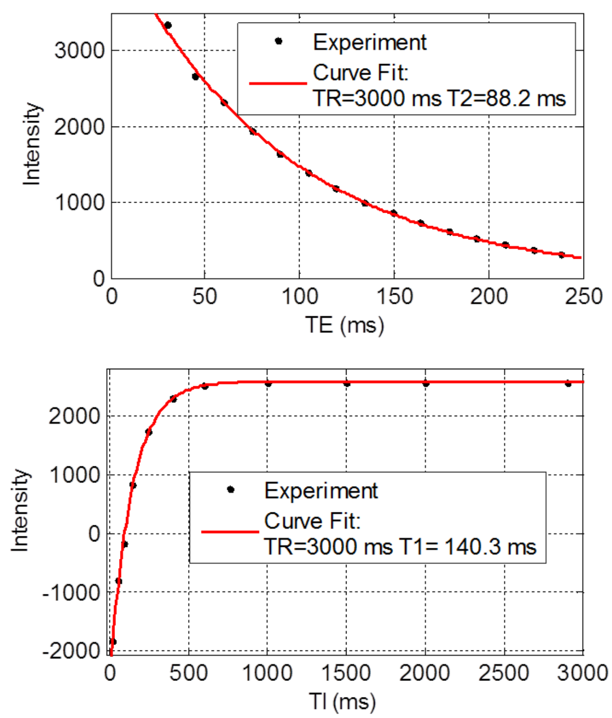

Figure 4.1: T1 and T2 parameters of the prepared phantom. T1 was measured to be about 140 ms and T2, to be about 88 ms.

The characteristic parameters of this phantom are suitable to analyze the in-vivo loading performance of our resonator. Here, initial images were acquired by using a body coil as the transmitter and a standard twelve-channel head coil as the receiver. We used spoiled gradient echo sequence (also known as the gradient-recalled echo, GrE), with a 100 mm × 100 mm field of view (FOV) in the transverse plane, a 256 × 256 image resolution, a 2 mm slice thickness, TR/TE of 100 ms/10 ms, a 260 Hz pixel bandwidth, a flip angle of 10° and a total imaging duration of 29 s. Figure 4.2 depicts the intensity distribution of our resonator with a footprint area of 8 mm × 8 mm.

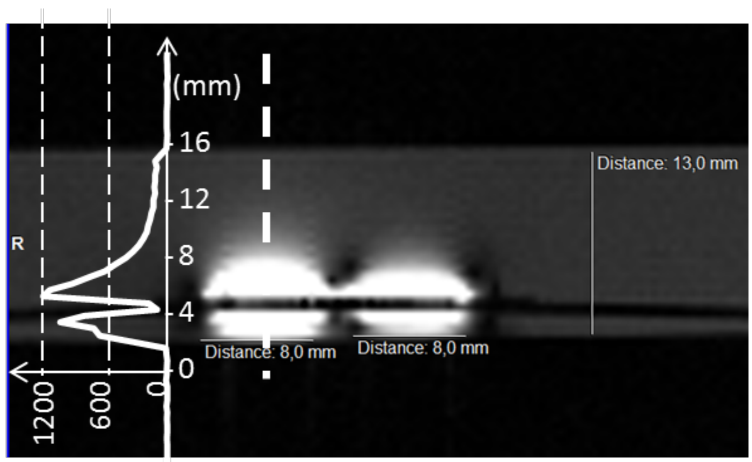

Figure 4.2: Intensity distribution of the proposed resonator with a footprint area of 8 mm × 8 mm.

Here we found that the image intensity level, for the applied flip angle of 10°, was amplified from 80 to 1200 for the close vicinity of the resonator. Similarly, at 4 mm away from the resonator, signal intensity was about 600, which is 7.5 times higher than the original intensity level. Signal intensity drops to about 120 (1.5 times the original intensity level), at a distance 8 mm away from the resonator, which is also the side length of the resonator itself.

As reported in Figure 4.3, this characterization was extended to different flip angles for the same imaging parameters as described in Figure 4.2. It is observed that the signal intensity, within the existence of the resonator, was always higher than the resonator-free case. But, the intensity amplification of the resonator was strictly dependent on the imaging angle. This makes the characterization of the proposed structure difficult. Hence, a more reliable MRI characterization method, B1 mapping, is needed to give a better explanation for the operating principle of this resonator.

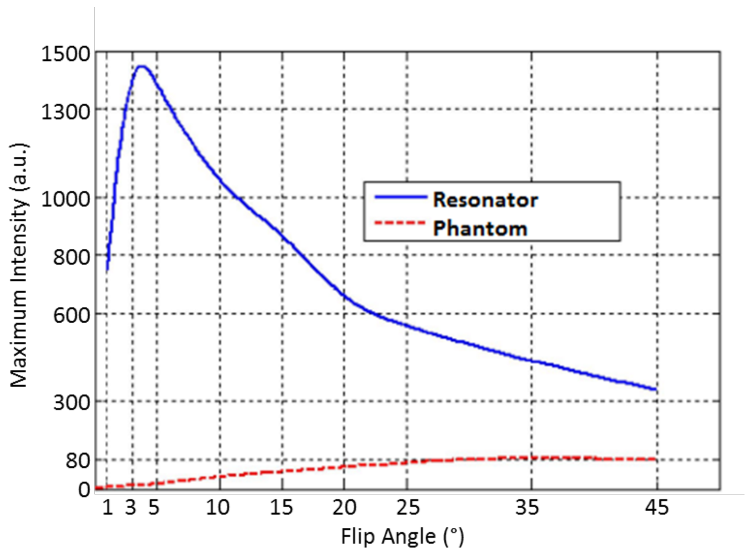

Figure 4.3: Flip-angle characterization of the proposed resonator.

4.2 B1 Mapping of Wireless Resonators

B1 mapping is used in several applications in MRI including T1 mapping [67], transmit gain adjustment [68–70] and chemical shift imaging. B1 mapping can be done either by using signal intensity based methods or by using phase based methods [71]. Intensity based methods strictly depend on the applied RF flip angle, where the double angle method [72] and fitting progressively increasing flip angles [73] are two common methods in this category.

These methods suffer from the followings: requirement of large TR to eliminate T1 effects, higher flip angle to acquire enough signal level (lower flip angles or 180° flip angle cannot be successfully mapped) and higher RF power deposition for large flip angles or reset pulses to handle T1 dependence. To eliminate these problems, Bloch-Siegert method is utilized [74].

The relationship between the B1 and flip angle is given in Equation (4.1):

$$\alpha = \int_0^{\tau} \gamma B_1(t)dt \tag{4.1}$$

4.2.1 Double Angle Method

In this method, by assuming that the TR is large enough to have complete decay/recovery, a saturated GRE sequence with the flip angles of α and 2α is applied to obtain two different images of the same scene. By assuming that the signal intensity is sinusoidally dependent on the flip angle, we can apply the following solution to extract flip angle:

$$S1 = I_0 sin(\alpha)$$

$$S2 = I_0 sin(2\alpha) = I_0 2 sin(\alpha) cos(\alpha)$$

$$\alpha = cos^{-1}(\frac{S2}{2S1}) \tag{4.2}$$

where I_0 is the signal intensity maximum, S1 and S2 are the signal intensities of each pixel for the corresponding MRIs. By using the Equation (4.1), one can extract the B1 map for the given resonator for every pixel.

MRI measurements were taken by using the same configuration as given in Section 4.1 with a TR of 2000 ms. To extract experimental B1 map with the double angle method, we used two saturated GrE images with the flip angles of 10° and 20°. Results are shown in Figure 4.4.

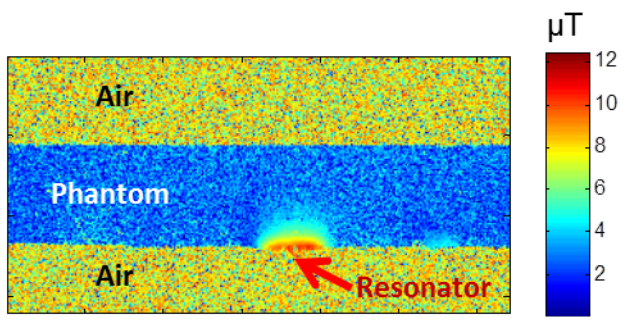

Figure 4.4: Experimental B1 mapping of the proposed resonator structure by using double angle method.

It is seen that the phantom has the B1 map distribution of about 2 μT, where the vicinity of the resonator is amplified to around 12 μT. Additionally, it is observed that the air regions do not converge to a reliable value due to the lowered SNR.

4.2.2 Progressive Fit to Multiple Angles

It is clearly observed that the double angle method fails to provide convergent results for lower SNR values. To overcome this problem, we repeated the previous experiments with the same imaging configuration and with several flip angles to fit a curve to the intensity values. A new imaging set up with the same phantom was used to verify and validate this method. Figure 4.5, shows the phantom with arbitrary features positioned in it. Here, MRIs with progressive flip angles (starting from 5° to 90° with 5° incremental values) were acquired and the obtained image intensities were analyzed for their characteristics.

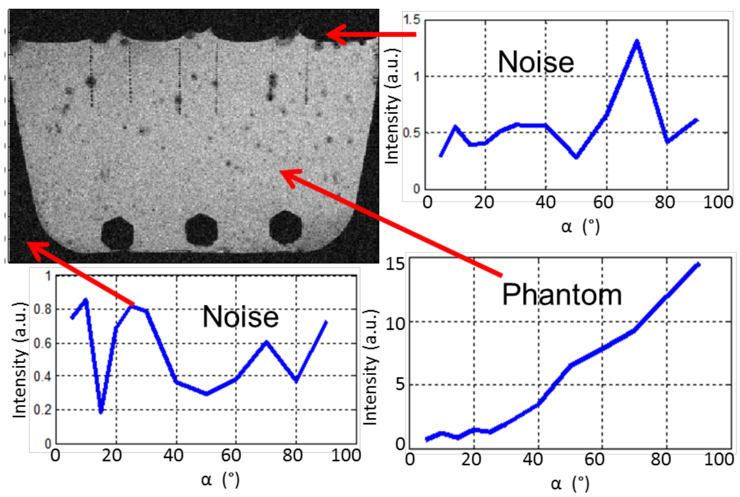

Figure 4.5: MR image of the new imaging set-up with the same phantom. The same imaging slice was acquired for different flip angles to obtain intensity pattern.

We observed that the phantom signal has a sinusoidal pattern as expected (in the bottom-right of Figure 4.5), whereas the noise signal has almost a random pattern with an average of 0.5. These imaging experiments verified the signaling equation (Equation 4.2).

A resonator was placed on top of the phantom to verify its characteristics by fitting an equation to its multiple angle intensity patterns. The new results, with the same imaging parameters as described above, are depicted in Figure 4.6. From Figure 4.6, it is clearly seen that the image intensity is increasing in the vicinity of the resonator, where it is naturally lower in the far away distances. Conventional explanation for the intensity improvement includes the flip angle distribution, but this is not enough to explain the behavior in this scenario. If this were the case, the maximum intensity of all plots should have reach the same value. However, they are significantly different and the equation of $S(\alpha) = I_0 sin(\alpha)$ does not suffice to explain this situation.

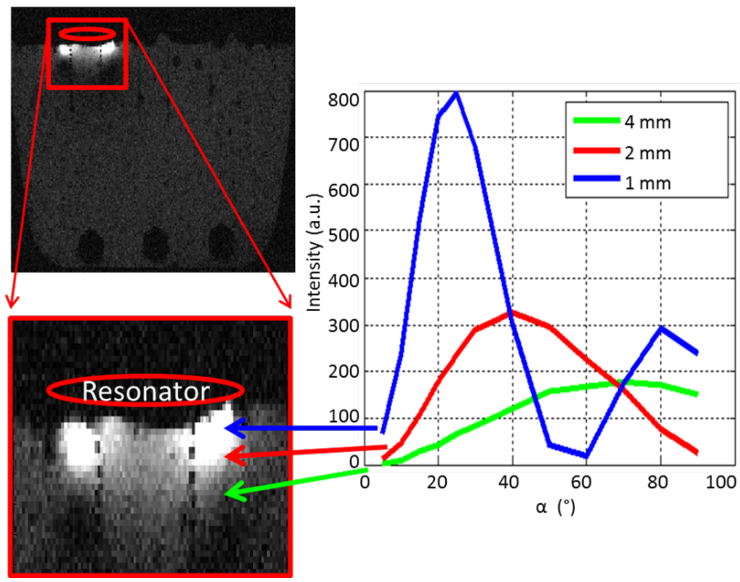

Figure 4.6: MRI of the same imaging set-up in the presence of the resonator. Intensity patterns acquired from 1, 2, and 4 mm away from the resonator are plotted to understand its characteristics.

The brightness of certain regions close to the resonator can be seen, which occurs because of two reasons: the first one is due to the inductive coupling of transmit-field ($B1^+$ improvement) and the second is due to the receive-field inductive coupling. Applied RF power induces surface currents proportional to the resonator Q-factor, which in return creates an effective $B1^+$ field distribution in its vicinity ($B1_Q^+ \propto Q\ B1^+$). The new flip angle (α) distribution will be proportional to this new $B1_Q^+$ field distribution ($\alpha \propto \gamma B1_Q^+\ \tau$, where γ is the gyromagnetic ratio and τ is the RF signal duration). Hence, the transmit field contribution to the imaging signal will be proportional to $sin(\alpha) \propto sin(\gamma Q B1^+ \tau)$. Thus, the image intensity distribution will depend on the Q-factor and the $B1^+$ distribution due to the spatial distribution of this flip angle.

Once the spins are excited in the presence of a resonator, they emit precession signal that is captured by the resonator and transmitted to the receiver antennas. This process known as receive-field coupling is a straightforward RF phenomenon, which is proportional to the Q-factor of the resonator [75]. Hence, the overall

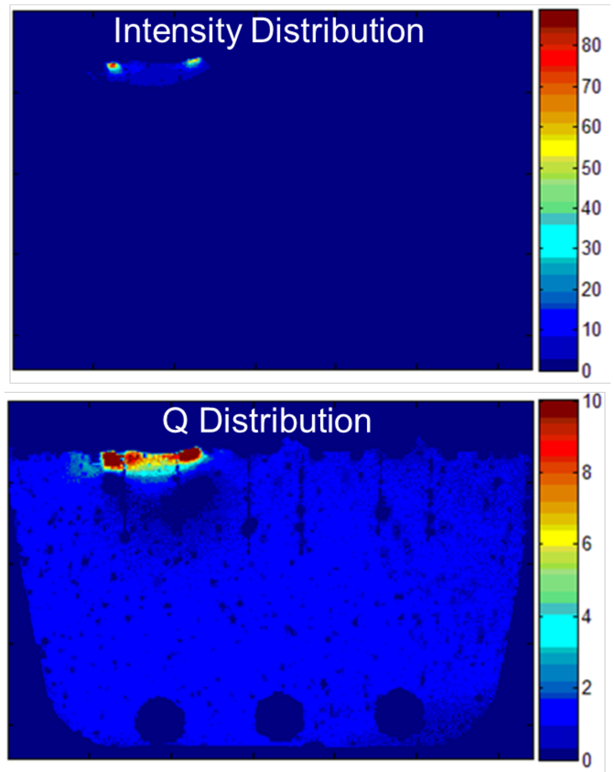

Figure 4.7: B1 mapping by using multiple angle method shows that Q-factor of the resonator significantly affects the image intensity.

image intensity enhancement profile will be proportional to the multiplication of these two effects. (SQ=$|I_0 Q sin(Q\alpha)|$), here note that Q is position dependent). The distribution of Q and I_0Q is provided in Figure 4.7. We observed that this method eliminates the effect of noise and resulting in better characterization results.

Here, a more robust method to obtain the B1 map of a given device is studied. It is seen that the Q-factor of our resonator is affecting not only the flip angle distribution but also the reception efficiency of the system due to mutual coupling between the resonator and the receiver antennas. We observed that the Q-factor of such a resonator as ours can be estimated by using this method.

4.2.3 Bloch-Siegert Method

The Bloch-Siegert (BS) method determines the resonance frequency shift of a nucleus under off-resonance RF field excitation [74, 76]. If RF field is applied with a frequency sufficiently far away from the resonance frequency of a spin or with a special pulse shape to leave the spin as if it is not excited, the precession frequency of the spins changes [77]. This off-resonance precession frequency is dependent on the B1 field and the difference between the spin resonance and RF frequency, w_{RF}.

Figure 4.8 shows the effective B1 field in rotating frame ($B1_{eff}$). By applying a proper Bloch-Siegert shift during excitation and knowing the resonance frequency of the nucleus, one can deduce the resonance frequency offset, which is equal to γB1.

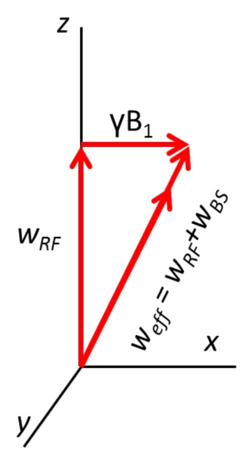

Figure 4.8: Bloch-Siegert signaling scheme for B1 map extraction.

In this rotating frame, the $B1_{eff}$ field is constant, and is given by Equations (4.3):

$$\gamma B1_{eff} = \sqrt{w_{RF}^2 + \gamma B1^2} \tag{4.3}$$

For a large off resonance $w_{RF} >> \gamma$ B1, a trigonometric identity can be used to solve for w_{BS} according to Equations (4.4 and 4.5) [76]:

$$(w_{BS} + w_{RF})^2 = w_{RF}^2 + (\gamma B1)^2 \tag{4.4}$$

$$w_{BS} = \frac{(\gamma B1)^2}{2w_{RF}} \tag{4.5}$$

and the phase shift (ϕ_{BS}) due to the Bloch-Siegert shift is given by Equation (4.6):

$$\phi_{BS} = \int_0^T w_{BS}(t)dt = \int_0^T \frac{(\gamma B1_t)^2}{2\ w_{RF}(t)}dt \tag{4.6}$$

The expected phase shift can be calculated from Equation (4.6) for any arbitrary pulse B1(t) with a constant or time-dependent frequency offset $w_{RF}(t)$.

This method requires taking the difference of two scans to remove additional, undesired phase effects in the image [78]. By keeping all the other factors the same in both scans, we applied the BS shift of 4 kHz to calculate B1.

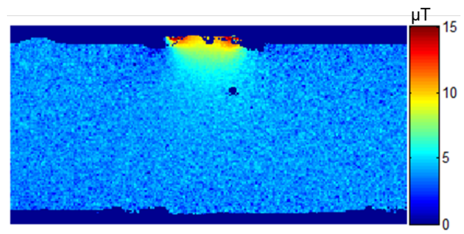

Figure 4.9: Experimental B1 map of the proposed resonator by using Bloch-Siegert mehtod.

In Figure 4.9, we see that the phantom regions have the B1 map of about 2-4 μT, where the resonator has almost 15 μT B1 map level in its vicinity. These B1 map results are in agreement with the previous methods (e.g., double angle and multiple angles).

4.3 SNR Mapping

SNR of an MR image is one of the key metrics, which depends on several parameters including the DC magnetic field strength, pixel volume, repetition time, echo time, T1 and T2 of the imaged material, and the imaging sequence. For all the other parameters kept constant, having a higher B1 value will result in better SNR performance. This can be achieved by using improved antenna systems and/or using passive wireless coils (as proposed in this thesis work) closer to the imaged volume. Since the B1 performance of the proposed resonator has been discussed earlier, here we will mainly focus on the SNR improvement performance of this structure.

SNR calculation of complex valued MR images was proposed by Henkelman [79]. A predetermined slice is imaged several times to properly see the effect of noise in the consecutive slices. Graphical representation of this method is illustrated in Figure 4.10.

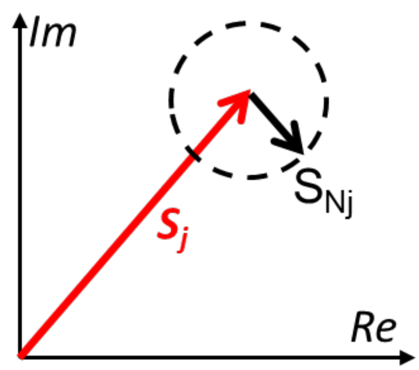

Figure 4.10: Representation of noise calculation for complex valued pixels.

Here, S_j is the complex signal strength of the j^{th} pixel and S_{Nj} is the noise signal in that pixel for the given image frame. It is assumed that the noise signal has a Gaussian distribution with a zero mean. Hence, different images of the same frame are averaged to find the mean of the signal level of each pixel. Similarly, the standard deviation of these images for a given pixel represents the complex noise. For the regions with sufficiently higher signal intensities (e.g., $S_j >> S_{Nj}$), this method converges to real values quickly.

To implement this method, we prepared an MR imaging set-up with the same phantom as defined earlier. MR images were acquired by using GRE with an 80 mm $\times$ 80 mm FOV in transverse plane, a 2 mm slice thickness, TR/TE of 100 ms/10 ms, a 260 Hz pixel bandwidth, and a flip angle of 10° and applying different imaging resolution and numbers of acquisition (NA) to observe the effect of voxel size on SNR. Figure 4.11 depicts the SNR distribution of this set-up with

448 × 448 imaging resolution (178 μm for each pixel) and an NA of 5.

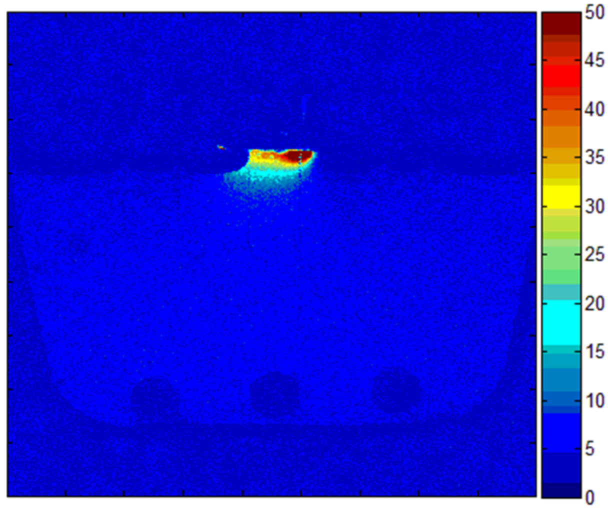

Figure 4.11: SNR of an image for NA=5 and a pixel size of 178 μm.

Here we found that the signal intensity is amplified more than an order of magnitude in the vicinity of the resonator for this case. Including the other imaging scenarios, we plotted the curve provided in Figure 4.12 to depict the SNR performance of the proposed architecture.

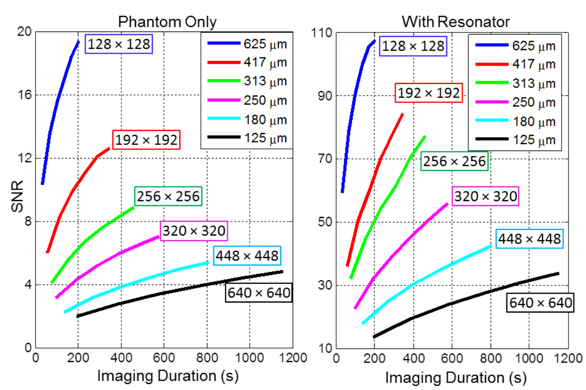

Figure 4.12: SNR performance of the proposed resonator for different imaging resolution for 80 mm × 80 mm FOV: (left) without and (right) with the resonator.

From Figure 4.12, independent from the imaging resolution, it is observed that over five fold time SNR improvement is achieved. Similarly, for an imaging resolution of 640 × 640 (corresponding to a pixel resolution of 125 μm in transverse plane), it is not possible to reach the SNR level of 10 for the phantom, whereas it is always over 10 in the case of using the resonator. To make the situation clearer, let"s choose an arbitrary point with an SNR of about 20 for the resonator-free case (left graph). We can choose a 625 μm pixel size with 200 s of imaging duration. On the right side, for the same SNR, we can either image the same system with about a 180 μm pixel size at the same time or with the same pixel size but in less than 20 s. Using a resonator for a given FOV allows us to image a volume either with a very high resolution or with the same resolution but using fast imaging parameters. We believe that this introduces great flexibility for several medical applications including angiographs in flow studies.

4.4 SAR Distribution

To futher study the resonator architecture, we simulated a 3-dimensional body model from the library of CST Microwave Studio using a birdcage coil with a diameter of 70 cm and a length of 120 cm tuned to 123 MHz. It was previously proven that the tissue parameters (hence, RF characteristics) of adults and children [80, 81] and the performance levels of different solvers [82] are not considerably different from each other. Thus, here we used a children body model to decrease the computational burden as a result of the reduced tissue volume. Numerical SAR results were acquired by using a time-domain solver and a power loss monitor. Time-averaged SAR values were calculated by using the time derivative of the incremental energy (absorbed by an incremental mass of 1 and 10 g of tissues).

By using the child phantom from the CST library, we computed the SAR distribution in the head of the given data set. Figure 4.13 shows the SAR maps of the imaged subject for the sagittal plane that includes the region of the highest SAR with 1 and 10 g averaging. To understand its effect, we located the resonator at the point with the highest SAR and ran the solvers to compute the second SAR maps as shown in Figure 4.13 (b) and 4.13(d), respectively.

These results showed that the SAR is increased from 1.09 to 1.91 W/kg for 1 g of averaging and 0.763 to 1.22 W/kg for 10 g of averaging. These numbers should be considered to determine the upper limit of the applied RF power for the imaging sequences for the patients when using such a resonator in vivo. Within this limit, the resonator will outperform the resonator-free case by a level better

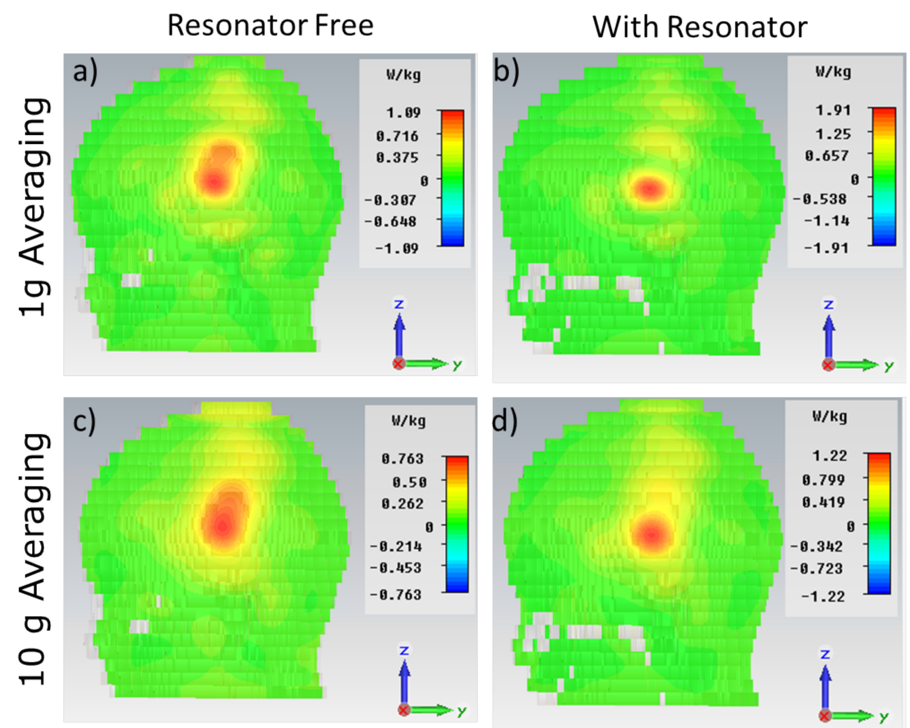

Figure 4.13: SAR distribution results of the resonator for the child data set: (a) 1 g of averaging without resonator, (b) 1 g of averaging with resonator, (c) 10 g of averaging without resonator, and (d) 10 g of averaging with resonator.

than an order of magnitude in terms of the image intensity, proving the substantial benefit in its usage.

4.5 Temperature Study

The transmit field coupling to a resonator is the main reason for tissue heating due to the scattered electric field from the structure. Resonant behavior of the such devices results in confined electric field outside their structure that causes tissue heating. To analyze the tissue heating, thus the RF safety, of the proposed resonator, we immersed a tuned resonator into a cylindrical gel phantom with 40 cm in diameter and 25 cm in height (heat resistivity=0.661 W/mK, heat conductivity=1.513 mK/W, heat capacity=4454 J/kg K, and diffusivity=1.48 mm^2/s). Before starting with an MRI experiment, we numerically calculated the electric field distribution of the resonator immersed into this phantom. From these calculations, we determined the possible region with the highest SAR values, where the highest region has an SAR increase of about %40.

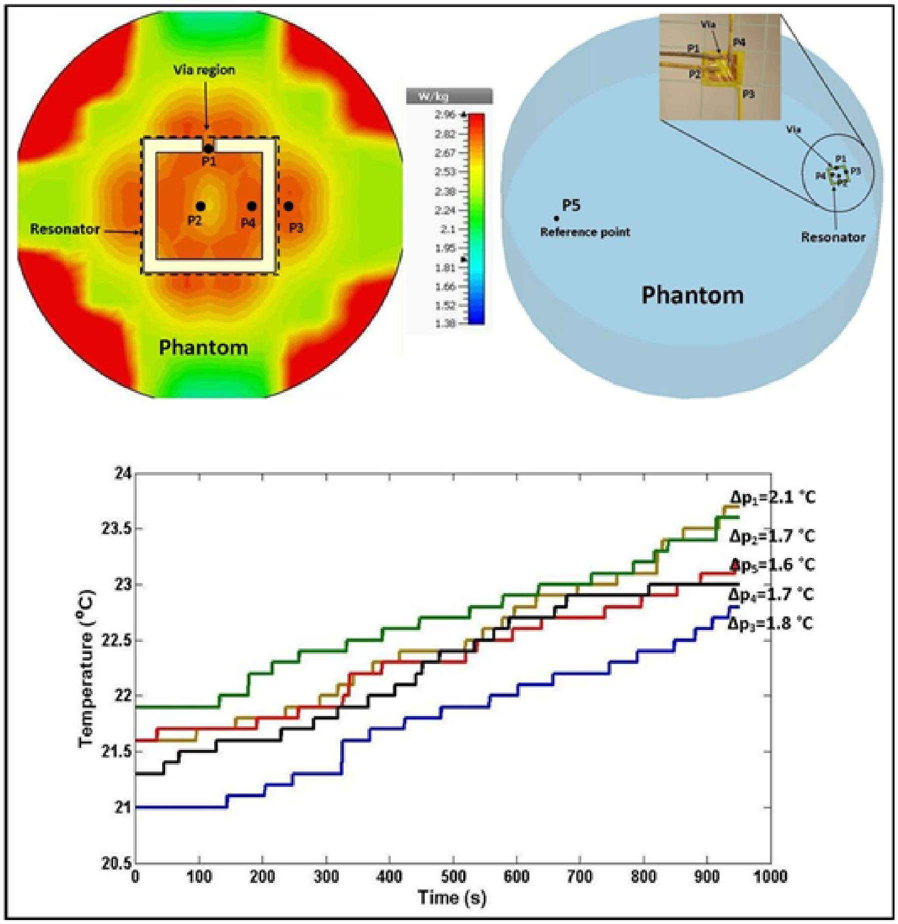

Figure 4.14: A tuned resonator loaded into a cylindrical phantom and numerically evaluated for the highest SAR regions (top left). Experimental set-up was prepared by using the same configuration with a five fiberoptical temperature sensing lumens located properly (top right). Here the temperature increase measured by four probes is not significantly different than the reference probe (the fifth one), which was located very far from the resonator (bottom). The proposed resonator is expected to be RF safe [48].

Four fiber tips (P_1-P_4) of an optical thermometer (Neoptix, RF-04-1, Fiber optical temperature sensor, Canada) were positioned inside the phantom near the resonator as depicted in Figure 4.14. The last fiber tip, P5 was used as a reference electrode that is located 25 cm away from the resonator. The experimental set-up was exposed to a high SAR sequence (GRE: TR=2.6 ms, TE=1.5 ms, FA=50, slice thickness=200 mm, FOV =220 × 220 mm^2, average=32). The total acquisition time was 16 min at a B1-field strength of 14 μT.

RF heating measurement of the resonator was measured under continuous high SAR MRI pulse sequence. All the fiber sensors experienced similar temperature raises ($P_1 = 2.1°C$, $P_2 = 1.7°C$, $P_3 = 1.8°C$, $P_4 = 1.7°C$ and $P_5 = 1.6°C$). The measured temperature difference was the highest at the point P_1 with a temperature difference of $2.1°C$. We may claim that the electric field distribution of the resonator is relatively homogeneous, which is due to its thin-film loading scheme, to lead to uniform temperature increase along with its geometry. We experimentally observed that the maximum SAR increase was obtained with 60% under these circumstances, which is still below the limits of U.S. food and drug administration (FDA). Although we observed temperature increase in this study, most of the imaging applications do not require such high SAR sequences; hence, RF safety of the proposed resonator can possibly be attained easily.

4.6 Proof-of-Concept Demonstration Under 1.5 T

To verify the operation of the proposed resonator, a device with a 14 mm × 14 mm footprint area was fabricated onto a Kapton polyimide film (which was thinned down using a reactive ion etching) with an initial resonance frequency of 42 MHz and a Q-factor of about 21. This structure was tuned to the operating frequency of a 1.5 T Siemens Scanner located at Hacettepe University, at a resonance frequency of 63.67 MHz. A GRE sequence with a TR of 580 ms, a TE of 14 ms, a FOV of 120 mm × 120 mm, a resolution of 256 × 256, a slice thickness of 5 mm, a pixel bandwidth of 121 Hz and a total acquisition time of 192 s were used to determine the location of the resonator external to a cylindrical phantom. Imaging set-up and 1.5 T MRI images are depicted in Figure 4.15.

We clearly see that the proposed structure, once tuned to the targeted frequency, can be used with different MRI platforms. Since the operating frequencies of about 60 MHz is easily achievable with the footprint area of about 1 cm × 1 cm, we believe this architecture can be used for most of the clinical MRI scanners as an in-vivo and/or ex-vivo imaging device.

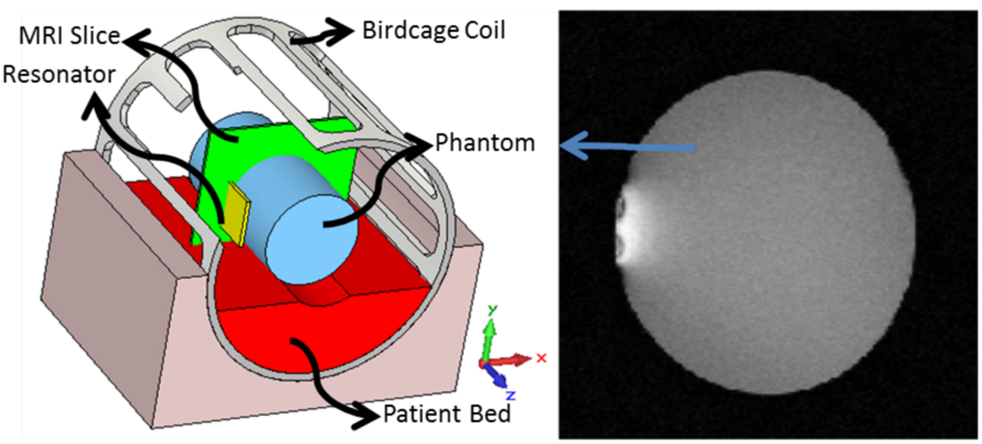

Figure 4.15: Schematic representation of the imaging set-up (left) and the 1.5 T MRI of the resonator that is external to the phantom (right).

Chapter 5

Imaging Applications

This chapter is based on and partially taken from the following publications of the thesis author: S. Gokyar, A. Alipour, E. Unal, E. Atalar, H. V. Demir, Magnetic resonance imaging assisted by wireless passive implantable fiducial e-markers, IEEE Access, vol. 5, issue 1, pp. 19693-19702, (2017), doi: 10.1109/ACCESS.2017.2752649; S.Gokyar, A.Alipour, E.Atalar, and H.V.Demir, "Wireless deep-sub-wavelength metamaterial enabling sub-mm resolution magnetic resonance imaging", in revision Sensors and Actuators: A. Physical (2017); and A.Alipour, S.Gokyar, O.Algin, E.Atalar, and H.V.Demir, "An Inductively coupled ultra-thin, flexible and passive RF resonator for MRI marking and guiding purposes: clinical feasibility", Magn. Reson. in Medicine, (2017), doi: 10.1002/mrm.26996.

5.1 MRI Marking of Subdural Electrodes

For the treatment of epilepsy disease, it is a common method to use subdural electrodes to image defected parts of the brain, where the positioning of the electrodes has crucial importance for the surgery [83]. Correct positioning and high performance imaging of problematic regions improve the success rate of this treatment and help to eliminate excess recession of the brain regions. As mentioned earlier, clinical MRI scans are not suitable to show these electrodes due to lack of ^{1}H atoms in their content. Some magnetic content could be added to these electrodes to make them MRI visible (actually darker), but this comes with a loss of data and increased artifacts near them, which cannot be removed in real time by any MRI method. Position of a non-magnetic subdural electrode cannot thus be determined by MRI. Additional imaging modalities, e.g., X-ray, PET and CT, are therefore required to reveal their locations correctly. The proposed resonator here can allow for marking in MRI together with enabling enhancement in imaging resolution without any timing parameter.

As a proof of concept demonstration, we prepared an imaging environment with an eight-channel open surface coil array, dedicated to animal experiments, and a rabbit used for ex-vivo imaging was placed at the scanner as shown in Figure 5.1. Here necessary steps to obey the national laws (5199, February, 2014), ruled by European Union Directive 2010/63/EU, were applied for animal experiments (Bilkent University, HADYEK permission, 2012/9, ext. 3). The rabbit was positioned on the patient bed of the scanner and transverse images were acquired for marking purposes. Images were acquired by using body coil as the transmitter, surface coil as the receiver with a GRE sequence, 100 mm $\times$ 100 mm FOV in the transverse plane, a 256 $\times$ 256 image resolution, a 2 mm slice thickness, TR/TE of 100 ms/10 ms, a 260 Hz pixel bandwidth, a flip angle of 3° and a total imaging duration of 29 s.

Figure 5.1: An eight-channel open surface coil system used for ex-vivo animal studies.

Although a detailed analysis about the safety of intracranial EEG electrodes under MRI was previously conducted [84], their magnetic content prevents us to use them for GRE sequences. Hence, we fabricated an array of mimicked non-magnetic subdural electrodes. To mimic the operation of subdural electrodes, we deposited Ti/Au metals onto a 12.5 μm thick flexible polyimide film, Kapton, with a diameter of 4 mm and combined them with the resonators by sticking them to each other. The overall electrode-resonator structure was placed external to the head of a rabbit as shown in Figure 5.2.

Standard gradient echo sequences with different imaging parameters were applied to verify the operation of the resonator. Although we presented the MRI acquired by using a flip angle of 3° in Figure 5.2, we observed that it would be as low as 1° for this configuration.

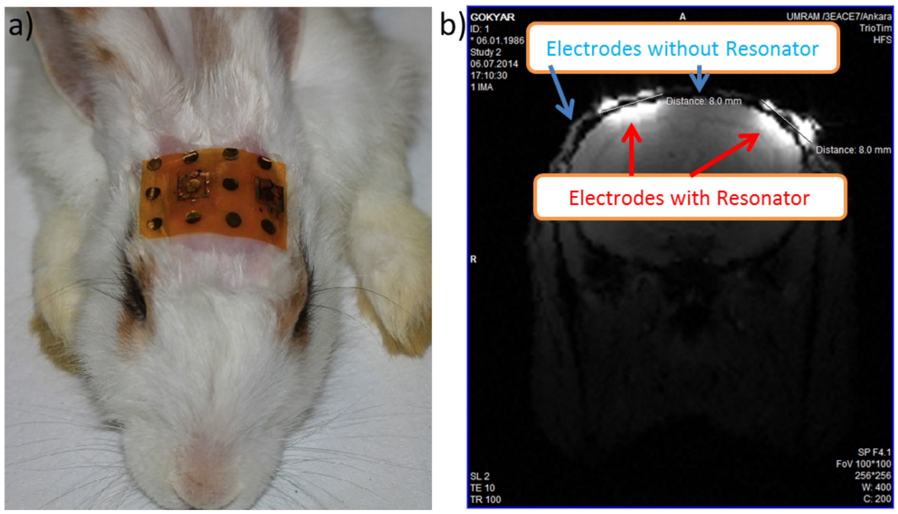

Figure 5.2: Proposed electrode-marker resonator pairs placed onto the head of a rabbit (a). These pairs, as well as the subdural electrodes without resonators, imaged under MRI to localize them. (b) Electrode-marker pairs are clearly marked in the MRI, where the electrodes without markers are not visible.

These MRIs showed that we can clearly mark these electrodes with our resonators whereas the other electrodes without resonators cannot be distinguished in the image. The resulting performance of the resonators is high even in the vicinity of the electrodes. Not only the marking but also the SNR enhancement is possible, which can be clearly seen in Figure 5.2(b). By adding resonators onto all of the electrodes it is thus possible to map each electrode by using only MRI. All of the complications regarding the transportation of patients, mapping of electrodes via CT, PET or X-Ray imaging to obtain clear positioning of electrodes can thus be resolved using this resonator together with the electrodes in MRI and positioning efforts can be significantly simplified [46].

5.2 SNR Improvement for High-Resolution MRI

Following the seminal work of Veselago [85], metamaterials were introduced for different applications including material characterization [86], sensing [33–37, 87–89], compacting devices [90–92], and imaging of sub-wavelength features [93, 94] from optical frequencies [95, 96] to RF region [41]. Operating bandwidth of those metamaterial devices has been typically narrow due to high Q-factor elements used in the unit cell of their structures. Since MRI is basically a narrow bandwidth imaging technique, metamaterials could be greatly attractive for MRI applications. It was indeed previously shown that metamaterial structures can be used for RF flux guiding [97] and SNR improvement purposes [63]. These metamaterials, in addition to conventional imaging hardware of an MRI scanner, properly manipulates the EM fields in their vicinity to increase imaging signal emitted from the imaged objects (e.g., tissues). However, these previous designs are typically larger in size to be used for medical applications. As such, the design of wireless sub-cm metamaterials to address in-vivo MRI of sub-mm features has not been achieved to date.

High-resolution MRI (HR-MRI) suffers the fundamental problem of reduced SNR due to decreased volume of the imaged voxels. To increase the SNR of an MR image, several methods can be applied. These include applying a higher DC magnetic field [98], eploying high density coil arrays with parallel imaging techniques [99, 100], increasing the number of image acquisition and using high-sensitivity wired coils [8, 60, 101–109]. Practically, DC field strength is predetermined and assumed to be constant after the installment of the main magnet. Although using high density coil arrays with parallel imaging techniques is one of the major breakthroughs, their performance can be increased further by using wireless coils for in-vivo applications. Increasing the number of acquired images increases the imaging duration and the total RF power exposure of patients, which is not suitable for clinical imaging practices. Hence, for a predetermined DC field, increasing SNR without increasing the total RF power exposure and imaging duration becomes possible only with localized coil solutions. However, these coils include complicated electronics (e.g., matching capacitors, solder, diodes and/or cryo-cooling) and they are connected to the body of the scanner with RF cables. Thus, their application to in vivo operations is inherently challenging due to RF heating risks [20]. Using wireless metamaterials for in-vivo MRI applications would increase the detection performance of an MRI system [40, 110, 111]. Although the previous wireless designs, including some metamaterials, achieved this purpose to a certain extent, none of them has accomplished an electrical size smaller than $\lambda_0/300$ and a Q-factor larger than 50 simultaneously without using cryo-cooling or lumped element thus far.

In this thesis work, to address the aforementioned problems of HR-MRI, we showed a wireless deep sub-wavelength metastructure enabling a high Q-factor of about 80 in free space, while using a highly compact footprint area. Here this proposed wireless metamaterial architecture, while being electrically very small, is demonstrated to be an excellent candidate for in-vivo MRI applications including HR-MRI at sub-mm resolution level.

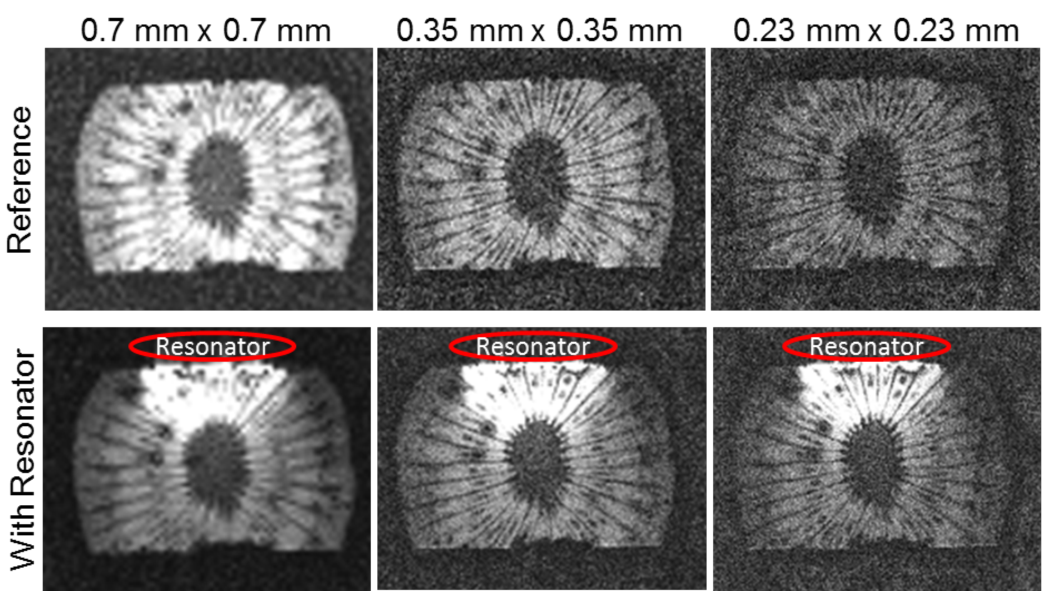

Figure 5.3: Kiwi fruit imaged to visualize its sub-mm features without (top panels) and with (bottom panels) using a resonator. Increasing resolution (decreasing pixel size) is necessary to resolve these sub-mm features, but this reduces SNR. Hence, smaller features cannot be clearly resolved due to noise (top row). However, using a wireless resonator allows us to image these sub-mm features clearly in its vicinity (bottom row).

To highlight the SNR improvement property (hence, imaging smaller features) of the proposed structure, we prepared an imaging set-up by using kiwis. We used a GRE sequence with a transverse imaging slice, TR/TE of 170 ms / 10 ms, a FOV of 90 mm, a flip angle of 25°, a slice thickness of 2 mm, a pixel bandwidth of 260 Hz and resolutions of 128, 256 and 384 pixels in both x and y directions with pixel sizes of 0.70 mm, 0.35 mm and 0.23 mm, respectively. Then, we put the pre-mentioned resonators on top of the kiwi to highlight its sub-mm features.

From Figure 5.3, it is observed that increasing the imaging resolution (increasing the imaging matrix size) results in the decreased voxel size, which in turn reduces the SNR of the pixels. This prevents us to resolve sub-mm features. However, using a wireless resonator in this experimental set-up allows us to image these sub-mm features with higher resolution in its vicinity. If the limited FOV is tolerable, then these resonators serves as a perfect candidate for high-resolution imaging applications.

Additionally, the proposed architecture was located on a coronal plane (XZ plane), where immersed pillars were lined in the z-direction located inside a standard head coil of the scanner as shown in Figure 5.4(a). Transverse images, with the imaging parameters given in Section 4.1., were acquired to count each pillar as presented in Figure 5.4. Here, we observed that the pillar array can be visible only in the vicinity of the resonator that is in agreement with the $B1^+$ map of the resonator as given in Figure 5.4(c). $B1^+$ results showed that the amplitude of the RF magnetic field can be amplified significantly in the vicinity of the resonator.

From the MR image depicted in Figure 5.4(b), we obtained the intensity plots along blue and red lines marked on it. From Figure 5.4(d), we observed that the average noise level corresponds to about 50 arbitrary units (a.u.), where the signal intensity in the neighboring region of the resonator seems to be about 1,000 a.u. Intensity curve in blue drops down to about the noise level for the corresponding pillars in the vicinity of the resonator. We can clearly count the number of dips to be 13, which is the number of pillars in the array. Red curve (at 5 mm away) shows the intensity profile far away from the resonator. It is clearly seen that the pillars 5 mm away from the resonator are not visually separable from each other.

Here we also observed that the signal intensity is amplified by about one order of magnitude (1,000/100) in the vicinity of the resonator. For the pillars close to the resonator metallization, contrast to noise ratio (CNR) reaches about 15.4 (i.e., CNR=(920-150)/50), where CNR drops down to about 6.9 for the 6^{th} and

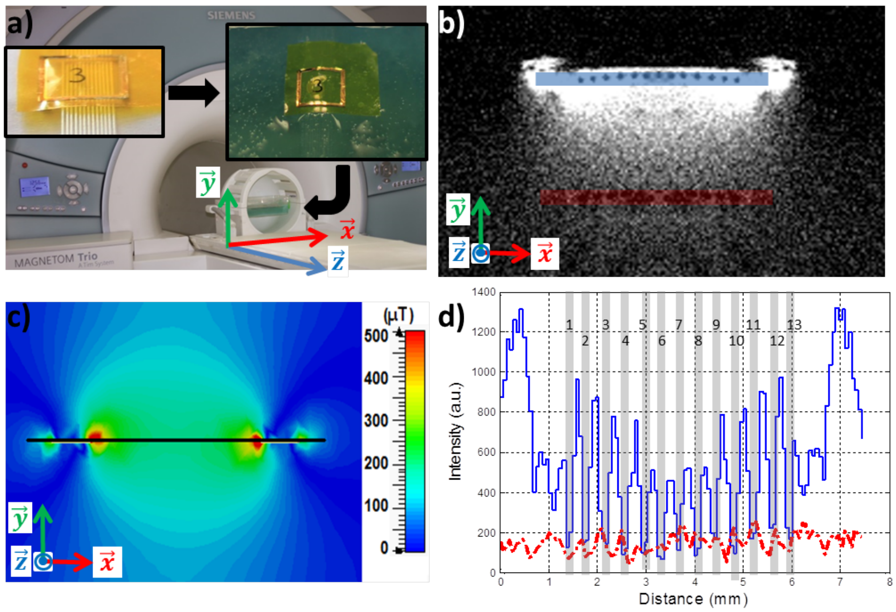

Figure 5.4: MRI characterization of the tuned resonator to resolve the evenly distributed fibers pillars, each with a diameter of 200 μm. (a) 3 T Siemens Magnetom Trio MR imaging system was used with a head coil, loaded with a body mimicking phantom to image fibers immersed into the phantom. (b) MRI image shows that pillars are clearly visible and can be countable in the vicinity of the resonator along the blue line (at 0.1 mm away from the resonator), whereas they are not fully resolvable along the red line (at 5 mm away from the resonator). (c) $B1^+$ map of the wireless metamaterial structure. (d) Red curve shows the image intensity pattern at 5 mm away from the device and the blue curve indicates the image intensity at 0.1 mm away from the device. The blue profile clearly resolves all 13 of these pillars.

7^{th} pillars. This results from the increased SNR in the proximity of the resonator, which was also verified from its $B1^+$ map. For the pillars away from the resonator, CNR drops to about unity. To image smaller objects, e.g., pillars with 200 μm diameter, SNR should be kept high enough to eliminate noise effects. The proposed metamaterial architecture manipulates EM field strongly in its vicinity to increase the SNR and this allows for MRI of sub-mm pillars with an unprecedented resolution for the 3 T head coils, which is otherwise not possible using these imaging parameters [112].

5.3 Other Applications

The proposed resonator architecture can be used as an SNR improvement device. This structure increases the signal level in its vicinity and improves SNR of the image, hence making the features more visible for clinical applications. The device would increase the signal level of any biological tissue. Operational performance of this device is not affected by the values of imaging parameters (including the size of image, applied signal power, imaging bandwidth, imaging duration, applied signal duration, and echo time). From Figure 5.5, we can see that the proposed resonator can be used as an SNR improvement device in extremities (e.g., hand in here) as well as in head. Further systematic studies are needed to explore SNR enhancement in such body parts.

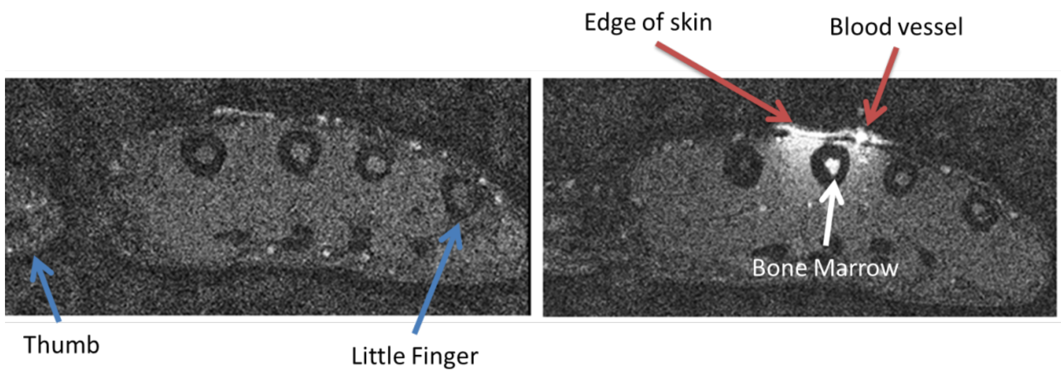

Figure 5.5: MRI of hand without a resonator (left) and with a resonator (right).

Although the proposed architecture would eliminate the need for multimodal imaging, it is still suitable for multimodal imaging if wanted and does not put any direct limitation to conventional imaging practices. To prove this point, we imaged our resonator located on top of phantom by using conventional X-ray imaging. X-ray of the resonator, together with phantom, is presented in Figure 5.6. The resonator is: optically visible (due to construction materials of gold, polyimide, and PDMS), MRI visible (due to the resonance behavior, exhibiting extra-ordinary benefits as explained in the previous sections), and X-ray visible (because of containing very thin metallic paths that absorb x-ray and do not cause any artifacts as can be seen in Figure 5.6). Hence, we can conclude that the proposed architecture can be used for multimodal imaging practices for clinical applications, if desired.

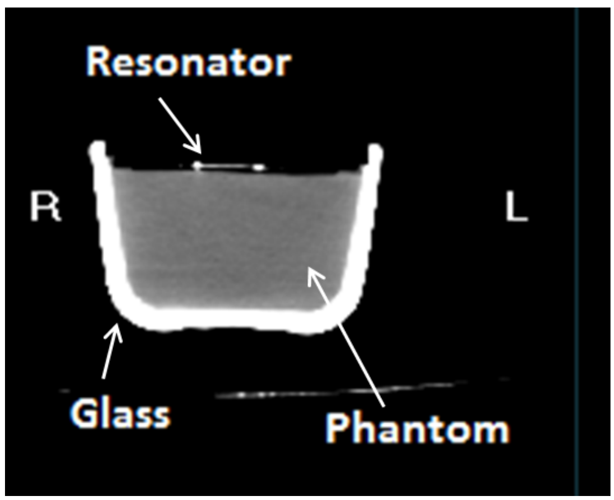

Figure 5.6: Conventional X-ray image of a resonator loaded phantom. Both phantom and the resonator are visible, and unlike other metallic implants reported in the literature, the proposed device does not cause any imaging artifacts in this platform. This guarantees the use of conventional methods.

Chapter 6

Conclusions

In this thesis, we have proposed, designed and demonstrated a thin-film loaded helical metamaterial architecture for wireless RF applications including marking of implants under MRI and signal level enhancement for high-resolution imaging. This proposed flexible architecture is also a good candidate for replacement of lumped capacitors and inductors in conventional systems, including interventional applications, thus, leaving a room for device miniaturization and improved flexibility. Also, the proposed architecture maintains several superior properties such as low footprint area, high Q-factors, maintaining them even under lossy medium loading and simultaneous negative permittivity and permeability.

It is proved that the side length of the proposed architecture can be miniaturized to below $1/1500^{th}$ of its free space resonance wavelength, which is the smallest self-resonating wireless structure reported thus far to the best of our knowledge. Additionally, it has ultra-thin vertical height, which is less than 25 μm, allowing for flexible operation for in-vivo applications. This miniaturization is achieved because of its cross-via metallization located among consecutive layers. Thanks to this special geometry, the proposed structure attains high Q-factors and low resonance frequencies simultaneously (e.g., Q-factor of about 80 for $\lambda_0/400$ operation). We have shown that this proposed device has a 25 times smaller footprint area compared to its conventional counterparts at the same operating frequency (e.g., stacked SRR architectures). This thesis work also provides the imaging results using a 1.5 T (64 MHz) MRI to show a proof of concept demonstration. A footprint area of 14 mm $\times$ 14 mm thin-film loaded helical resonator architecture (with a corresponding side length of $1/335^{th}$ of its free space wavelength) with a Q-factor of about 20 was demonstrated successfully.

We also observed that the conventional equivalent circuit models proposed for SRRs are not suitable for the novel resonator architecture developed in this thesis work. Hence, a proper equivalent circuit model was developed to calculate the characteristic parameters of the proposed architecture. Here it was proven that the cascaded equivalent circuit model accurately calculates the resonance frequency and the Q-factor of the proposed resonator. This equivalent circuit model also explains the reasoning to achieve a smaller footprint area and higher Q-factors simultaneously. Results of this circuit model were also verified by using numerical full-wave solver (CST Microwave Studio) and followed by experimental RF characterization of the microfabricated devices. With this circuit model, it was observed that the ultimate Q-factor of such a thin-film loaded helical resonator is limited by the $1/\delta$ of its dielectric material. We also concluded that increasing the turn ratio (the overlap area or the turn number) of the resonator results in the increased Q-factor because of higher effective inductance.

Unlike conventional lumped resonators, tuning of the proposed resonator architecture is easier and does not introduce complications due to its geometry (e.g., no soldering required, no wiring or bonding was used). This was achieved by changing the overlapping area of the consecutive turns by partial removal of the metallization layers. Doing so, it was demonstrated that the resonance frequency range from 30 MHz to 5.5 GHz was achievable for a footprint area of 6 mm $\times$ 6 mm. This tuning range is extraordinarily wide compared to the tuning capability of conventional devices reported in the literature (e.g., for SRRs $< 10\%$ tuning is possible by changing their gap size).

Thanks to the thin-film loading scheme used in our resonator architecture, we showed that the electric field is strongly confined inside the resonator, which allows for reduced interaction with the environment. Hence, loading of this resonator with a lossy medium does not substantially degrade its performance. We also showed that the unloaded-to-loaded Q-factor ratio for a footprint area of 8 mm $\times$ 8 mm is less than 1.7, which was previously reported to be above 2.5 for these dimensions and frequencies in the literature.

The proposed device architecture was microfabricated in different implementations and sizes to verify their theoretical models. A simplified microfabrication methodology was developed to increase the fabrication yield. Here we observed that over 90% yield is achievable using both rigid and flexible substrates. To maintain biocompatibility, all of the constituent of the microfabricated devices were selected carefully (e.g., titanium, gold, polyimide and nitrides). Additionally, the adopted fabrication technique decreased the use of hazardous chemicals such as photoresist, removal chemicals and hydrofluoric acid. This helps to maintain biocompatibility for the microfabricated devices without requiring harsh cleaning. Although all of these steps were carefully designed, biocompatibility of the final structure should be further verified before its final use for human studies.

In this thesis, we also showed that the proposed resonator architecture exhibits metamaterial properties including negative ϵ_r and negative μ_r near its operating frequency. Such metamaterials can be used for various applications including miniaturization of conventional circuits, remote sensing of physical signals, sensitivity improvement of receiver antennas, other medical imaging applications and cloacking. We believe that our deep sub-wavelength resonator as a metamaterial is also a powerful candidate for these applications.

Additionally, MRI characterization of our thin-film loaded helical resonators showed that one order-of-magnitude B1 field enhancement is possible. This explains the signal intensity improvement and SNR improvement in the MR images taken with these resonators. This B1 field improvement comes, however, at a cost of SAR increase. Although the proposed resonator causes almost 50% of SAR increase in its vicinity (for 10 g of averaging), it avoids excessive temperature increase due to smaller volume of localization. Additional temperature studies were conducted to understand their safety of the proposed structure. We found that the maximum temperature increase was about 2.1 °C for a high SAR imaging sequence, where a reference point experiences a temperature increase of 1.6 °C. WE therefore observed that the proposed resonator architecture would be safe for most of the clinical MRI sequences.

Finally, the microfabricated devices were also demonstrated for various MRI applications including subdural electrode marking, SNR improvement and multimodal imaging. Here we demonstrated that the marking of subdural electrodes under MRI is possible without requiring any other imaging method when using such a resonator. Such compatibility increases the reliability of treatment and decreases the risks due to multi-platform dependent discrepancies. In addition to this simplification, we also found that the proposed structure does not put any limitation to conventional imaging modalities such as X-ray. An x-ray image of the resonator was provided to show this capability.

In summary, the findings of this thesis work reflect that the proposed thin-film loaded helical metamaterial architecture is a strong candidate for various applications including marking, SNR improvement, and improving the performance of conventional devices by field localization. We believe that this architecture holds a great promise for future applications such as smart implants and other imaging technologies.

6.1 Contributions to the Literature

The author of this thesis, Saym Gkyar, made the following contributions during the time of this thesis. These contributions to the literature are summarized below one by one, along with the author's individual contribution. This thesis including some of these contributions as reported and identified below:

1. **S.Gokyar**, A. Alipour, E. Unal, E. Atalar, H. V. Demir, "Magnetic resonance imaging assisted by wireless passive implantable fiducial e-markers", IEEE Access, vol. 5, issue 1, pp.19693-19702, 2017, doi: 10.1109/ACCESS.2017.2752649

   In this work, passive wireless resonator architecture, namely resonator e-marker was proposed, designed and demonstrated for subdural electrode marking. Sayim Gokyar contributed to the design, microfabrication, and tuning of the architectures to a predefined MRI frequency. He also conducted the MRI experiments to show the proof of concept demonstration.

2. **S.Gokyar**, A.Alipour, E.Atalar, and H.V.Demir. "Wireless deep-subwavelength metamaterial enabling sub-mm resolution magnetic resonance imaging", in revision, Sensors and actuators A: Physical (2017).

   In this work, the wireless metamaterial resonator architecture was studied and demonstrated with its ultrawide-band tuning properties. Sayim Gokyar contributed to the design, modeling, microfabrication and tuning of the resonator metamaterial. He also conducted the RF characterization of the microfabricated devices followed by MRI experiments.

3. H.V.Demir, E. Unal, and **S.Gokyar**, "Enhancement of magnetic resonance image resolution by using bio-compatible, passive resonator hardware", PCT/TR2014/000083, Republic of Korea-granted, 0157029561

4. A.Alipour, **S.Gokyar**, O.Algin, E.Atalar, and H.V.Demir, "An Inductively coupled ultra-thin, flexible and passive RF resonator for MRI marking and guiding purposes: clinical feasibility", Magn. Reson. in Medicine, (2017), DOI: 10.1002/mrm.26996

   In this work, wireless thin-film resonator architecture was demonstrated for passive catheter tracking purposes under MRI. Sayim Gokyar contributed to the design and modeling of the resonator.

5. A.Alipour, V.Acikel, **S.Gokyar**, O.Algin, C.Oto, E.Atalar, and H.V.Demir. "An inductively receive-only passive resonator probe decoupled using linearly polarized excitation for endocavity MRI imaging", submitted to Magn. Reson. in Medicine, (2017).

   In this work, linearly polarized wireless helical resonator architecture was demonstrated to increase transmit field decoupling for MRI applications. Sayim Gokyar contributed to the design and modeling of the linearly polarized resonator. He finally reviewed the manuscript of this article in conjunction with the other authors.

6. A. Alipour, E. Unal, **S.Gokyar**, and H. V. Demir. "Development of a distance-independent wireless passive RF resonator sensor and a new telemetric measurement technique for wireless strain monitoring", Sensors and Actuators A: Physical 255, (2017): 87-93. doi:10.1016/j.sna.2017.01.010

   In this work, a wireless strain sensing device was proposed, designed and demonstrated with a distance-independent strain measurement methodology. Sayim Gokyar contributed to the design and modeling of the proposed sensor for numerical studies.

7. V. K. Sharma, **S.Gokyar**, Y. Kelestemur, T. Erdem, E. Unal, and H. V. Demir. "Manganese doped fluorescent paramagnetic nanocrystals for dual-modal imaging", Small 10, no. 23, 4961-966, (2014):

doi:10.1002/smll.201401143

In this work, nano-crystals that are suitable for multimodal imaging (T1 and T2) and can be used as a new-generation contrast agents were proposed, synthesized and demonstrated for MRI applications. Sayim Gokyar designed and conducted the MRI experiments to measure the T1 and T2 parameters of these nano-crystals. He also contributed to the MRI characterization.

8. S.Fardindoost, A.Alipour, S. Mohammadi,**S.Gokyar**, R.Sarvari, A.Irajizad, and H.V.Demir, "Flexible strain sensors based on electrostatically actuated graphene flakes", Journal of Micromechanics and Microengineering, 25 (7), 075016, (2015).

   In this work, nested-comb architectures were microfabricated onto a flexible substrate by using graphene flakes to increase the Q-factor of resonators. Hence, better sensitivities were achieved with these flexible sensors. Sayim Gokyar contributed to the microfabrication and RF characterization of the proposed graphene sensors.

9. A.Alipour, **S.Gokyar**, E.Unal, and H.V.Demir, "Thin-film resonator marker for interventional MRI", MRI-Balkan, Ankara, (2014).

   In this work, thin-film resonator architecture was investigated for interventional MRI applications. The first characterization results of the proposed architecture were reported. Sayim Gokyar contributed to the design, microfabrication, and tuning of the device.

10. A.Alipour, S.Fardindoost, S. Mohammadi, **S.Gokyar**, R.Sarvari, A.Irajizad, and H.V.Demir, "Ultrasensitive flexible graphene-based resonator sensor for strain sensing". IEEE RWW, Austin (2016).

    In this work, the resonator architecture was microfabricated with extraordinarily high Q-factors to achieve ultrasensitive sensors. Sayim Gokyar contributed to the microfabrication and RF characterization of the proposed graphene sensors.

Bibliography

[1] P. C. Lauterbur, "Image Formation by Induced Local Interactions: Examples Employing Nuclear Magnetic Resonance", *Nature*, 242, 190-191, 16 March 1973

[2] F. Bloch, W. W. Hansen, and M. Packard, "Nuclear Induction", *Physical Review Letters*, 69, 127, 1946

[3] E. M. Purcell, H. C. Torrey and R. V. Pound, "Resonance Absorption by Nuclear Magnetic Moments in a Solid", *Physical Review Letters*, 69, 37, 1946

[4] "Nobel Prize for Physics", 1952, *Nature* 170, 911-912, 29 November 1952

[5] $https : //www.nobelprize.org/nobel_prizes/medicine/laureates/2003/press.html$, Last Accessed: Oct. 2017

[6] Atalar, E., Bottomley, P. A., Ocali, O., Correia, L. C. L., Kelemen, M. D., Lima, J. A. C. and Zerhouni, E. Atalar, "High resolution intravascular MRI and MRS by using a catheter receiver coil", *Magn. Reson. Med.*, 36: 596-605. doi:10.1002/mrm.1910360415

[7] K. Segkhoonthod, R. R. A. Syms and I. R. Young, "Design of Magneto-Inductive Magnetic Resonance Imaging Catheters", *IEEE Sensors Journal*, Vol. 14, No: 5, May 2014

[8] R. R. A. Syms, I. R. Young, M. M. Ahmad, M. Rea, C. A. Wadsworth, S. D. Taylor-Robinson, "Thin-Film Detector System for Internal Magnetic Resonance Imaging", *Sensors and Actuators A*, 163, 15-24, 2010

[9] R. R. A. Syms, I. R. Young, C. A. Wadsworth, S. D. Taylor-Robinson and M. Rea, "Magnetic Resonance Imaging Duodenoscope", *IEEE Transactions on Biomedical Engineering*, Vol. 60, No:12, Dec. 2013.

[10] K. Segkhoonthod, R. R. A. Syms and I. R. Young, "Design of Magneto-Inductive Magnetic Resonance Imaging Catheters", *IEEE Sensors Journal*, Vol. 14, No: 5, May 2014.

[11] R. R .A. Syms, I. R. Young, M. M. Ahmad, S. D. Taylor-Robinson and M. Rea, "Magneto-Inductive Catheter Receiver for Magnetic Resonance Imaging", *IEEE Trans. On Biomedical Engineering*, Vol. 60, No:9, Sept. 2013

[12] J. E. Baumgartner, "MRI-Compatible Fiducial Markers and Methods for Using the Same", *US PATENT NO: US 20150011868 A1, January 2015.*

[13] E. R. Cosman, T. S. Roberts, "CT and MRI Visible Index Markers for Stereotactic Localization", *US PATENT NO: US 6,419,680 B1, July 2002.*

[14] C. Guihua, C. Wenjie, W. Zhuang, Y. Renxu, L. Hua, G. Jinming, S. Xintao, "MRI-visible polymeric vector bearing CD3 single chain antibody for gene delivery to T cells for immunosuppression", *Biomaterials*, 30 (2009): 1962-1970

[15] P. Pang, C. Wu, M. Shen, F. Gong, K. Zhu, Z. Jiang, S. Guang, H. Shan, X. Shuai, "An MRI-Visible Non-Viral Vector Bearing GD2 Single Chain Antibody for Targeted Gene Delivery to Human Bone Marrow Mesenchymal Stem Cells", *PLoS ONE* 8(10): e76612. doi:10.1371/journal.pone.0076612

[16] C. C. Parker, A. Damyanovich, T. Haycocks, M. Haider, A. Bayley, C. N. Catton, "MRI in the Radiation Treatment Planning of Localized Prostate Cancer Using Intra-Prostatic Fiducial Markers for CT Co-Registration", *Radioterapy and Oncology* 66: 217-224, 2003.

[17] J.W. Gilbert, G.R. Wheeler, G.B. Richardson, S.L. Herder, G.E. Mick, K. Gyarteng-Dakwa, C.M. Kenney, P.G. Broughton, "Guidance of magnetic resonance imaging and placement of skin-marker localization devices", *J. Neurosurg. Sci.*,55(2):85-8, 2011.

[18] M. Burl, G. A. Coutts and I. R. Young, "Tuned Fiducial Markers to Identify Body Locations with Minimal Perturbation of Tissue Magnetization", *Magn. Res. On Med.*, 36:491-493, 1996.

[19] H. H. Quick, M. O. Zenge, S. Massing, M. E. Ladd, "Wireless Active Catheter Visualization: Passive Decoupling Methods and Their Impact on Catheter Visibility",*Proc. Intl. Soc. Magnetic Resonance in Medicine*, 13 (2005)

[20] Paul A. Bottomley, “Turning Up the Heat on MRI”, *J. Am. Coll. Radiol.*, 5 (7), 853-855, July 2008.

[21] G. Thormer, N. Garnov, M. Moche, J. Haase, T. KAhn and H. Busse, “Simultaneous 3D localization of multiple MR-visible markers in fully reconstructed MR images: proof-of-concept for subsecond position tracking”, *Magnetic Resonance Imaging*, 30, 2012, 371-381,

[22] M. Rea, D. McRobbie, H. Elhawary, Z. T. H. Tse, M. Lamperth, I. R. Young, “Sub-pixel Localisation of passive micro-coil fiducial markers in interventional MRI”, *Magn Reson Mater Phy*, 22: 71, 2009, doi:10.1007/s10334-008-0143-1.

[23] S. S. Dalal, E. Edwards, H. E. Kirsch, N. M. Barbao, R. T. Knight, S. S. Nagarajan, “Localization of neurosurgically implanted electrodes via photograph-MRI radiograph coregistration”, *Journal of Neuroscience Methods*, 174 (2008): 106-115

[24] P. S. LaViolette, S. D. Rand, M. Raghavan, B. M. Ellingson, K. M. Schmainda and W. Mueller, “Three-Dimensional Visualization of Subdural Electrodes for Presurgical Planning”, *Neurosurgery*, 68, 152-161, March 2011.

[25] M. A. Silberbusch, M. I. Rothman, G. K. Bergey, G. H. Zoarski and M. T. Zagardo, “Subdural Grid Implantation for Intracranial EEG Recording: CT and MR Appearance”, *AJNR* 19:1089-1093, June 1998

[26] J. X. Tao, S. Hawes-Ebersole, M. Baldwin, S. Shah, R. K. Erickson, J. S. Ebersole, “The accuracy and reliability of 3D CT/MRI co-registration in planning epilepsy surgery”, *Clinical Neurophysiology*, 120 (2009): 748-753

[27] B. J. Erickson, C. R. Jack, “Correlation of Single Photon Emission CT with MRI Data Using Fiduciary Markers”, *AJNR*, 14: 713-720, 1993.

[28] M. Nelles, R. Koenig, J. Kandyba, C. Schaller, H. Urbach, “Fusion of MRI and CT with subdural grid electrodes”, *Zentralbl Neurochirurgie*, 65(4), 174-9, November 2004.

[29] Dwight G. Nishimura, “The Principles of Magnetic Resonance Imaging”, *Copyright April 1996 by Dwight G. Nishimura, Stanford University*, USA, pp 114, April, 1996

[30] *National Magnetic Resonance Research center*, http://umram.bilkent.edu.tr/

[31] L. Wen-Tao, Z. Dong-Lin, and T. Xin, “A novel approach to designing cylindrical-surface shim coils for a superconducting magnet of magnetic resonance imaging”, *Chin. Phys.*, B Vol. 19, No. 1, 018701, 2010.

[32] J. M. Jin, “Electromagnetic Analysis and Design in Magnetic Resonance Imaging”, *CRC Press*, September 29, 1998, ISBN 9780849396939

[33] A.Daliri, A.Galehdar, S.John, C.H.Wang, W.S.T.Rowe, K.Ghorbani, “Wireless strain measurement using circular microstrip patch antennas”, *Sensors and Actuators: A Physical*, 184 (2012), 86-92

[34] R. Melik, E. Unal, N. K. Perkgoz, C. Puttlitz, H. V. Demir, “Metamaterial-based wireless strain sensors”, *Applied Physics Letters*, 95, 011106 (2009)

[35] R. Melik, E.Unal, N. Kosku Perkgoz, B. Santoni, D. Kamstock, C. Puttlitz, and H. V. Demir, “Nested Metamaterials for Wireless Strain Sensing”, *IEEE Journal of Special Topics in Quantum Electronics (special issue on Metamaterials)*, 16, 450 (2010)

[36] R. Melik, E.Unal, N. Kosku Perkgoz, C. Puttlitz, and H. V. Demir, “Metamaterial based telemetric strain sensing in different materials”, *Optics Express*, 18, 5000 (2010)

[37] R. Melik, E.Unal, N. Kosku Perkgoz, C. Puttlitz, and H. V. Demir, “Flexible Metamaterials for Wireless Strain Sensing”, *Applied Physics Letters*, 95, 181105 (2009)

[38] Q.Y.Tang, Y.M.Pan, Y.C.Chan, K.W.Leung, “Frequency-tunable soft composite antennas for wireless strain sensing”, *Sensors and Actuators: A Physical*, 179 (2012), 137-145

[39] F.Bilotti, A.Toscano, L.Vegni “Design of Spiral and Multiple Split-Ring Resonators for the Realization of Miniaturized Metamaterial Samples”, *IEEE Transactions on Antennas and Propagation*, Vol: 55, Issue: 8, Aug. 2007, DOI: 10.1109/TAP.2007.901950

[40] J. C. Ginefri, A. Rubin, M. Tatoulian, M. Woytasik, F. Boumezbeur, B. Djemai, M. Poirier-Quinot, F. Lethimonnier, L. Darrasse, E. Dufour-Gergam.,

"Implanted, inductively-coupled, rf coils fabricated on flexible polymeric material: Application to in vivo rat brain MRI at 7T", *Journal of Magnetic Resonance*, 224, (2012), 61-70

[41] M. J. Freire, R. Marques, "Near-field imaging in the megahertz range by strongly coupled magnetoinductive surfaces: Experiment and ab initio analysis", *Journal of Applied Physics*, 100, 063105 (2006)

[42] E. Ekmekci, K. Topalli, T. Akin and G. Turhan-Sayan, "A tunable multi-band metamaterial design using micro-split SRR structures", *Optics Express*, Vol. 17, No. 18 (2009)

[43] M. M. Ahmad et al, "Catheter-based flexible microcoil RF detectors for internal magnetic resonance imaging", *Journal of Micromechanics and Microengineering*, 19 (2009), 074011

[44] F. Taffoni, D. Formica, P. Saccomandi, G. D. Pino and E. Schena, "Optical Fiber-Based MR-Compatible Sensors for Medical Applications: An Overview", *Sensors*, 13, 14105-14120, (2013), doi:10.3390/s13101410105

[45] S. Gokyar, "Novel Implantable Distributively Loaded Flexible Resonators for MRI", *M.Sc. Thesis, Bilkent University*, Ankara, August 2011

[46] S. Gokyar, A. Alipour, E. Unal, E. Atalar, H. V. Demir, "Magnetic Resonance Imaging Assisted by Wireless Passive Implantable Fiducial e-Markers", *IEEE Access*, Vol. 5, Issue 1, pp.19693-19702, December 2017, doi: 10.1109/ACCESS.2017.2752649

[47] A.Alipour, S.Gokyar, O.Algin, E.Atalar, and H.V.Demir, "An Inductively coupled ultra-thin, flexible and passive RF resonator for MRI marking and guiding purposes: clinical feasibility", *Magn. Reson. in Medicine*, 17 November 2017, DOI: 10.1002/mrm.26996

[48] A. Alipour, "Wireless Thin Film Microwave Resonators for Sensing and Marking", *PhD. Dissertation, Bilkent University*, Ankara, May 2017

[49] J.D.Baena, J.Bonache, F.Martin, R. Marques Sillero, F. Falcone, T. Lopetegi, M. A. G. Laso, J. Garcia-Garcia, I. Gil, M. F. Portillo, M. Sorolla, "Equivalent-circuit models for split-ring resonators and complementary split-ring resonators coupled to planar transmission lines", *IEEE Transactions On Microwave Theory and Technology*, Vol. MTT-53 (2005), 1451-1461

[50] B. Ozbey, A. Altintas, H. V. Demir, V. B. Erturk, "An Equivalent Circuit Model for Nested Split-Ring Resonators", *IEEE Transactions on Microwave Theory and Techniques*, 65, 3733 (2017).

[51] Khennouche M. S., Gadot F., Lustrac A., Quinot M. P., Darrasse L., Ginefri J. C., "The use of metamaterials: a solution to improve the performance of Radiofrequency Coil for Magnetic Resonance Imaging (MRI)?", *Metamorphose-VI*, 468-470, 2011

[52] Inder Bahl, "Lumped Elements for RF and Microwave Circuits", *Artech House*, ISBN-13: 978-1580533096, 2003

[53] S.S.Mohan, M.Hershenson, "Simple accurate expression for planar spiral inductances", *IEEE Journal of Solid State Circuits*, Vol. 34-10 (Oct. 1999), 1419-1424

[54] R. Marques, L. Jelinek, F. Mesa, "Negative Refraction From Balanced Quasi-Planar Chiral Inclusions", *Microwave and Optical Technology Letters*, Vol. 49, No. 10 (2007)

[55] F. W. Grover, "Inductance Calculations: Working Formulas and Tables", *Dover Phoenix Ed.*, 2004

[56] J. T. Vaughan, J. R. Griffiths, "RF Coils for MRI", *Wiley*, 2010, UK, pp 17-25

[57] A.L.Coutrot, E. Dufour-Gergam, E. Martincic, J.P. Gilles, J.P. Grandchamp, J.M. Quemper, A. Bosseboeuf, F. Alves, B. Ahamada, "Electromagnetic micro-device realized by electrochemical way", *Sensors and Actuators A*, 91 (2001), 80-84

[58] J. C. Ginefri, E. Durand, L. Darrasse, "Quick Measurement of Nuclear Magnetic Resonance Coil Sensitivity with a Single-Loop Probe", *Review of Scientific Instruments*, 70, 4730, 1999

[59] B. Keil, J. N. Blau, S. Biber, P. Hoecht, V. Tountcheva, K. Setsompop, C. Triantafyllou and L. L. Wald, "A 64 Channel 3T Array Coil for Accelerated Brain MRI", *Magnetic Resonance in Medicine*, 70: 248-258, 2013

[60] E.M.Kardoulaki, R.R.A.Syms, I.R.Young, M.Rea, W.M.W.Gedroyc, "Thin-film micro-coil detectors: Application in MR-thermometry", *Sensors and Actuators: A Physical*, 226 (2015), 48-58

[61] X. Zhang, E. Usi, S. K. Khan, M. Sadatgol and D. O. Guney, "Extremely Sub-wavelength Negative Index Metamaterial", *Progress in Electromagnetics Research*, Vol. 152, 95-104, 2015.

[62] C. P. Scarborough, Z. H. Jiang, D. H. Werner, C. Rivero-Baleine and C. Drake, "Experimental demonstration of an isotropic metamaterial superlens with a negative unity permeability at 8.5 MHz", *Applied Physics Letters*, 101, 014101 (2012)

[63] M. J. Freire, R. Marques, L. Jelinek, "Experimental Demonstration of a u=-1 metamaterial lens for magnetic resonance imaging", *Applied Physics Letters*, 93, 231108 (2008)

[64] D. R. Smith, S. Schultz, P. Markos, C. M. Soukoulis, "Determination of effective permittivity and permeability of metamaterials from reflection and transmission coefficients," *Phys. Rev. B*, Vol. 65, 195104, 2002.

[65] http://niremf.ifac.cnr.it/tissprop/ Last accessed on April, 2017

[66] V. Acikel, O. Ulutan, A. C. Ozen, B. Akin, Y. Eryaman and E. Atalar, "A Novel MRI Based Electrical Properties Measurement Technique", *Proc. Intl. Soc. Mag. Reson. Med.*, 21 (2013)

[67] J.B. Warntjes, O. D. Leinhard, J. West, P. Lundberg, "Rapid magnetic resonance quantification on the brain: Optimization for clinical usage", *Magn Reson Med.*, 2008, 60: 320-329.

[68] U. Katscher, P. Bornert, C. Leussler, J. S. van den Brink, "Transmit SENSE", *Magn Reson Med.*, 2003, 49: 144-150

[69] Y. Zhu, "Parallel excitation with an array of transmit coils", *Magn Reson Med.*, 2004, 51: 775-784

[70] D. Xu, K. F. King, Y. Zhu, G. C. McKinnon, Z. P. Liang, "Designing multichannel, multidimensional, arbitrary flip angle RF pulses using an optimal control approach", *Magn Reson Med.*, 2008, 59: 547-560

[71] G. R. Morrell, "A phase-sensitive method of flip angle mapping", *Magn Reson Med.*, 2008, 60: 889-894

[72] C.H. Cuningham, J.M. Pauly and K.S. Nayak, "Saturated Double-Angle Method for Rapid B1+ Mapping", *Magn. Reson. Med.*, 55, 2006, 1326-1333

[73] J.P. Hornak, J. Szumowski, R. G. Bryant, "Magnetic field mapping", *Magn Reson Med.*, 1988, 6: 158-163

[74] F. Bloch, A. Siegert, "Magnetic resonance for nonrotating fields", *Phys Rev.*, 1940, 57: 522-527

[75] S. Wang, J. Murphy-Boesch, H. Merkle, A. P. Koretsky, and J. H. Duyn "B1 Homogenization in MRI by Multi-layer Coupled Coils", *IEEE Trans Med Imaging.* 28(4): 551-554, 2009

[76] N. F. Ramsey, "Resonance transitions induced by perturbations at two or more different frequencies", *Phys Rev.* 1955, 100(4): 1191-1194

[77] M. Steffen, L. M. K. Vandersypen, I. L. Chuang, "Simultaneous soft pulses applied at nearby frequencies", *Journal of Magn Reson.*, 2000, 146(2): 369-374

[78] L. I. Sacolick, F. Wiesinger, I. Hancu, and M. W. Vogel, "B1 mapping by Bloch-Siegert shift", *Magn. Reson. Med.*, 63: 1315-1322 doi:10.1002/mrm.22357

[79] R. M. Henkelman, "Measurement of signal intensities in the presence of noise in MR images", *Med. Phys.*, 12(2), March/April 1985

[80] E. Conil, A. Hadjem, F. Lacroux, M. F. Wong and J. Wiart,"Variability Analysis of SAR from 20 MHz to 2.4 GHz for Different Adult and Child Models Using Finite-Difference Time-Domain", *Physics in Medicine and Biology*, Vol. 53, 2008

[81] J. Wang, O. Fujiwara,"Comparison and Electromagnetic Absorption Characteristics in Realistic Human Head Models of Adult and Children for 900 MHz Mobile Phones", *IEEE Transactions on Microwave Theory and Techniques*, Vol. 51, No:3, March 2003

[82] M. Kozlov and R. Turner,"A comparison of Ansoft HFSS and CST Microwave Studio Simulation Software for Multi-Channel Coil Design and SAR Estimation at 7T MRI", *PIERS Online*, Vol. 6, No:4, 2010

[83] E. Asano, C. Juhasz, A. Shah, S. Sood and H. T. Chugani,"Role of Subdural Electrocorticography in Prediction of Long Term Seizure Outcome in Epilepsy Surgery", *Brain, A Journal of Neurology*, 2009, 132, 1038-1047

[84] D. W. Carmichael, J. S. Thornton, R. Rodionov, R. Thornton, A. McEvoy, P. J. Allen and L. Lemieux,"Safety of Localizing Epilepsy Monitoring Intracranial Electroencephalograph Electrodes Using MRI: Radiofrequency-Induced Heating", *Journal Of Magnetic Resonance Imaging*, 28:1233"1244 (2008)

[85] Veselago V.G.,"The electrodynamics of substances with simultaneously negative values of ϵ *and* μ,", *Sov. Usp.*, Vol. 10, 509"514 (1968)

[86] Withayachumnankul, K.Jaruwongrungsee, A.Tuantranont, C.Fumeaux, D.Abbott,"Metamaterial-based microfluidic sensor for dielectric characterization", *Sensors and Actuators: A Physical*, 189 (2013), 233-237

[87] A.Alipour, E.Unal, S.Gokyar, H.V.Demir,"Development of a distance-independent wireless passive RF resonator sensor and a new telemetric measurement technique for wireless strain monitoring", *Sensors and Actuators: A Physical*, 255 (2017), 87-93

[88] A.K.Horestani, J.Naqui, Z.Shaterian, D.Abbott, C.Fumeaux, F.Martin,"Two-dimensional alignment and displacement sensor based on movable broadside-coupled split ring resonators", *Sensors and Actuators: A Physical*, 210 (2014), 18-24

[89] M. Lapine, D. Powell, M. Gorkunov, I. Shadrivov, R. Marqu"s, Y. Kivshar,"Structural tunability in metamaterials", *Applied Physics Letters*, 95, 084105 (2009), DOI: 10.1063/1.3211920

[90] F.Bilotti, L.Nucci, L.Vegni,"An SRR based microwave absorber", *Microwave and Optical Technology Letters*, 2006, 48.11: 2171-2175

[91] R. Melik, E.Unal, N. Kosku Perkgoz, C. Puttlitz, and H. V. Demir,"Circular High-Q Resonating Isotropic Strain Sensors with Large Shift of Resonance Frequency under Stress", *Sensors*, 9, 9444, (2009)

[92] R. Melik, N. Kosku Perkgoz, E. Unal, C. Puttlitz, and H. V. Demir,"Bio-implantable passive on-chip RF-MEMS strain sensing resonators for orthopaedic applications", *Journal of Micromechanics and Microengineering*, 18, 115017 (2008)

[93] J. B. Pendry,"Negative Refraction Makes a Perfect Lens", *Physical Review Letters*, 85, 3966 (2000)

[94] D. R. Smith, J. B. Pendry, M. C. K. Wiltshire,"Metamaterials and Negative Refractive Index", *Science*, 305, 788 (2004)

[95] N. Fang, H. Lee, C. Sun, X. Zhang,"Sub"Diffraction-Limited Optical Imaging with a Silver Superlens", *Science*, 308, 534 (2005)

[96] F. Lemoult, N. Kaina, M. Fink, G. Lerosey,"Wave propagation control at the deep subwavelength scale in metamaterials", *Nature Physics*, Vol. 9, 2013.

[97] M. C. K. Wiltshire, J. B. Pendry, I. R. Young, D. J. Larkman, D.J. Gilderdale and J. V. Hajnal"Microstructured Magnetic Materials for RF Flux Guides in Magnetic Resonance Imaging", *Science*, 291, 849, 51 (2001)

[98] E. Moser, M. Meyerspeer, F. Ph. S. Fischmeister, G. Grabner, H. Bauer and S. Trattnig,"Windows on the Human Body-in vivo High-Field Magnetic Resonance Research and Applications in Medicine and Psychology", *Sensors*, 10, 5724-5757 (2010)

[99] M. Blaimer, F. Breuer, M. Mueller, R. M. Heidemann, M. A. Griswold and P. M. Jakob,"SMASH, SENSE, PILS, GRAPPA, How to Choose the Optimal Method", *Magnetic Resonance Imaging*, Vol. 15, Nu. 4, 223-236, (August 2004)

[100] M. A. Griswold, P. M. Jakob, R. M. Heidemann, M. Nittka, V. Jellus, J. Wang, B. Kiefer and A. Haase,"Generalized Autocalibrating Partially Parallel Acquisitions (GRAPPA)", *Magnetic Resonance in Medicine*, vol. 47, 1202-1210, (2010)

[101] C. Baltes, N. Radzwill, S. Bosshard, D. Marek, M. Rudin,"Micro MRI of the mouse brain using a novel 400 MHz cryogenic quadrature RF probe", *NMR in Biomedicine*, 22: 834-842, 2009, doi:10.1002/nbm.1396

[102] T. Dohi, K. Matsumoto, I. Shimoyama,"Flexible Micro Resonator for the Magnetic Resonance Catheter", *The 13th Int. Conf. on Solid-State Sensors, Actuators and Microsystems*, Seoul, Korea, June 5-9, 2005

[103] J. Gawlitza, M. Reiss-Zimmermann, G. Th"rmer, A. Schaudinn, N. Linder, N. Garnov, L.C. Horn, D. H. Minh, R. Ganzer, J.U. Stolzenburg, T. Kahn, M. Moche, H. Bussea, "Impact of the use of an endorectal coil for 3 T prostate MRI on image quality and cancer detection rate", *Nature, Scientific Reports*, 7:40640 (2017), doi:""10.1038/srep40640

[104] P. Gonord, S. Kan, A. Leroy-Willig, and C. Wary,"Multigap parallel-plate bracelet resonator frequency determination and applications", *Review of Scientific Instruments*, 65, 3363 (1994), doi: 10.1063/1.1144573

[105] P. Gonord S. Kan, A. Leroy-Willig,"Parallel Plate Split-Conductor Surface Coil: Analysis and Design", *Magn. Reson. in Medicine*, 6, 353-358 (1988)

[106] I. Lin, H. C. Yang, J.H. Chen,"Diffusion tensor imaging using a high-temperature superconducting resonator in a 3T magnetic resonance imaging for a spontaneous rat brain tumor", *Applied Physics Letters*, 102, 063701 (2013)

[107] T.Matsunaga, Y.Matsuoka, S.Ichimura, Q.Wei, K.Kuroda, Z.Kato, M.Esashi, Y.Haga,"Multilayered Receive Coil Produced Using a Non-planar Photofabrication Process for an Intraluminal Magnetic Resonance Imaging", *Sensors and Actuators: A Physical*, http://dx.doi.org/10.1016/j.sna.2017.04.021

[108] D. Sakellariou, G. Le Goff, J. F. Jacquinot,"High-resolution, high-sensitivity NMR of nanolitre anisotropic samples by coil spinning", *Nature*, 447, 694-697 (7 June 2007)

[109] E. Laistler, M. Poirier-Quinot, S. A. Lambert, R.M. Dubuisson, O. M. Girard, E. Moser, L. Darrasse and J.C. Ginefri,"In Vivo MR Imaging of the Human Skin at Subnanoliter Resolution Using a Superconductor Surface Coil at 1.5 Tesla", *Journal of Magnetic Resonance Imaging*, Vol. 41, Issue 2, 496"504 (February 2015), doi:10.1002/jmri.24549

[110] R. Kriegl, J.C. Ginefri, M. Poirier-Quinot, L. Darrasse, S. Goluch, A. Kuehne, E. Moser, E. Laisler,"Novel Inductive Decoupling Technique for Flexible Transceiver Arrays of Monolithic Transmission Line Resonators", *Magnetic Resonance in Medicine*, 73: 1669-1681 (2015)

[111] J. A. Lehmann-Horn, J.F. Jacquinot, J. C. Ginefri, C. Bonhomme, D. Sakellariou.,"Monolithic MACS micro resonators", *Journal of Magnetic Resonance*, 271, (2016), 46-51

[112] S.Gokyar, A.Alipour, E.Atalar, and H.V.Demir."Wireless deep-subwavelength metamaterial enabling sub-mm resolution magnetic resonance imaging", *In submission to Sensors and actuators A: Physical*